Universidade de Aveiro Departamento de Geociências
2016

RAQUEL DA SILVA RIBEIRO

ONDAS MIGRANTES DE SEDIMENTOS NO MAR JÓNICO REVELADAS EM PERFIS DE REFLEXÃO SÍSMICA MULTICANAL DE ALTA RESOLUÇÃO

MIGRATING SEDIMENT WAVES IN THE IONIAN SEA REVEALED FROM HIGH RESOLUTION MULTICHANNEL SEISMIC REFLECTION PROFILES

Universidade de Aveiro Departamento de Geociências
2016

RAQUEL DA SILVA RIBEIRO

ONDAS MIGRANTES DE SEDIMENTOS NO MAR JÓNICO REVELADAS EM PERFIS DE REFLEXÃO SÍSMICA MULTICANAL DE ALTA RESOLUÇÃO

MIGRATING SEDIMENT WAVES IN THE IONIAN SEA REVEALED FROM HIGH RESOLUTION MULTICHANNEL SEISMIC REFLECTION PROFILES

Dissertação apresentada à Universidade de Aveiro para cumprimento dos requisitos necessários à obtenção do grau de Mestre em Engenharia Geológica, realizada sob a orientação científica do Doutor Luís Filipe Fuentefria de Menezes Pinheiro, Professor Associado do Departamento de Geociências da Universidade de Aveiro

o júri

presidente	Prof. Doutor Jorge Manuel Pessoa Girão Medina Professor Auxiliar do Departamento de Geociências da Universidade de Aveiro
arguente	Doutor Pedro António Gancedo Terrinha Investigador Auxiliar do Instituto Português do Mar e da Atmosfera Professor Auxiliar Convidado da Faculdade de Ciências da Universidade de Lisboa
orientador	Prof. Luís Filipe Fuentefria Menezes Pinheiro Professor Associado do Departamento de Geociências da Universidade de Aveiro

agradecimentos

Em primeiro lugar agradeço ao Professor Luís Menezes pela oportunidade de trabalhar e aprender sob a sua orientação. Obrigado pelo tempo despendido a ensinar e pela sua paciência. Obrigado pela oportunidade de embarcar na Caravela Vera Cruz durante uma semana, no âmbito da Ciência Viva no Verão! Foi uma experiência muito enriquecedora, quer a nível pessoal quer a nível académico! Espero um dia voltar a embarcar.

Um agradecimento ao Dr. Marc-André Gutscher pela cedência dos dados originais dos perfis sísmicos da campanha CIRCEE-HR e do mapa batimétrico de alta resolução, que permitiram a realização deste estudo.

Um muito obrigado aos meus pais! Não só pela oportunidade de frequentar um curso superior, mas também pela compreensão no dia-a-dia, principalmente na fase final do mestrado. Rafa, não me esqueci de ti, obrigada por me chateares todos os dias.

Aos meus colegas do LGGM, Mirian, Laurício e Angel, pois tantas foram as horas que passámos juntos, entre trabalho, desabafos e peripécias. Um forte agradecimento ao Omar Benazzouz, pela ajuda prestada e pela paciência em responder e explicar detalhadamente a todas as minhas questões.

Obrigada à Sandra e Sofia, Ângela, Joana, Sara, Vanessa, e ao André e Baieta, por serem bons amigos e por terem acompanhado todo o meu percurso académico.

Ao Ricardo, por nestes últimos meses ter sido um excelente amigo e companheiro.

palavras-chave

Ondas Migrantes de Sedimentos, Mar Jónico, Prisma Acrecionário da Calábria, Reflexão Sísmica Multicanal 2D de Alta Resolução, Batimetria Multifeixe, Processamento e Interpretação Sísmica.

resumo

A análise e reprocessamento de perfis 2D de reflexão sísmica de alta resolução, adquiridos no âmbito do cruzeiro CIRCEE-HR, permitiu a identificação da presença de ondas de sedimentos actuais e fósseis no Mar Jónico. A ocorrência de ondas migrantes de sedimentos atuais nesta área foi relatada anteriormente, com base na batimetria multifeixe, mas aqui relatamos pela primeira vez, a nosso conhecimento, a ocorrência de ondas migrantes fósseis nessa região, reveladas pelos perfis de reflexão sísmica. Ondas migrantes de sedimentos foram observadas nos perfis sísmicos CIRCEE-HR complementados por batimetria multifeixe. 3 campos principais de ondas de sedimentos, tanto fósseis como ativos foram identificados com várias gerações de ondas de sedimentos com diferentes comprimentos de onda e amplitudes. Na ausência de idades bem constrangidas para calibrar os perfis sísmicos na área de estudo, e de forma a atribuir idades tentativas aos vários episódios de formação de ondas de sedimentos, foi realizada uma interpretação geral dos principais refletores sísmicos e de eventos bem datados, que foram correlacionados entre os vários perfis sísmicos. Dois modelos principais de formação foram propostos para a formação das ondas de sedimentos nesta área. Para o Campo de Ondas de Sedimentos C, mais setentrional, embora não se possa descartar uma possível origem relacionada ao spillover de canal turbidítico, parece que as ondas internas solitárias geradas no Estreito de Messina podem ser o mecanismo responsável mais provável. No entanto, no que diz respeito aos dois campos a sul, A e B, embora não seja possível excluir o possível papel das ondas internas ou a interacção dos canais turbiditos com as correntes de fundo, não existem observações da presença de nenhum deles nesta área. Portanto, propomos que as ondas de sedimentos fósseis foram formadas por spillover dos canais turbidíticos, produzindo ondas de sedimento aproximadamente perpendiculares ou oblíquas ao canal principal. O canal turbidítico principal, que agora segue aproximadamente a frente de deformação, parece ter sido antes localizado mais ao norte. Isto pode ser uma indicação de que a migração para o sul do prisma acrecionário associado ao roll-back da subdução parou a formação das ondas de sedimento, que são atualmente formadas muito mais ao sul. No campo B, a formação das ondas de sedimento parece ter parado completamente em algum momento há cerca de 400kyr, embora este processo tenha começado localmente há cerca de 700kyr. Interpretamos isso como ligado à migração para sul do canal turbiditico principal que segue aproximadamente a frente de deformação, causada pelo roll-back da subducção.

acknowledgments

First of all, I thank Professor Luís Menezes for the opportunity to work and learn under his guidance. Thanks for the time spent teaching and for your patience. Thank you for the opportunity to embark on the Caravela Vera Cruz for a week, in scope of Ciência Viva no Verão! It was a very enriching experience, both personally and academically! I hope someday to get back on board.

Thanks to Dr. Marc-André Gutscher for providing the original data of the CIRCEE-HR seismic profiles and the high-resolution bathymetric map, which allowed this study to be carried out.

A big thank you to my parents! Not only for the opportunity to attend a higher education course but for the daily understanding, especially in the final phase of the Master's program. Rafa, I have not forgotten you, thank you for annoying me every day.

To my LGGM colleagues, Mirian, Laurício and Angel, because so many were the hours that we spent together, between work and jokes. A big thank you to Omar Benazzouz for his help and patience in answering and detail explaining all my questions.

Thank you to Sandra and Sofia, Ângela, Joana, Sara, Vanessa, and André and Baieta, for their great friendship and for having accompanied my entire academic journey.

To Ricardo, for have been an excellent friend and partner in these last months.

keywords

Migrating Sediment Waves, Ionian Sea, Calabrian Accreationary Wedge, 2D High-Resolution Multichannel Seismic Reflection, Multibeam Bathymetry, Seismic Processing and Interpretation.

abstract

Analysis and reprocessing of 2D high-resolution seismic reflection profiles acquired in the scope of the CIRCEE-HR cruise has allowed the identification of the presence of both present-day active and fossil migrating sediment waves in the Ionian Sea. The occurrence of presently active migrating sediment waves in this area was previously reported, based on multibeam bathymetry, but here we report for the first time to our knowledge, the occurrence of fossil migrating waves in this region, imaged by seismic reflection profiles. Migrating sediment waves were identified on the CIRCEE-HR seismic profiles complemented by multibeam bathymetry. 3 main fields of sediment waves, both fossil and active were identified with several generations of sediment waves with different wavelengths and amplitudes. In the absence of borehole constrained age interpretations of seismic profiles in the study area, and in order to assign tentative dates to the various episodes of sediment wave formation, an overall interpretation of the main seismic reflectors and of well dated events was carried out and correlated between the various seismic profiles. Two main models of formation were proposed for the formation of the sediment waves in this area. For the northernmost Sediment Wave Field C, although a possible origin related to turbidite channel spillover cannot be ruled out, it appears that solitary internal waves generated at the Messina Strait may be the more likely responsible mechanism. As concerns the two southern fields A and B, however, although the possible role of internal waves or the interaction of turbidite channels with bottom currents cannot be ruled out, there are no reported observations of their presence of neither of them in this area. Therefore, we propose that the fossil sediment waves have been formed by turbidite channel spillover, producing sediment waves approximately perpendicular or oblique to the main turbidite channel. The turbidite channel that now approximately follows the deformation front appears to have been before located further north, this may be an indication that the migration to the south of the accretionary wedge associated with the subduction rollback has stopped the formation of the sediment waves, which are at present formed much further south. In field B, the formation of the sediment waves appears to have completely stopped sometime at about 400kyr, although this process started locally at about 700mMyr. We interpret this as linked to the migration to the south of the turbidite channel that approximately follows the edge of the deformation front, caused by the subduction rollback.

Contents

List of Figures

Chapter I. Introduction

I.1 Nature and Scope of this work

This thesis corresponds to the final project of the MSc Course in Geological Engineering, branch of Geological Resources, from the Geosciences Department of the University of Aveiro. This research work was carried out under the supervision of Prof. Luís Menezes Pinheiro, from the University of Aveiro. All the processing and interpretation of the seismic data presented in this work was carried out at the Marine Geology and Geophysics Laboratory of the Geosciences Department of the University of Aveiro.

I.2 Objectives

The main objective of this thesis was to investigate, characterize and try to understand the formation of the migrating sediment waves that were identified on a set of high resolution multichannel seismic reflection profiles acquired in the Ionian Sea in the scope of the CIRCEE Cruise, and to propose possible models for their formation and abandonment. Specific objectives were: (1) to reprocess selected multichannel seismic profiles to obtain good quality images of the subsurface geology, and in particular to improve the imaging in the deeper part of the seismic sections; this involved learning multichannel seismic data processing, getting familiar with the *SPW* seismic processing software and implementing the more adequate processing flows; (2) to perform an overall interpretation of selected seismic reflection profiles in the study area and to assign tentative ages to the main reflectors; (3) to characterize the various generations of sediment waves (both active and fossil) in the study area and compare them with similar occurrences elsewhere; (3) to propose a model for their formation and for their abandonment.

I.3 The CIRCEE-HR Survey

The CIRCEE-HR survey (***C****alabrian arc* ***I****onian sea* ***R****esearch and* ***C****atastrophic historical* ***E****arthquak****E****s in southern Italy: a* ***H****igh-****R****esolution seismic survey*) was

carried out in the Ionian Sea, offshore Southern Italy, onboard of the R/V *Le Suroit* between the 2nd and the 24th of October 2013.

The main purpose of this survey was to conduct a study of the neo-tectonics in the accretionary wedge of the Calabrian subduction zone, a region struck repeatedly by some of the most destructive earthquakes in European history. The main objectives of this scientific cruise were to seek evidence of active faults associated with these structures, and to characterize the degree of activity of the Calabria accretionary wedge (sedimentary deformation, dewatering processes and the thermal regime), in order to better assess its seismogenic potential. Another major objective was to try to determine the typical recurrence interval for large earthquakes in the region (by coring and dating of turbidites).

The applied methods were high-resolution seismic and sub-bottom profiling (chirp), bathymetric swath mapping, gravity coring of the turbidite deposits with simultaneous heat-flow measurements.

I.4 Dataset

The dataset used for this work, kindly made available by the CIRCEE Cruise Chief Scientist, Dr. Marc-Andre Gutscher, from the Université de Bretagne Occidentale, France, consisted at 18 multichannel seismic reflection profiles (with a total extension of 1505 km) and a multibeam bathymetry cover acquired in the Ionian Sea, East offshore of Sicily, during the CIRCEE-HR cruise (Figure I.1).

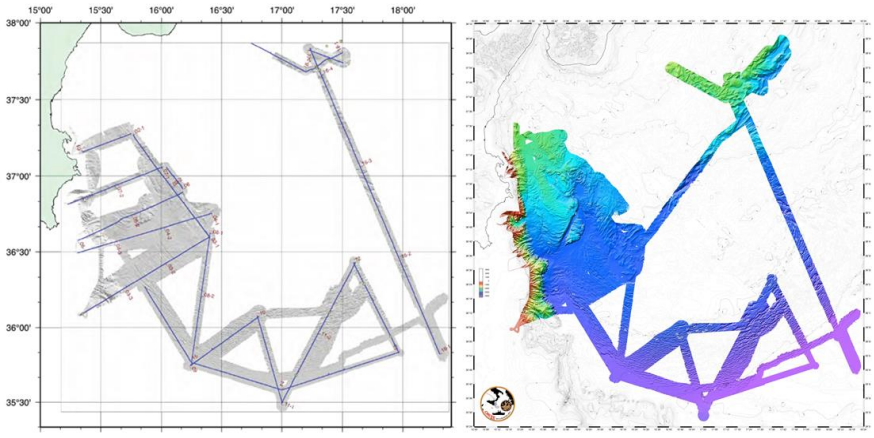

Figure I.1 - Location of the multichannel seismic reflection lines and the multibeam high resolution bathymetry acquired during the CIRCEE-HR cruise, and used for this work.

I.5 Methodology

In order to accomplish the main objectives, two different methodologies were adopted: one for the seismic data processing and the other for the seismic data interpretation.

Seismic Data Processing

The processing of the seismic profiles was performed with the *Seismic Processing Workshop* 3 (SPW3), from Parallel Geoscience Corporation. After getting familiar with the main steps of multichannel seismic data processing and with the architecture of this software, a processing flow was designed to improve the preliminary onboard seismic processing of selected profiles. The raw SEG-Y seismic data were fully processed to achieve high quality seismic images in depth, particularly in the areas where the migrating sediment waves have been identified. The main processing steps consisted of: pre-processing Quality Control, Geometry Assignment, Frequency Filtering, Velocity Analysis, CMP sorting and Post-Stack time migration.

Seismic Interpretation

The seismic interpretation of the seismic profiles was carried out using the *Kingdom Suite 2015*, seismic and geological interpretation software from IHS Markit Corporate, to whom we thank the licenses donation to the University of Aveiro. The seismic profiles that cross the Ionian abyssal plain and the deformation front of the accretionary wedge were the first to be interpreted; in this area, the correlation of the main seismic horizons between the different lines was possible whereas the spacing between the other 2D seismic lines made such a correlation more difficult and less reliable. As the interpretation advanced to the western profiles, the focus was on the identification, mapping and characterization of the sediment waves that were observed in eight profiles, which became the main objective of this study. A more detailed interpretation was carried out in these areas in order to understand the different stages of formation of the sediment waves.

I.6 Structure of this thesis

This thesis is divided into seven chapters. The first chapter briefly introduces the reader to the nature and scope of this work, the main objectives, the scientific survey, the dataset and the methodology used. It ends with this brief description of the thesis structure.

The second chapter presents the study area, its geographical location, describes the geological and tectonic setting, particularly the Calabrian Accretionary Wedge and the main turbidite deposits.

The third chapter introduces in general the fundamentals and some important concepts of the multichannel seismic reflection method, including the marine seismic acquisition geometry and the necessary equipment (sources and receivers).

The fourth chapter starts with a brief description of the seismic data processing default flowchart for 2D seismic data, followed by a description of the geometry and acquisition parameters, adopted on the CIRCEE-HR survey, and the preliminary onboard processing flow. This chapter concludes with a detailed description of seismic processing flows used in the scope of this work to improve the seismic imaging, and a comparison of the final processed section with the previous onboard processing.

The fifth chapter describes briefly the global significance, formation mechanisms and classification of the migrating sediment waves. Case studies are presented.

The sixth chapter describes and characterizes in detail the migrating sediment waves observed in the CIRCEE-HR seismic profiles, and concludes with a proposed model for their formation.

Chapter seven presents the main conclusions of this work and several suggestions about possible future work.

Chapter II. Study Area

II.1 Geographical Location

The study area is located in the Ionian Sea, South of Italy and East of Sicily (Figure II.1). It is bounded by the parallels 35º24'N and 38º12'N and by the meridians 15ºE and 18º24'E.

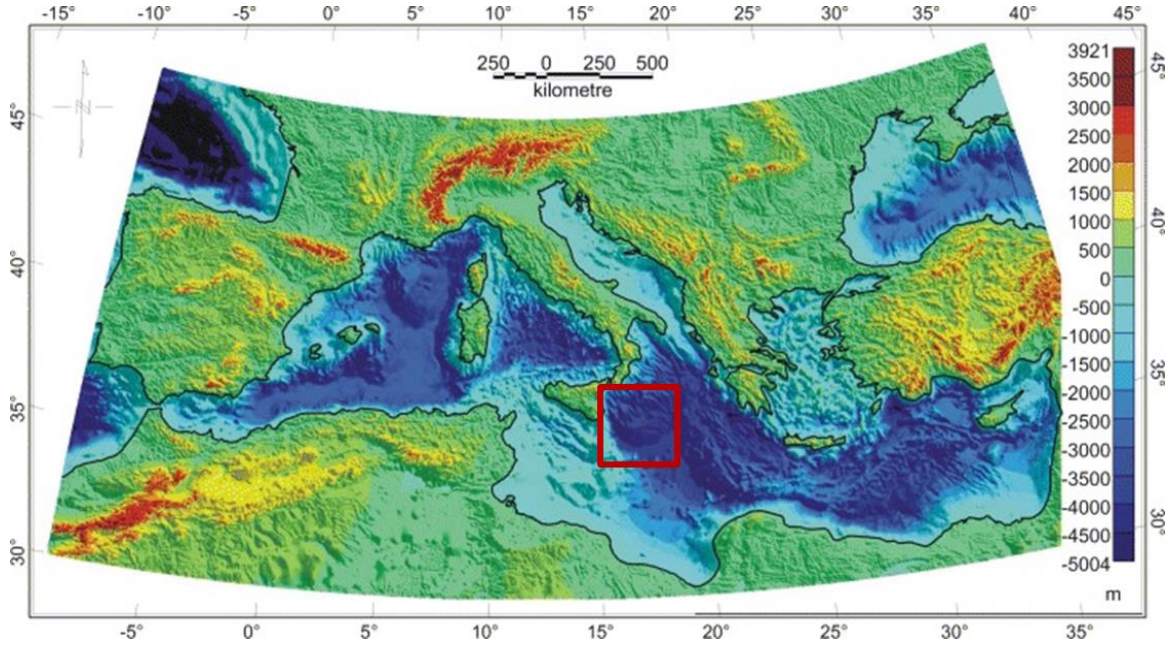

Figure II.1 - Geographical location of the study area (red square). Topographic and bathymetric map adapted from Tontini et al. (2007).

II.2 Geological and Tectonic Setting

II.2.1 Tectonic Evolution of the Western and Central Mediterranean since the Cretaceous

The whole Mediterranean region was subjected to a large-scale rapid pulse of in-plane compressional stress during the Late Cretaceous (~ 95–85 Myr). This event is marked by large scale folding. Soon after this widespread compressional episode, the first evidence of the formation of a trench and the subduction process along the northern, Iberian–European margin occur (Faccenna *et al.*, 2001),

defining the beginning of the closure of Tethys Ocean, formed about 250 Myr ago, upon the rupture of the supercontinent Pangea.

Faccenna et al. (2001) propose a model that discerns the evolution of the Central Mediterranean subduction zone into three phases (Figure II.2): (1) slow initiation, characterized by very low subduction speeds, (2) slab development with a roughly exponential increase of subduction speed and opening of a first back-arc basin; and (3) slow-down due to interaction of the slab with the 660 km transition zone.

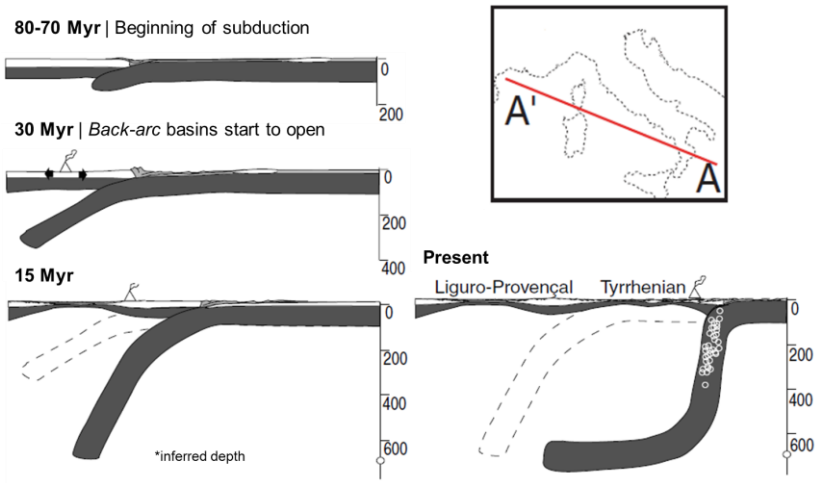

Figure II.2 - Reconstruction, in three phases, of the subduction process along A-A' cut, where it is represented the basins associated with the subduction and its rollback. Modified from Faccenna et al. (2001).

The first phase (80 to 30-35 Myr) is characterized by a very low velocity of subduction (an average of 0.8 cm/yr). Arc volcanism developed when the slab reached a depth of 200-300 km, attaining a shallow dip (Faccenna *et al.*, 2001).

In the second phase (30-35 to 15 Myr), the velocity of subduction and the slab dip increased rapidly; consequently, the arc volcanism increased too. The opening of the back-arc basins gradually starts from north to south (Faccenna *et al.*, 2001; Figure II.3). The first ones began to form, in the Late Oligocene, in the Golf of Lyon, in the Ligurian Sea and in the Valencia Trough. In the Early Miocene, the back-arc extension spread on to the Provençal, Algerian and Alboran basins. The extension in the Western Mediterranean was primarily controlled by the rollback of the subduction zone (Rosenbaum *et al.*, 2002).

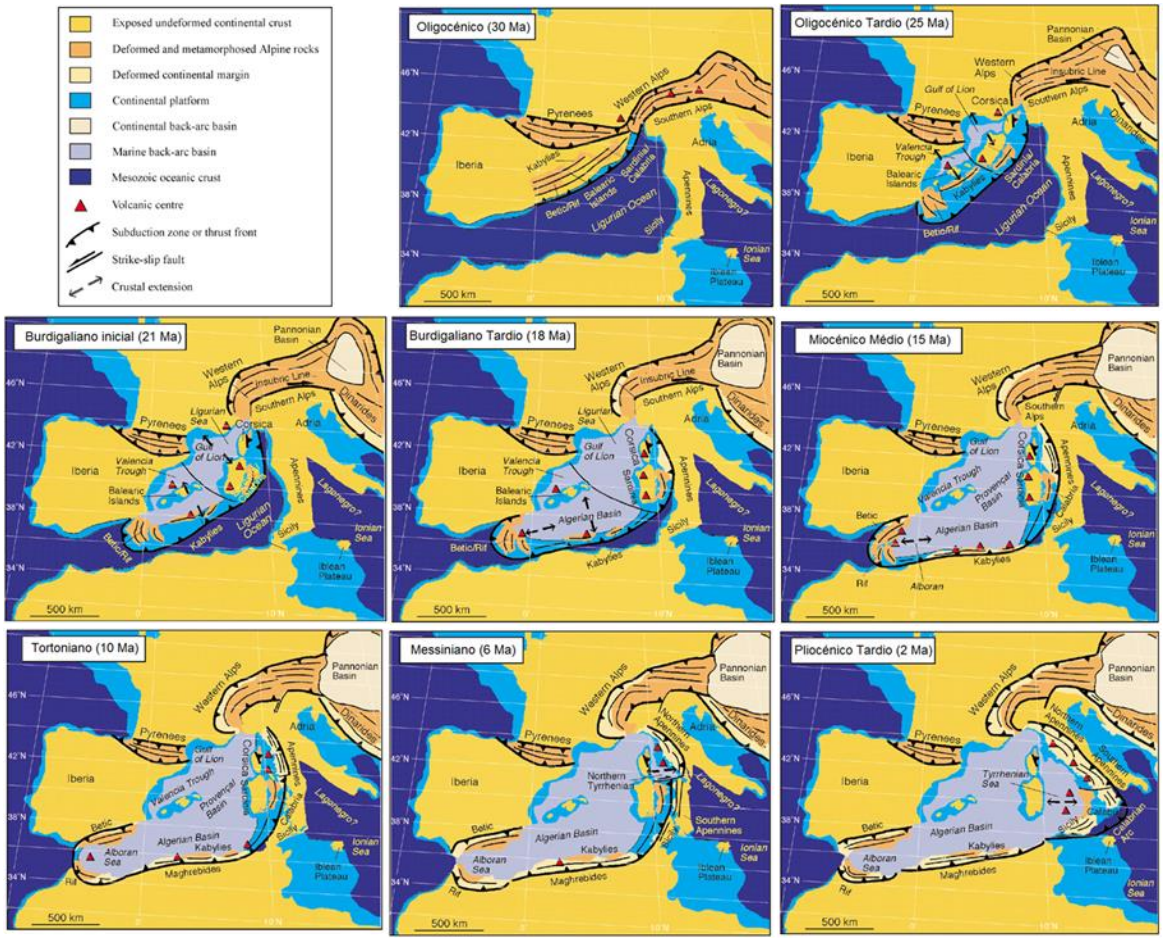

Figure II.3 - Reconstruction of the tectonic evolution of the Western Mediterranean since the Oligocene (adapted from Rosenbaum et al., 2002).

In the third phase (last 15 Myr) the slab reaches the 660 km transition zone. To the south, the slab is deformed due a pause in the subduction (for about 5 Myr) and the subsequent acceleration of the rollback during the opening of the Tyrrhenian back-arc basin, in the Late Miocene (Faccenna *et al.*, 2001).

Rifting led to breakup of continental terranes, which drifted and rotated as long as the subduction zone continued to rollback. Subduction rollback temporally or permanently ceased when continental crust arrived at the subduction zone, impeding subduction processes. The continental terranes have then been accreted to the continents and considerable crustal shortening occurred (Rosenbaum *et al.*, 2002).

II.2.2 The Calabrian Accretionary Wedge

The Calabrian accretionary wedge is a 400 km long and 300 km wide structure, located southeast of Calabria and to the east of Sicily. It is confined between the NNW-SSE trending and 250 km long Malta escarpment and the NW-SE trending Apulian escarpment (Gallais *et al.*, 2012). The Calabrian accretionary wedge developed due to the SE-NW Africa/Eurasia convergence, presently occurring at a very slow rate of about 5 mm/yr or even lower (Polonia *et al.*, 2011).

Based on figures II.4 and II.5, five different morphological domains can be distinguished (from the SE to the NW). An undeformed area beneath the Ionian abyssal plain, distinct from the deformed Calabrian accretionary wedge, located directly to the NW, which comprises the other four domains: the frontal slope, the upper slope, the crest of the wedge and the inner plateau, directly SE of Calabria (Gallais *et al.*, 2012).

The Ionian Abyssal Plain is characterized as a deep triangular basin, roughly defined by the 4000 m depth isobath, bounded to the south by the Medina seamounts. It is a nearly flat domain despite some relief evidences such as the Victor Hensen Seahill and the Victor Hensen Seahill 2 (see Figure II. 5 for location; Gallais *et al.*, 2012).

West and east of the undeformed Ionian Abyssal Plain, the first evidences of deformation are notorious by the increasing roughness of the seafloor (Figure II.4). This morphological change marks the boundary between the undeformed Ionian Abyssal Plain and the frontal slope domain of the Calabrian wedge to the west and of the Western Mediterranean Ridge to the east (Polonia *et al.*, 2011). These boundaries correspond to the deformation fronts of the two accretionary wedges. Short-wavelength folds are well-expressed in the frontal slope, to the NW of the Ionian abyssal plain. These folds vary between 5 and 12 km in lateral extension and show a rather consistent axial N55 trend but veering to N90 further west. To the west, these folds become less well-expressed and a patchwork of small-scale asperities characterizes the seafloor morphology (Gallais *et al.*, 2012).

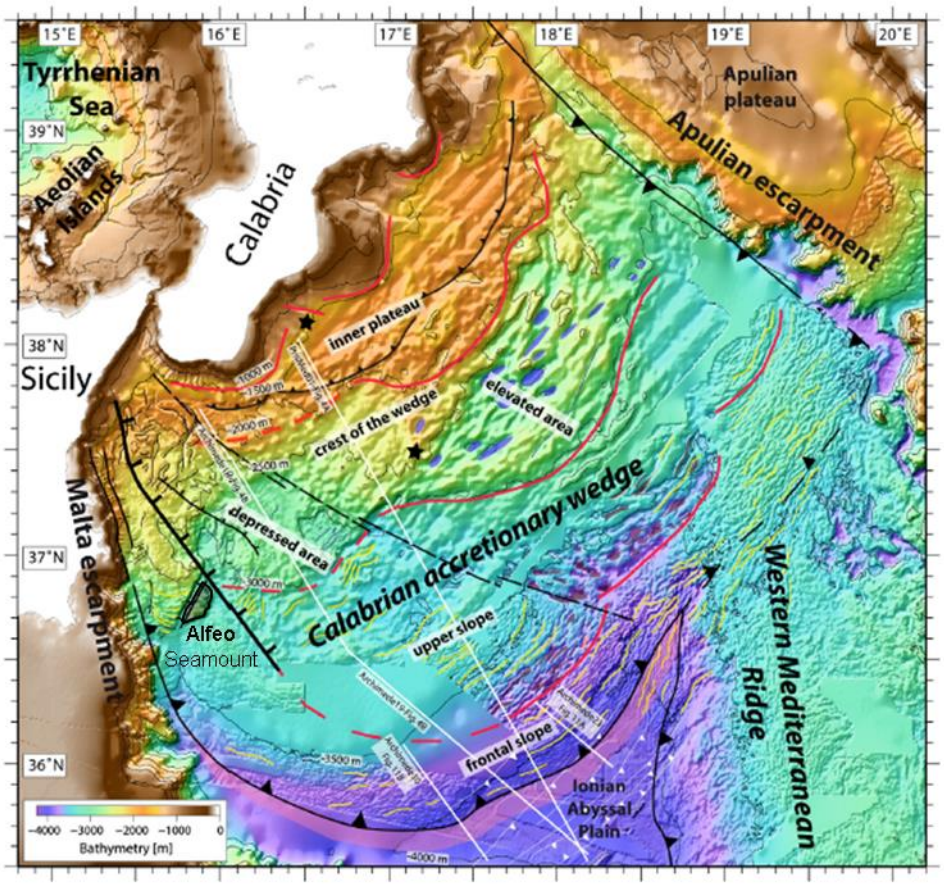

Figure II.4 - Morpho-structural map of the Calabrian accretionary wedge and its adjacent regions. Black lines with black triangles: the deformation fronts of the Calabrian accretionary wedge and of the Mediterranean Ridge. Dark red lines: main morphological boundaries in the Calabrian accretionary wedge. Black dashed lines: the boundary between the elevated and depressed domain of the Calabrian wedge. Black stars: mud volcanoes. Black lines with perpendicular dashes: normal faults. Thin white lines with white triangles: deep reverse faults. Pink area: extent of the proto-thrust domain. Brown area: depressions in the upper slope: Blue area: depressions in the crest of the wedge. Yellow lines: lineaments of the seafloor or axes of anticlinal folds. Black lines: location of the canyons. White lines: location of the multichannel seismic profiles from Archimede cruise (adapted from Gallais *et al.*, 2012).

The frontal slope is a 45-55 km wide domain. It extends approximately from 4000 m to 3800 m depth, directly NW of the Ionian Abyssal Plain and widens to the W from 4000 m to 3500 m depth. The western boundary of this domain terminates against the Alfeo seamount, a small plateau located 30 km east of the Malta escarpment (Gallais *et al.*, 2012).

The boundary between the frontal slope and the upper slope is defined by occurrence of deep gashes on the seafloor, reaching 4000 m depth and separated by bumps (called the cobblestone topography). These gashes represent zones, where the Plio-Quaternary sediments are absent and the Messinian evaporites rise locally as diapirs and pierce to the seafloor. This boundary is difficult to follow to the SW; so, the location of this boundary is based on the observation of the roughness of the seafloor on the seismic profiles (Gallais *et al.*, 2012).

The upper slope extends approximately from 3600 m to 3000 m depth. Landward, the seafloor morphology is characterized as a relativity flat domain, referred as the “slope terrasse” (Polonia *et al.*, 2011; Gallais *et al.*, 2012).

The 3000 m isobaths delineate a small scarp that marks the boundary between the upper slope. Recently, Polonia *et al.* (2011) outlined that the Calabrian accretionary wedge could be segmented longitudinally along a NW/SE trending diffuse boundary that is considered to be a major deformation zone (Figure II.6). To the NE of this zone, an elevated area of the crest of the wedge, located in the “eastern lobe” of the Calabrian prism, and representing a 75 km wide bulge, is observed, affected by SW-NE trending egg-shaped depressions that lie at an average depth of 3500 m. To the SW of the deformation zone, the depressed area, located in the “western lobe” represents a wide nearly flat basin at the toe of the 3000 m depth isobaths. Gallais *et al.* (2012) suggest that the NW/SE trending lineament may not represent a major deformation zone. They propose the different elevations of the two lobes to be linked with the collision between the Calabrian prism and the Mediterranean Ridge, occurring SE of the elevated domain.

The inner plateau is located above the 2000 m depth contours (Polonia *et al.*, 2011). It is a homogenous domain, with several kilometer-scale bumps. This area has been intensively studied because of its mud volcanoes’ activity.

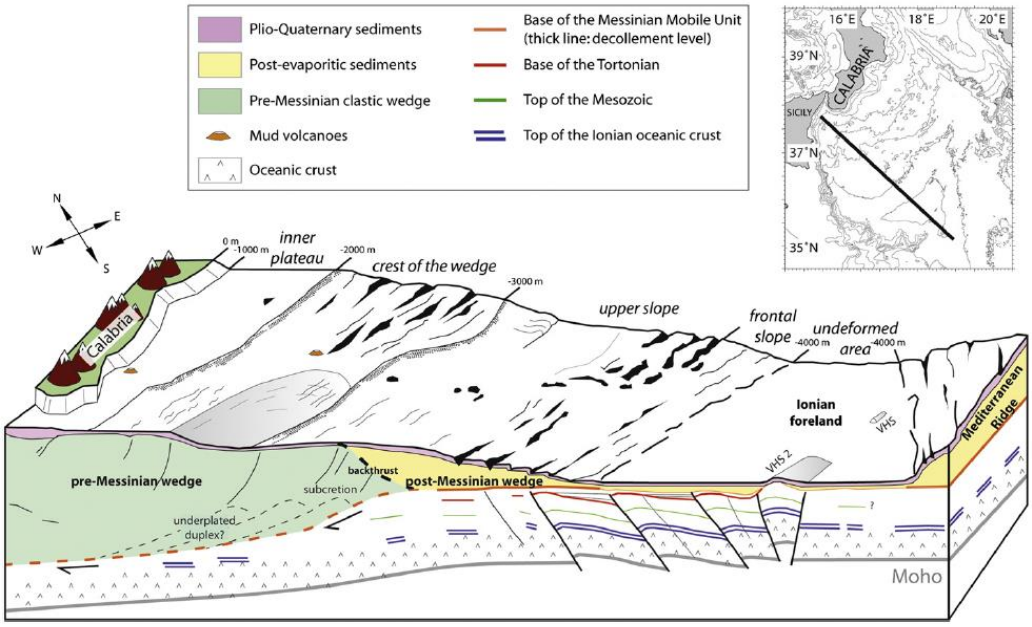

Figure II.5 - Schematic 3D view of the Calabrian accretionary wedge. In italics: the morphological domains. In bold: the associated structural domains. VHS: Victor Hensen Seahill. VHS 2: Victor Hensen Seahill 2. CTZ: Central Transition Zone (adapted from Gallais *et al.*, 2012).

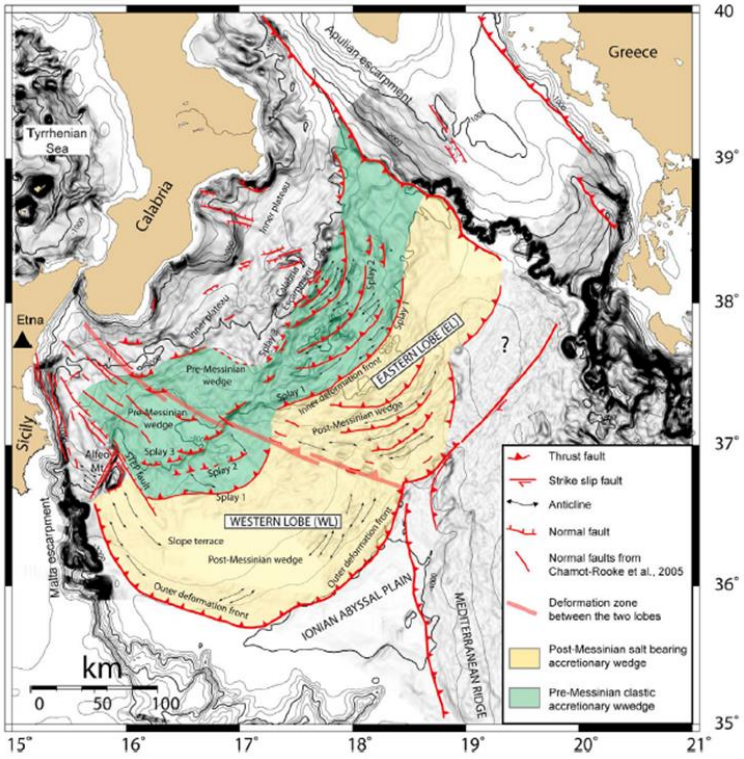

Figure II.6 - Structural map of the Calabrian Arc region. Major structural boundaries, active faults and the extent of the structural domains (i.e., pre and post-Messinian wedges and inner plateau) are indicated. Modified from Polonia et al. (2011).

The Calabrian accretionary wedge can also be divided into two important structural domains: the pre-Messinian and the post-Messinian wedges (Figure II.6; Polonia *et al.*, 2011). The pre-Messinian wedge is located in the inner zone, in the north, and it is constituted by clastic materials from Upper Cretaceous to pre-Messinian (see Figure II.5). The post-Messinian wedge, known as the "salt wedge" too, is located in the most external zone of the Calabrian accretionary wedge, in the south, and it is constituted exclusively by Messinian and Plio-Quaternary deposits. A basal décollement was identified on base of the Messinian deposits. Despite of certain ambiguity, it is proposed that the boundary between these two domains occurs over a "main external ramp" (Minelli & Faccenna, 2010) or a "splay fault" (Polonia *et al.*, 2011; Gallais *et al.*, 2012; Gutscher *et al.*, 2015).

Researchers have been seeking for the lithospheric scale tear fault associated with subduction rollback, presumably located offshore eastern Sicily (Figures II.4 and II.6). Many have proposed the Malta Escarpment to be the active tear fault, primarily due to its striking morphological expression as a 3–4km high step on the seafloor. The exact geometry and degree of activity of the network of faults offshore Sicily remains uncertain and highly controversial; so, there is no consensus on the surface expression of the "STEP" fault (subvertical tear fault). Recently, Gutscher et al. (2015) interpreted a two-part fault system as the shallow tectonic expression of a lithospheric scale lateral slab tear (STEP fault), based in new high-resolution seismic profiles and detailed morphobathymetry (Figure II.7).

II.2.3 Main turbidite episodes

The turbidite currents have played an important role in recent geological history of the Ionian Sea: between 93% and 95% of sediments from Holocene and Late Pleistocene were deposited by turbidite currents, unleashed mainly by regional seismic activity (Polonia *et al.*, 2013). Between the several turbidites that have been identified in the Ionian Sea basin, the mega-turbidites are the ones that deserve special attention because they are indicators of soil acceleration due to seismic events, impacts of tsunamis waves in the seafloor, volcanic activity, sea level changes, phase changes and gas hydrates dissociation, or even the combination of any of these processes (Polonia *et al.*, 2013).

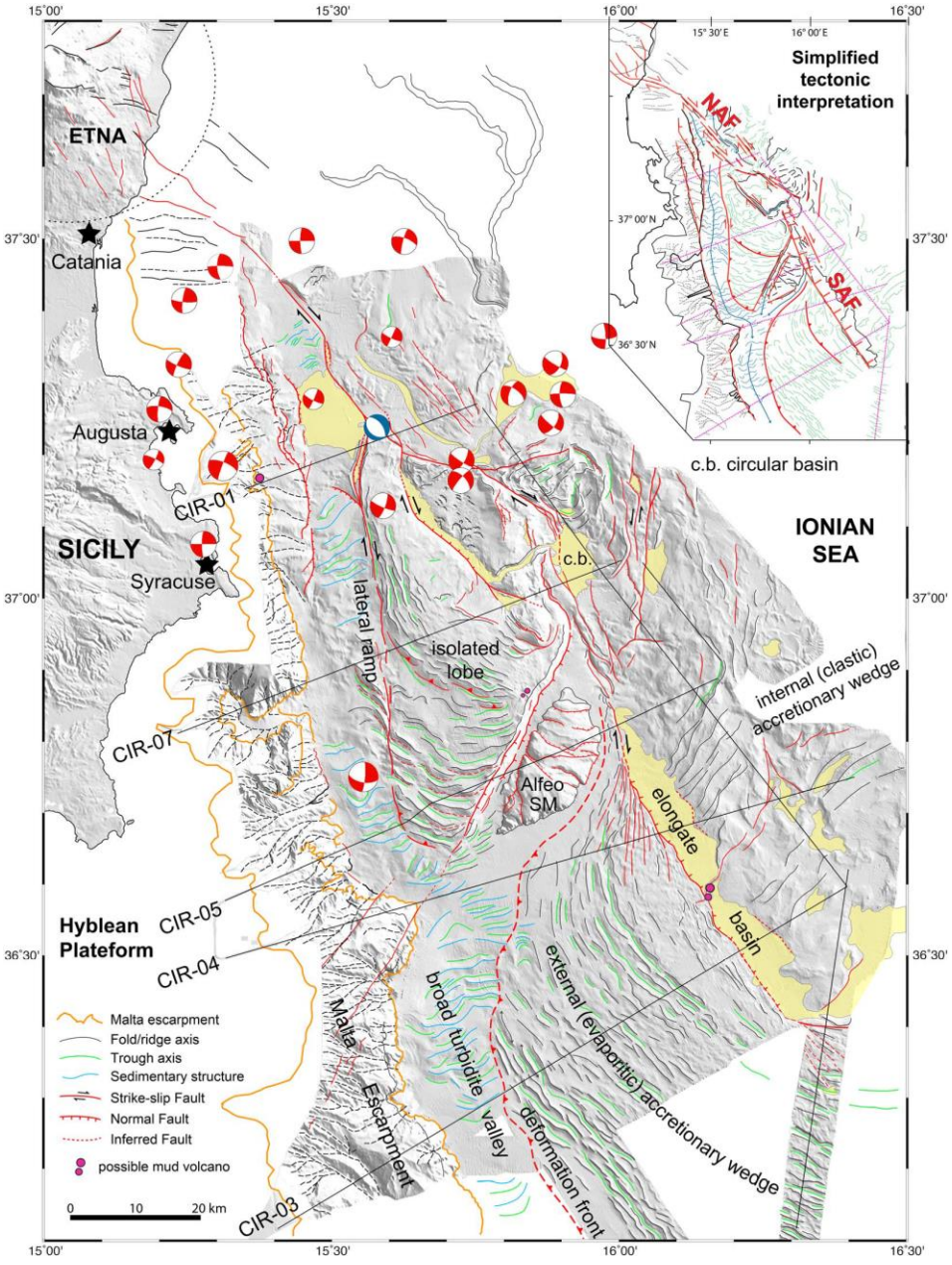

Figure II.7 - Morphobathymetric interpretation map, in east offshore Sicily, showing: position of CIRCEE-HR seismic profiles (straight black lines), sediment waves (alternating green and blue lines), accretionary wedge anticlines and synclines (black and green lines), likely faults (red lines), the upper and lower limits of the Malta Escarpment (orange lines), flat lying sedimentary basins (yellow shading), and earthquake focal mechanisms from a published study [Musumeci et al., 2014]. Simplified morphotectonic interpretation. Symbols: minor thrust faults in the accretionary wedge (green lines); sedimentary structures, (blue lines); basin boundaries and other tectonic lineaments (black lines); major faults (red lines) with kinematics indicated (barbs for normal faults, arrows for strike-slip faults, teeth for thrust faults) NAF = North Alfeo Fault system and SAF = South Alfeo Fault system; position of seismic profiles (straight magenta lines) (Gutscher et al., 2015).

Moreover, they should have an important role in the formation of the migrating sediment waves investigated in this study.

Three major transparent layers were identified in the region: Homogenite/Augias turbidite (HAT), Deep Transparent Layer (DTL) and Thick Transparent Layer (TTL) (Hieke, 2000; Bortoluzzi *et al.*, 2016; Figure II.8). The HAT and the DTL ages were reconstructed trough ^{14}C dating and they are about 1651 yr b.p. and 14000 yr b.p., respectively (Polonia et al., 2013). Using the average sedimentation rate for the Pleistocene in the Ionian Abyssal Plain (about 15 cm/1000 years; Cita et al., 1978), Hieke (2000) roughly estimated the age of TTL to about 650 kyr ± 100 kyr.

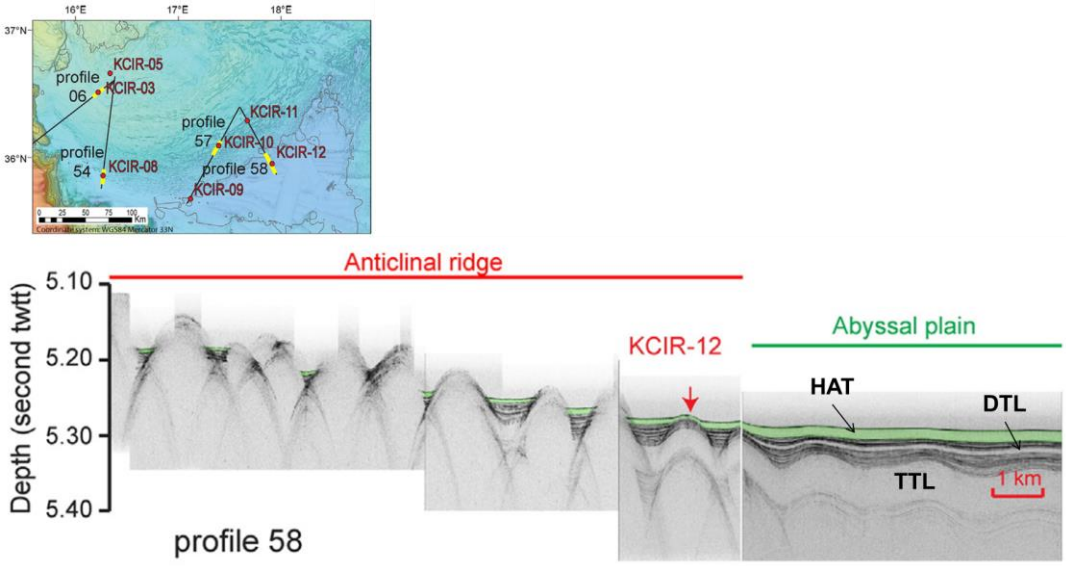

Figure II.8 - Chirp echosounder profile 58 showing three major turbidity deposits as acoustically transparent layers (CIRCEE data). In green: Homogenite/Augias turbidite (SanPedro et al., 2016).

The Augias mega-turbidite

The Augias mega-turbidite, also designated “homogenite” (due to the sediment homogeneity), was described for the first time by Hieke *et al.* (1975). It is characterized by a significant content in aragonite, which is restricted only to this turbidite (Hieke & Werner, 2000). Its thickness varies between 20 to 25 meters (Polonia *et al.*, 2013). The Augias covers the Ionian and Sirte Abyssal Plains and the lowermost slopes of the adjacent Calabrian and Sirte Rises and the Mediterranean Ridge (Figure II.9; Hieke & Werner, 2000).

The first hypothesis about the formation of this mega-turbidite pointed to the eruption of Santorini (3500 years ago) as the trigger event. The evolution of tsunami modelling led to question of the effectiveness of the tsunami wave generated by the Santorini caldera collapse, especially outside the Aegean Sea. Thus, it was proposed that the Augias was generated by a tsunami driven by the collapse of eastern flank of the Etna Volcano (7600 years ago). After several criticisms to these hypotheses it was suggested the possibility of this mega-turbidite be related with an important earthquake in Crete in 365 DC (Polonia *et al.*, 2013).

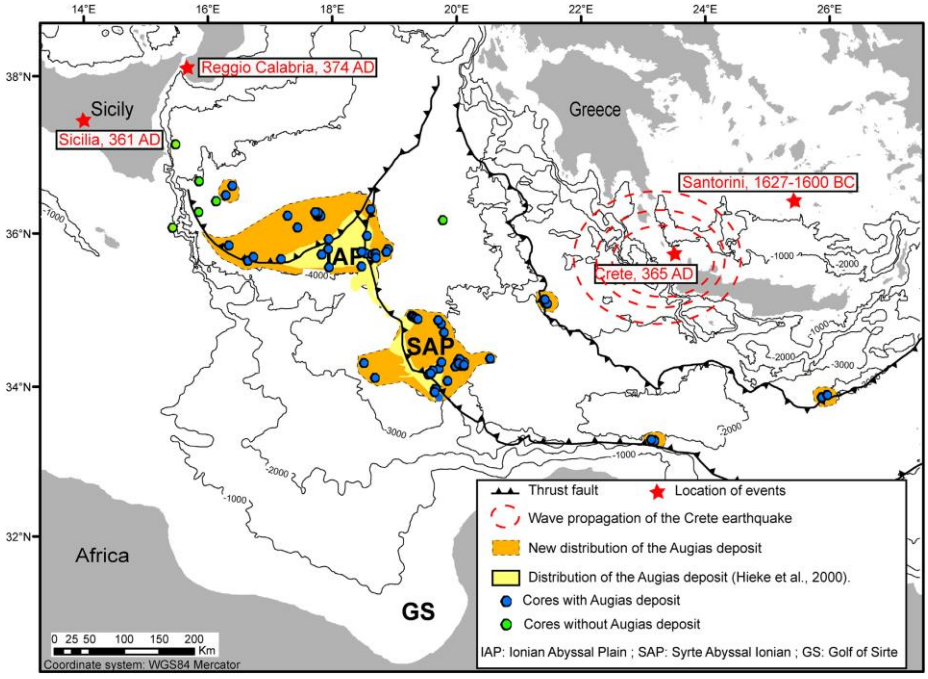

Figure II.9 - Distribution of the Augias deposit based on seismic profiles (yellow from Hieke *et al.,* 2000) and on sediment cores described by Cita *et al.* (1996), Hieke (2000), Polonia et al. (2013) and CIRCEE-HR data. Red stars represent the hypothesized epicenters for the origin of the Augias deposit (adapted from San Pedro *et al.*, 2016).

Polonia et al. (2013) concluded, after a careful study, that the event that caused the formation of the Augias happened between 215 and 530 AD, thus excluding the first hypotheses of the eruptions of Santorini and Etna. Indeed, the only historical earthquake potentially capable of generating devastating effects in the Ionian Sea, in the Sirte abyssal plain and in the Herodotus Trough during the given time interval was the Cretan 365 AD earthquake.

Chapter III. The 2D Marine Seismic Reflection Method

III.1 Basic Principles and Fundamentals

In the seismic reflection method, the structure of the subsurface geological formations is mapped by measuring the time required for a seismic wave (or pulse) emitted at or near surface to return to the surface after reflection on the interfaces between formations, which have different physical and acoustical properties (density and P-wave velocity). The incident wave at an interface is split into a reflected and a refracted part (Figure III.1), according to the Snell's Law (Equation 1):

$$\frac{\sin(\theta_i)}{\sin(\theta_r)} = \frac{V_1}{V_2} \qquad \text{(Eq. 1)}$$

where θ_i is the incident angle, θ_r is the refracted angle, and V_1 and V_2 represent the velocity of the seismic waves in two different media.

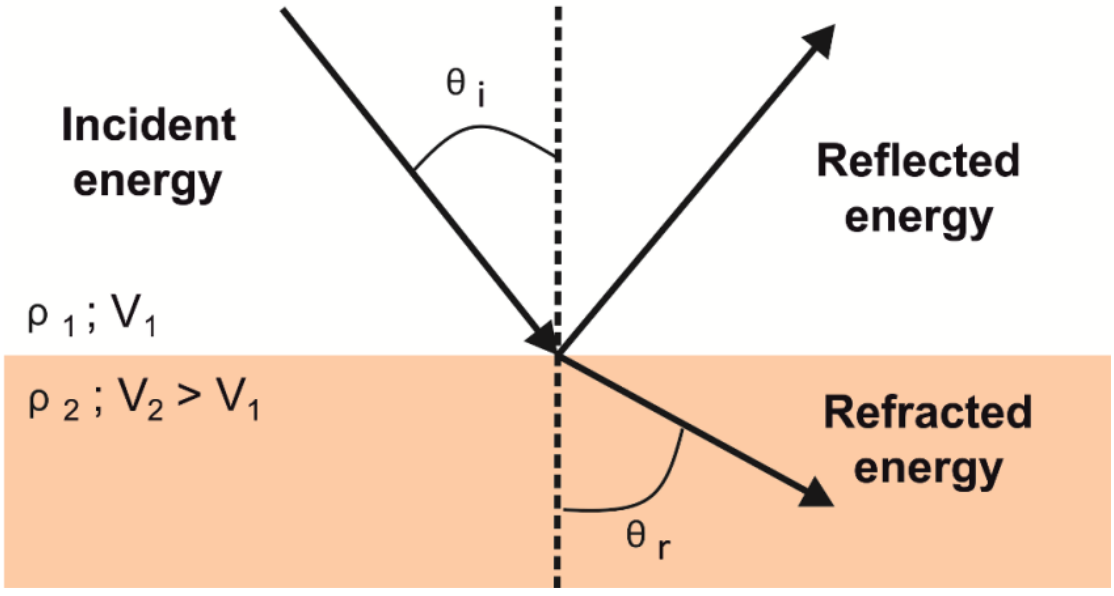

Figure III.1 - Partial reflection and partial refraction of a P-wave between two media with different physical properties for the simplified case in which there is no P to S wave mode conversion. V_i and ρ_i represents the velocity of the seismic waves and the density of the layers, respectively.

The travel-time of the reflected waves from the source until they are recorded by the receivers is used to derive information about the subsurface geology, as well as the rock properties and the layers attitude. The time that a wave takes to travel since it is generated at the source, finds an interface between two layers with different density (ρ), seismic wave velocity (V), where it is reflected, and travels back to the surface where it is recorded by the receivers, it is called two-way travel-time (TWT). The Reflection Coefficient (RC) is proportional to the acoustic impedance (Z) contrast between two layers and is given by Equation 2 – for the case of normal incidence (for the general case it will depend on the angle of incidence and mode conversion has to be taken into account – see, for example, Yilmaz, 2001a):

$$RC = \frac{\rho_2 V_2 - \rho_1 V_1}{\rho_2 V_2 + \rho_1 V_1} = \frac{Z_2 - Z_1}{Z_2 + Z_1} \qquad \text{(Eq. 2)}$$

The seismic resolution is largely determined by the acquisition system characteristics, the acquisition geometry and the properties of the media of propagation. Subsequent processing can improve the image resolution within some limits. Therefore, seismic resolution is a matter of prime importance in seismic data acquisition (Yilmaz, 2001a).

Vertical resolution

The vertical resolution of a seismic wave is a measure of its ability to recognize individual, closely-spaced reflectors and is determined by the pulse length of the record seismic section. The vertical resolution increases with increasing wave frequency. Higher frequencies mean sharper pulses and therefore better vertical resolution. Two reflectors can be recognized as separated seismic events only if the distance between them is at least ¼ of the wavelength (λ) of the seismic wavelet, defined by (Equation 3):

$$\lambda = \frac{V}{f} \qquad \text{(Eq. 3)}$$

where V is the seismic wave velocity in the layer and f is source frequency.

The frequency of waves transmitted into the Earth depends on the type and characteristics of the seismic source. However, the frequency changes as the waves travel in the subsurface and the seismic wave will lose higher frequencies in depth since they are more rapidly absorved. Therefore, high-frequencies waves are attenuated much faster than low-frequencies. The higher the frequency the lower will be the penetration, but the higher will be the vertical resolution.

Horizontal resolution

The horizontal resolution of a seismic wave is mainly controlled by the so-called "First Fresnel Zone" (Figure III.2). The Huygens ' Principle states that each part of a wavefront acts as a source of a new wave and the area where the waves interfere with each other constructively is the area of interest, called the "First Fresnel Zone" (Sheriff, 1991, 1996). The radius of the First Fresnel Zone, FR, is given by:

$$FR = \frac{V}{2}\sqrt{\frac{t}{f}} \qquad \text{(Eq. 4)}$$

where V is the average seismic velocity on the layer, t is the wave two-way travel-time, and f is the frequency of the seismic waves. Thus, the Fresnel zone increases, and consequently horizontal resolution decreases, with increasing velocity, increasing travel-time (depth) and decreasing signal frequency.

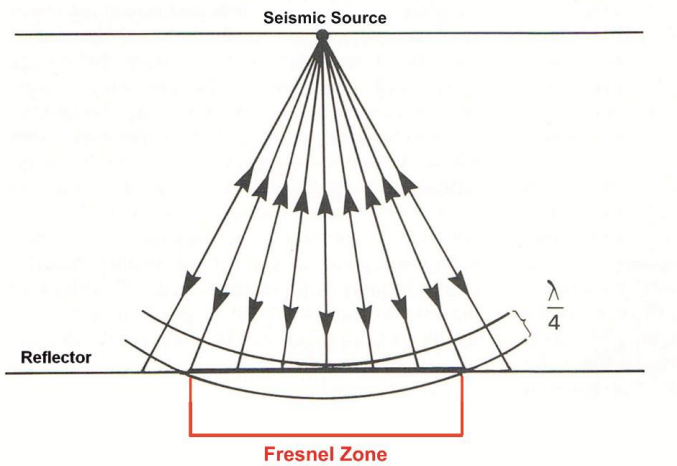

Figure III.2 - Schematic representation of the 1st Fresnel Zone. The energy is returned to the receiver from all points of the reflector. The part of the reflector which the energy is reflected within

half of wavelength of the initial reflected arrival is known as the First Fresnel zone (Kearey and Brook, 1991).

III.2 2D Multichannel Seismic Reflection Surveys

In the 2D multichannel marine seismic acquisition a long seismic streamer of hydrophones and a seismic wave source are towed behind the seismic vessel. The streamer will receive and convert the reflected waves that come from the sea subsurface to an electrical signal. The reflections from the subsurface are assumed to come directly from below the navigation line performed by the research vessel.

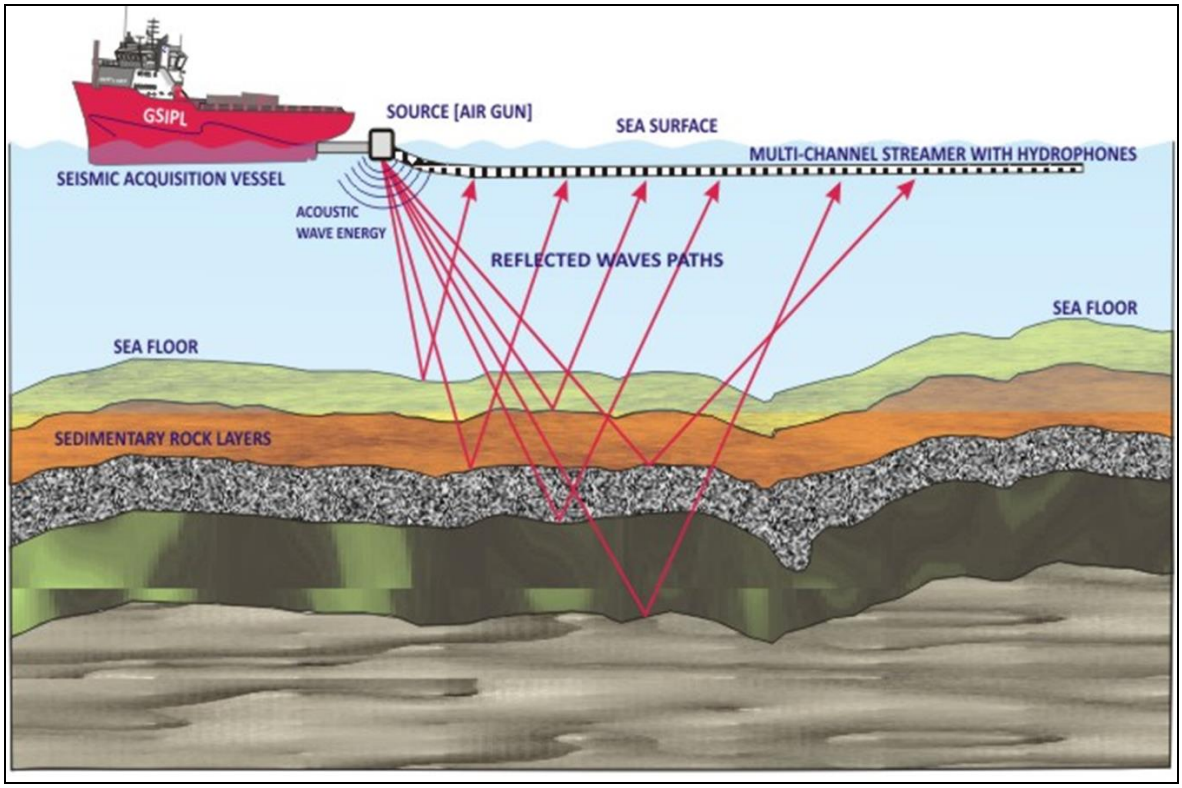

Figure III.3 - Typical 2D multichannel seismic reflection survey (modified from http://geostar-surveys.com).

III.2.1 Marine Seismic Sources

The most widely-used seismic sources in multichannel seismic surveys are the airguns. The airguns are devices that release a high-pressure bubble of compressed air underwater that acts as a source of energy to generate the

acoustic/pressure waves that are used in seismic reflection surveys. The primary pulse generated by an airgun is followed by a train of bubble pulses that increase the overall length of the pulse (McQuillin *et al.*, 1984; Dobrin and Savit, 1988, Telford *et al.*, 1990). This effect is called the "bubble effect" and it gives an oscillatory and, unsatisfactory reflection record. Special measures are adopted in the design of the seismic array and in the individual airguns time shooting, as well in the processing stage to attenuate the bubble oscillations.

The airguns used in the CIRCEE-HR survey were GI airguns (G – Generator; I – Injector). This type of sources was developed to reduce and suppress the bubble oscillation (Figure III.4 and III.5).

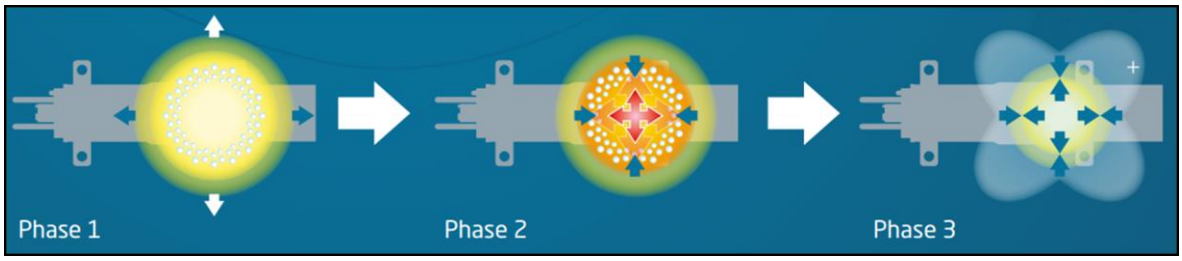

Figure III.4 - In phase 1, the Generator is fired. The blast of compressed air produces the primary pulse and the bubble starts to expand. In the second phase, just before the bubble reaches its maximum size, the injector is fired, injecting air directly inside the bubble. At last, the volume of air released by the injector increases the internal pressure of the bubble and prevents its violent collapse. The oscillations of the bubble and the resulting secondary pressure pulses are reduced and reshaped (in *www.sercel.com*).

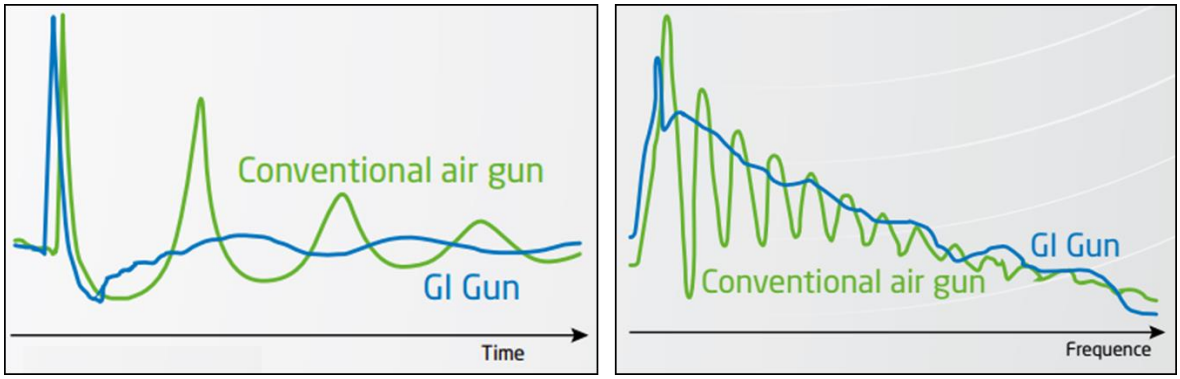

Figure III.5 - Comparison of acoustic signature between a conventional airgun and a GI airgun. The peak-to-peak is reduced due to the volume of the Generator; the primary-to-bubble ratio is greatly increased, thus resulting in a clean acoustic signature and in an almost total suppression of the bubble oscillation (in *www.sercel.com*).

III.2.2 Marine Seismic Receivers

To receive and record the seismic reflected waves a long hydrophone cable, called streamer, is used. This cable consists of a plastic tube, 5 to 8 cm in diameter, nearly neutrally buoyant and generally filled with querosene. The hydrophone elements, wires and transformers are stored inside the plastic tube, which is acoustically transparent and generally also optically transparent. The seismic wave passes through both the plastic tube and the oil and reaches the hydrophones without noticeable interference (Dobrin and Savit, 1988).

Within the hydrophone a piezoelectric transducer produces an electrical signal in response to the pressure changes caused by the passage through the surrounding water of the seismic pressure waves (Dobrin and Savit, 1988). Hydrophones are arranged in sections (“live sections”, or channels). Each hydrophone from each live section receives a seismic signal which is summed up together and the final result is considered the seismic record for that live section, receiver group or channel. With this summing (stacking) technique the signal to noise ratio is largely improved.

The streamer is divided into several components. Among the benefits of using streamer incorporations, such as lead-in sections, birds (to stabilize the streamer at a certain depth) as well as other noise-reducing design systems is that marine surveys can now be conducted at higher tow speeds and in rougher weather conditions; also improved signal to noise ratio is obtained, which allow the geophysicist to get deeper information and better imaging after data processing (Dobrin and Savit, 1988).

III.2.3 Multi-Fold Coverage Marine Seismic Acquisition

Multi-fold coverage in a multichannel seismic survey, means that for different shots, the reflections from each reflecting point along the reflector interface are recorded in more than just one seismic trace.

Figure III.6 illustrates how the seismic data is acquired in a way which allows multifold coverage and consequently stacking during conventional processing. The

geometry of acquisition is set in a way that a set of traces recorded at different offsets for different shots contains reflections from a common midpoint (CMP) on the same reflector. The CMP is the point at the surface located at half-offset between the source and the receiver that is common to several source-receiver pairs.

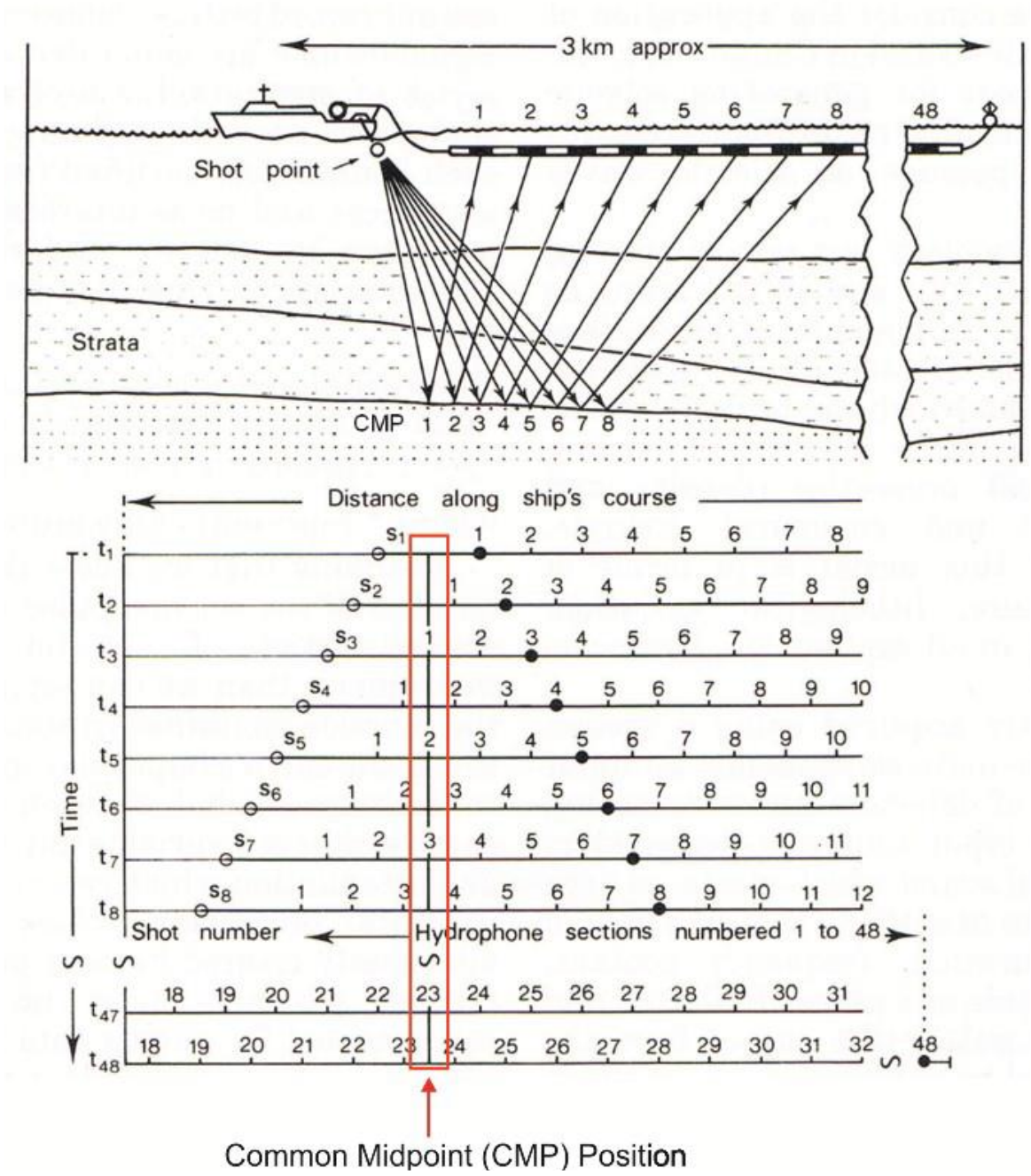

Figure III.6 - Diagram showing the multichannel marine seismic acquisition geometry with multi-fold coverage technique (modified from McQuillin et al., 1984).

The CMP gather (Figure III.7b) is formed by all the traces from the source-receiver (S_i-R_i) pairs that correspond to the same common reflections points. The fold refers to the number of traces in the CMP gather that can be summed. It can be expressed as a percentage (e.g. six-fold = 600% fold coverage) or by the number of times the same CMP is sampled (e.g. 20-fold). So, the larger the fold the better will be the data quality.

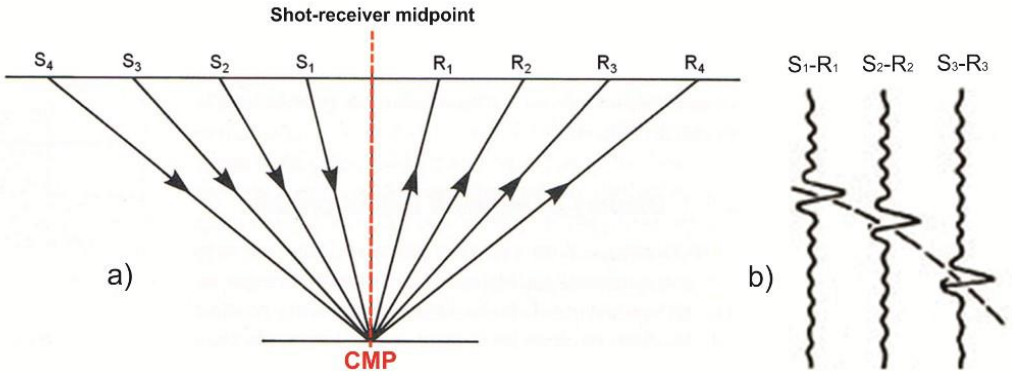

Figure III.7 – Shot-Receivers (S_i-R_i) pairs that share the same reflection point (figure (a)) and an example of CMP gather of three S-R pairs (figure (b)). Modified from Kearey and Brooks (1991).

This method brings a significant improvement in the signal-to-noise ratio, attenuating or almost suppressing totally the long-path multiples (Yilmaz, 1987; Kearey and Brooks, 1991; Yilmaz, 2001a). For inclined reflectors, the necessary corrections can be partially done through post-stack migration or correctly handled through pre-stack migration (Yilmaz, 2001a)

III.3 The Nature of Seismic Traces

Nowadays, the seismic trace corresponds to a digital signal that can be viewed as the convolution of a reflectivity function with a source wavelet, as shown on Figure III.8. A negative reflection coefficient occurs at a decrease in acoustic impedance across an interface.

In practice, the seismic trace also contains contributions of undesirable nature, in particular: (1) Multiple reflections, (2) Coherent noise and, (3) Random noise (Hatton *et al.*, 1986).

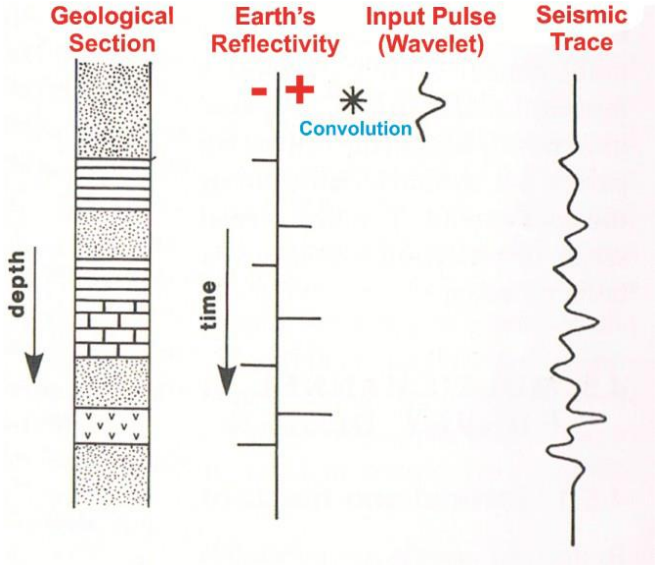

Figure III.8 – The seismic trace as the convolution of the source wavelet by the subsurface reflectivity function (modified from Kearey and Brook, 1991).

Multiple reflections

When the incident wave reflects in more than one interface in its travel path it is called a "multiple". Two classes of multiples can be distinguished: long-path and short-path multiples (Sheriff and Geldart, 1995). A long-path multiple is one whose travel path is long compared with primary reflections from the same deep interfaces, appearing as a separate event on a seismic record. Short-path multiples include the so-called ghost reflections (Figure III.9).

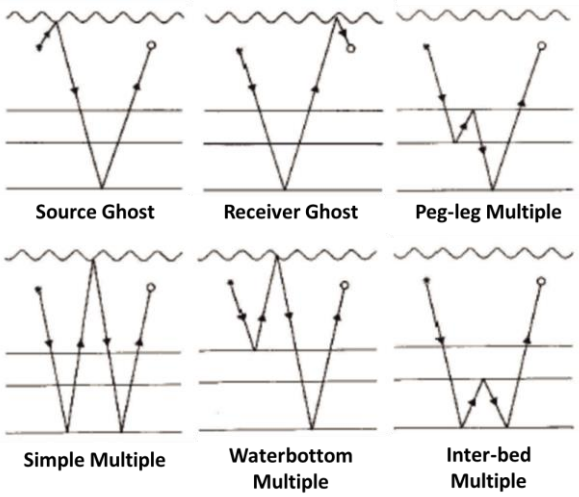

Figure III.9 - Ray paths of some common multiples families (modified from Hatton et al., 1986).

Coherent noise

According to Hatton *et al.* (1986) examples of coherent noise are: (1) direct waves, (2) diffracted waves, (3) refracted waves, (4) vibrational noise and, (5) interference.

The common characteristic of this kind of noise is the line-up of energy in a distinguishable manner across the traces of a shot gather (Larner *et al.*, 1983). 2D filtering techniques can be applied to attempt their attenuation.

Random Noise

Random noise exhibits no correlation from trace to trace, and no specific noise amplitude can be predicted from the knowledge of the generating mechanism. It can be generated by (1) Instrument noise, (2) Machinery, (3) Power lines, and (4) Cable noise.

Improvements in the design of seismic vessels, instruments and cables are continually reducing the effect of the various types of noise described above. Methods of random noise reduction are based on averaging techniques and frequency filtering (Hatton *et al.,* 1986).

Chapter IV. Multichannel Seismic Data Processing of the CIRCEE-HR Survey

Standard seismic processing flows have been fully completely implemented and are well known in the academia and industry to increase the seismic vertical resolution, improve the signal-to-noise ratio of the data and display the seismic events in their correct spatial position, in order to obtain a better imaging of the desired geological information contained in the seismic data (McQuillin *et al.*, 1984; Dobrin and Savit, 1988; Kearey and Brooks, 1991; Yilmaz, 2001a, b).

A common basic processing flow for 2D seismic data (Figure IV.1) is ordinarily composed of a preprocessing stage involving demultiplexing (if required), quality control and trace editing, amplitude and geometry corrections, followed by a processing sequence which normally includes: deconvolution, CMP sorting, velocity analysis, normal moveout correction, CMP stack and migration (Yilmaz, 2001a).

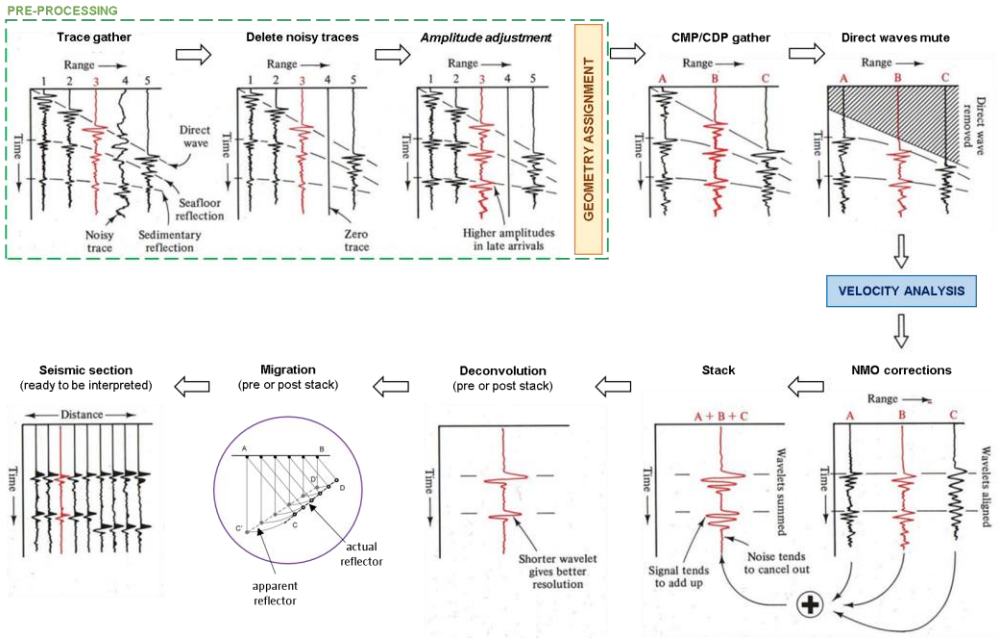

Figure IV.1 - Default seismic data processing flowchart (modified from Klemperer & Peddy, 1992).

All the processing steps should be quality controlled through the seismic processing job in order to ensure that the quality of the data is not diminishing

during the seismic data processing (Yilmaz, 2001a,b). For areas with complex geometry and where acquisition was carried out with long offsets to provide good velocity control, pre-stack migration processing can significantly improve the data, although at a computational cost.

IV.1 Acquisition Parameters

In seismic data processing, the correct definition of the acquisition parameters is fundamental to obtain a good and accurate processed seismic profile. During the acquisition geometry assignment stage, parameters such as the shooting interval, the channel spacing and the source-receiver offset are extremely important, since without them the seismic processing cannot be correctly performed. Besides the parameters already mentioned, it is required to know the sampling interval and the record length of the acquisition system. The tow-depths of the seismic sources and the receivers are also needed to correct for the statics; the SEGY files provided for the seismic processing of this work already have this correction applied.

The acquisition parameters of the CIRCEE-HR scientific cruise and the sources and streamer configurations are schematically represented in Figure IV.2 and in Figure IV.3, respectively.

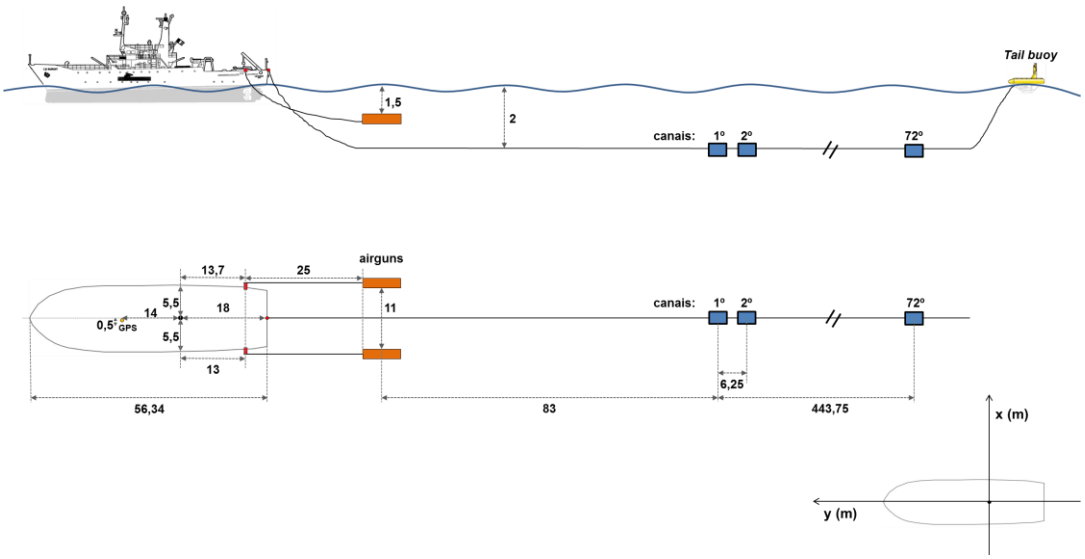

Figure IV.2 - Acquisition parameters of the CIRCEE-HR multichannel seismic survey (Gutscher *et al.*, 2013, 2015).

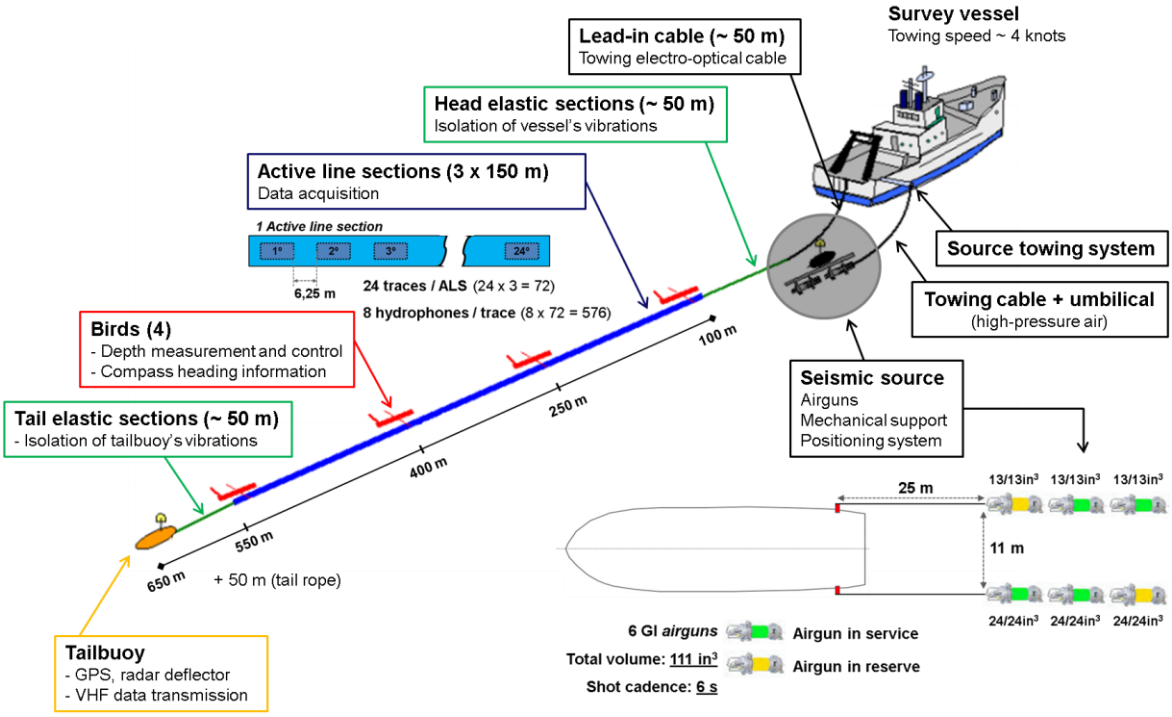

Figure IV.3 - Seismic sources and streamer configuration of the CIRCEE-HR multichannel survey (Gutscher *et al.*, 2013, 2015; modified from www.flotteoceanographique.fr).

IV.2 Preliminary Onboard Data Processing

Preliminary seismic data processing of all the 2D multichannel seismic lines acquired during the CIRCEE-HR survey was performed onboard during the acquisition cruise using the following software: (1) the SISPEED v5.2 software (Ifremer), used in the quality control (QC), and (2) the Seismic Unix software package used in the subsequently seismic data processing steps (filtering, stacking and time migration). This preliminary processing was performed by L. M. Pinheiro (University of Aveiro) and B. M. de Lepinay (National Center of Scientific Research, Nice), responsible for seismic data processing on the second leg of the survey.

Eighteen seismic profiles (representing a total of 1505 km) were acquired in the CIRCEE-HR survey. Due to computational limitations most of those profiles were divided into two or three sections, thus making the data processing more convenient. The seismic lines were recorded in demultiplexed SEG-D format which consists of one file per shot. All files contain a general header (usually

called trace header), with information from each channel of the streamer and also from the birds. The SISPEED software was used to explore the SEG-D files, not only for quality control tool but also for the first fundamental processing stages.

The adopted onboard processing flow was composed by the following stages: (1) navigation processing; (2) source location; (3) quality control and spectral analysis; (4) delay estimation of the sources (air guns' synchronization); (5) conversion of the SEG-D files to SEG-Y; applying a 20-800Hz filter for frequency preservation; (6) common depth point (CDP) calculation; binning and fold determination; (7) CMP gather visualization to determine the NMO's constant velocity (it was used an velocity of 1540m/s); (8) CMP stacking and filtering (70-425Hz); (9) Stolt migration, with a constant velocity of 1540 m/s; (10) sea bottom picking and mute; (11) signal-to-noise ratio (S/N) determination.

IV.3 Seismic Data Re-Processing

One of the objectives of this thesis was to learn the seismic processing techniques, become familiar with standard processing software and reprocess the original multichannel seismic data to try to improve the imaging quality, particularly in the deeper parts of the sections, since the upper part is already very well imaged. The short maximum offsets recorded, however, strongly limit the improvement of the imaging quality. For seismic processing, the Seismic Processing Workshop software (SPW), version 3, from Parallel Geoscience Corporation, was used. One of the first tasks in this thesis was therefore to get familiar with this software and implement the adequate processing flows.

As an example of the flowcharts used, we show below those used for the seismic profile 14.

IV.3.1 Flow 01 – Import

The processing flow **01 – Import** is composed by the following processes: *SEGY Import*, *Clipping*, *Trace Sample Math*, *Resample Seismic* and *Apply Static Shifts*.

SEGY Import

SPW 3 uses the SEG Y format as its internal processing file format, although data may be read in from other formats, such as SEG 2 and SEG D. By default, the SEG Y Standard format file delivered as part of the SPW 3 installation is used for decoding the SEG Y files.

In Processing Categories, the Seismic Data step was first selected, followed by SEG Y Import. A double click on this last item opens the SEG Y Import Dialog (Figure IV.4). The SEG Y seismic file to be used was selected (profil141.seg) and the SEG Y Index was rebuilt. An index file is created for each SEG Y file used in SPW. These files contain important information used in the processing and are required for processing and display. From the list of SEG Y index fields, three were selected: Trace sequential number, Field file number and Channel number. After that, the SEG Y Index was ready to be rebuilt. It was saved in XML file format.

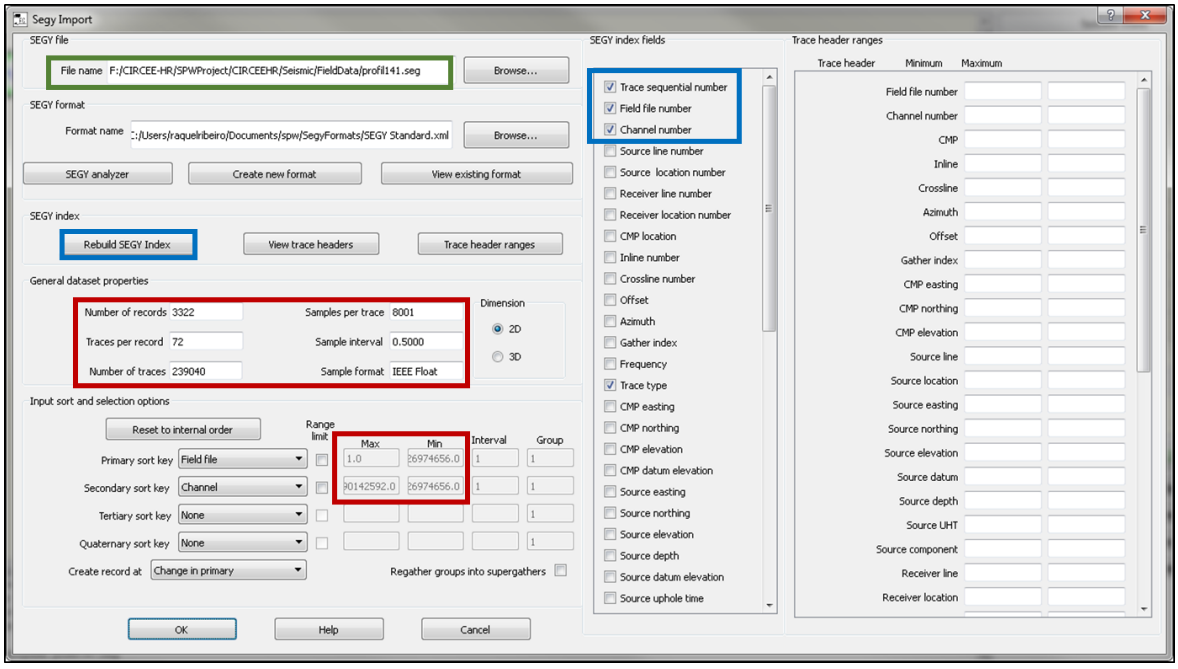

Figure IV.4 - The SEG Y Import dialog in SPW 3 flowchart.

After the SEG Y Index rebuilding, the general dataset properties are shown. They must be checked and confirmed before moving on to the next step. A few odd strange values were detected in the primary and secondary sort keys, and these

were corrected before the next processing step. An output seismic file allows to run the flow and to visualize the seismic profile (Figure IV.5).

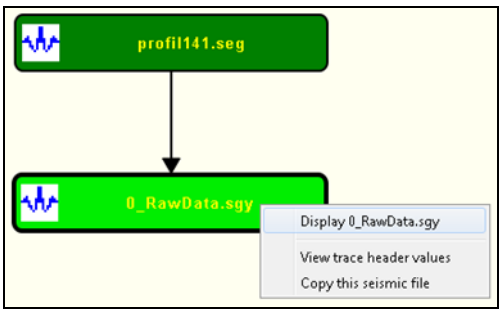

Figure IV.5 - Running the import flow and displaying the seismic file.

In the shot gather display and channel display, odd amplitude values in the original file also appeared in the SEG Y Import dialog. Therefore, it was not possible to visualize the data in True Amplitude (Figure IV.6). It was observed that the reference value of amplitude was too high. It was therefore necessary to reduce this reference value; probably it is one, or just a few, very high amplitude values, which have influenced the amplitude and visualization. The data was hence rapidly analyzed in relative amplitude (Figure IV.7 and IV.8).

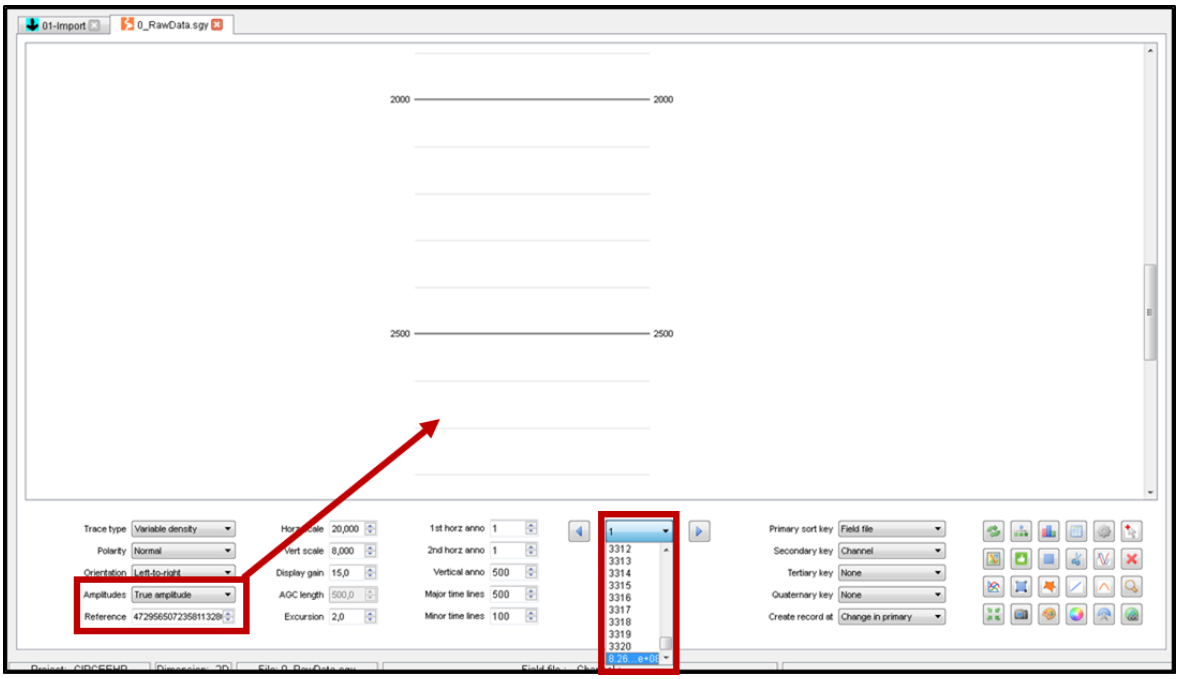

Figure IV.6 - Shot gather display for profile 14, using True Amplitude.

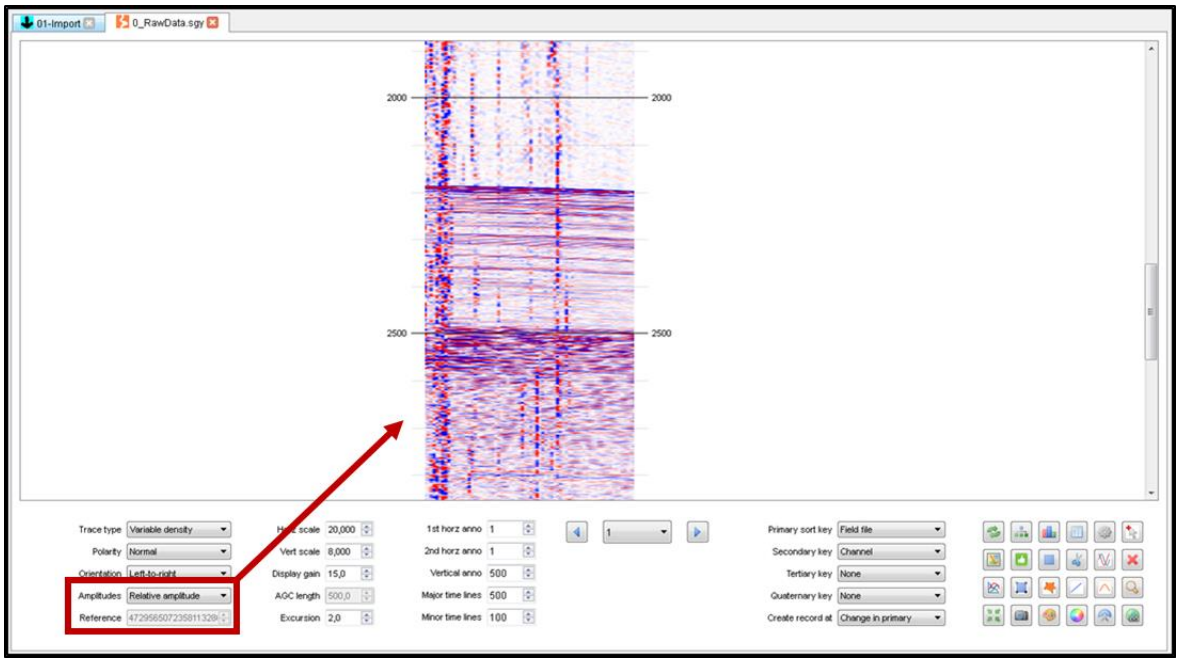

Figure IV.7 - Shot gather display from Figure IV.6 using Relative Amplitude.

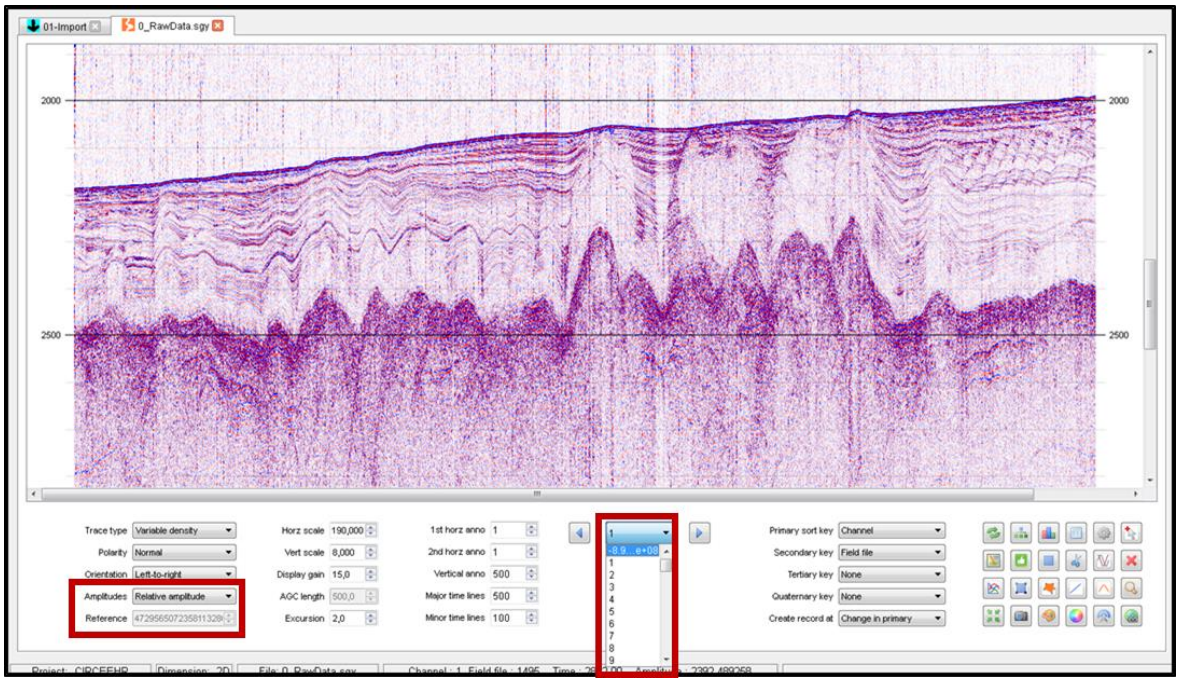

Figure IV.8 - Channel gather display for profile 14, using Relative Amplitude.

The anomalous values were corrected (Figure IV.9) and a new processing step was added to the flow for this purpose.

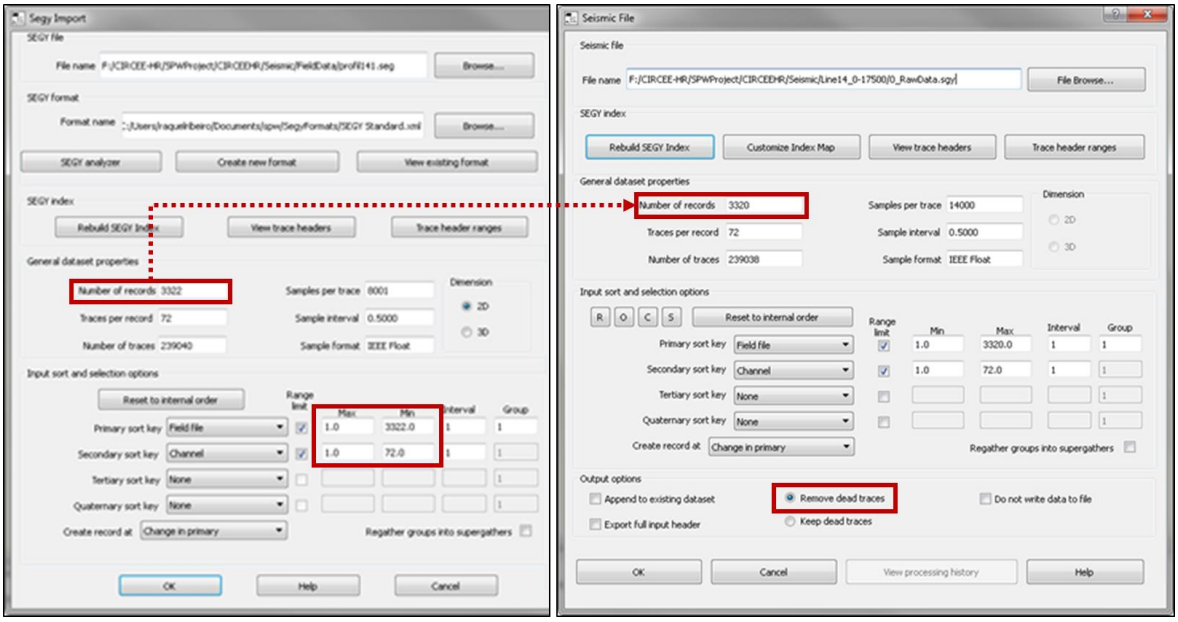

Figure IV.9 - SEG Y Import dialog (at the left) and Seismic File dialog (at the right). Correction of the anomalous values in the primary and secondary sort keys.

Clipping

A clipping step was used to remove the anomalous high-amplitude sample values from the input data and replace them with a threshold sample value. This was made in a way to guarantee that the largest positive and the largest negative sample amplitudes are acceptable.

Hatton et al. (1986) refer that very high amplitude reflections are generally clipped at a specific excursion of between 2 and 4 times the trace spacing, to prevent nearby adjacent traces being obscured or confused.

One simple and practical way to determine the range of the “normal” data amplitudes is moving the mouse over the seismic data and seeing which the common values are. The SPW software also allows visualizing a histogram that shows the amplitude distribution of the selected data traces (Figure IV.10).

The clipping tool was selected in the Amplitude Adjustment processing category, and the chosen input values were -20000 and +20000 (Figure IV.11).

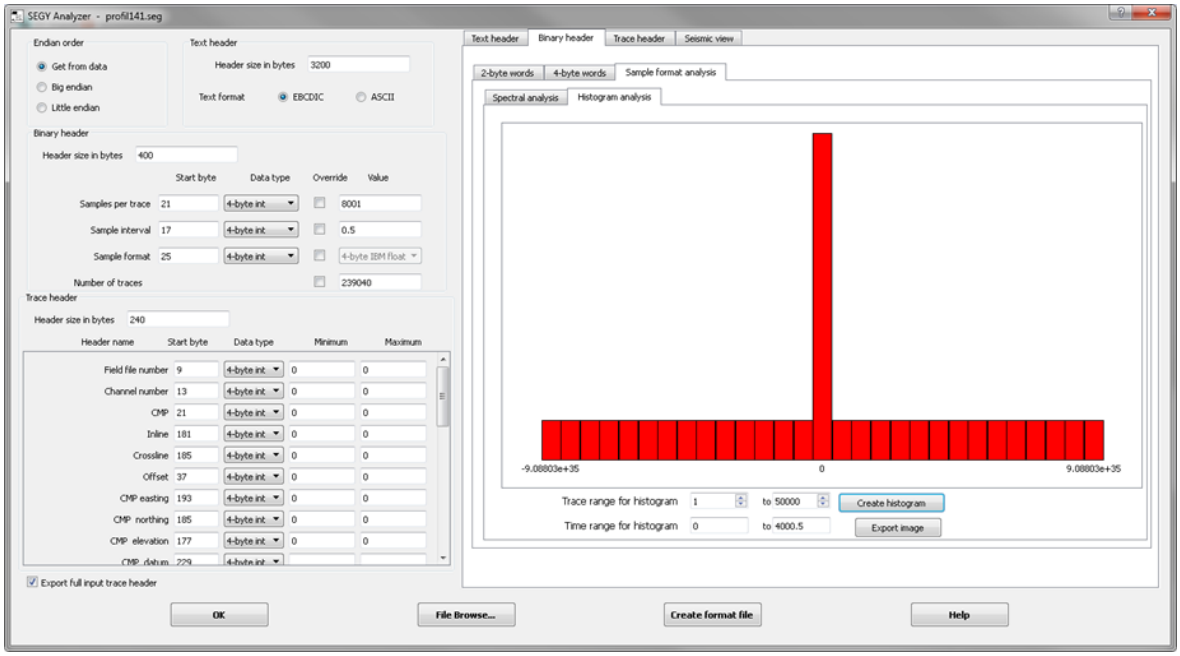

Figure IV.10 – Data amplitude histogram analysis display.

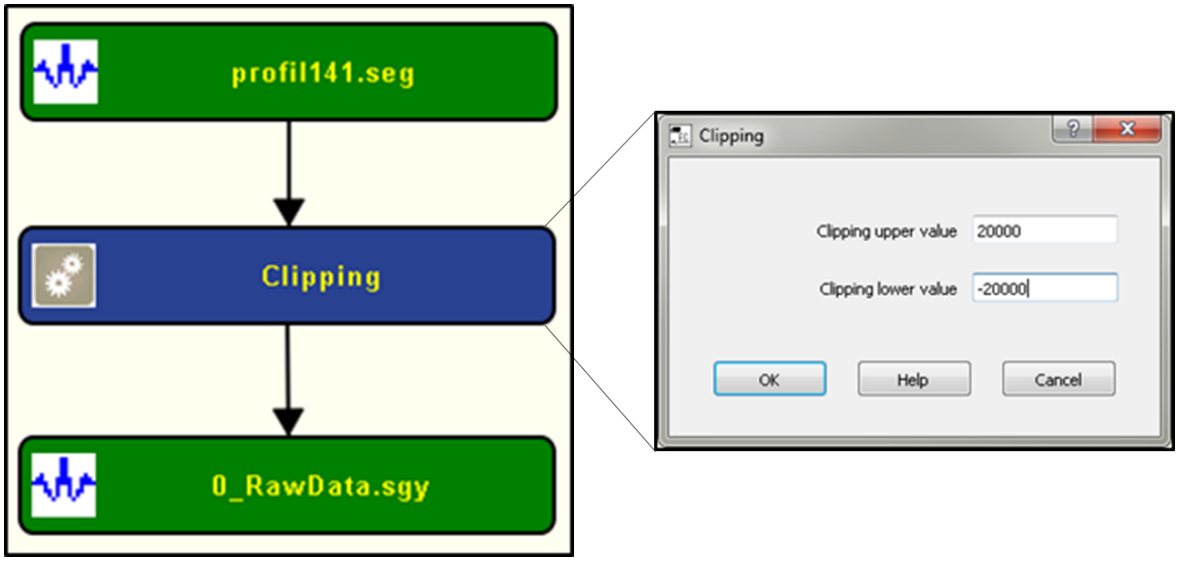

Figure IV.11 - Clipping tool in the flow 01 - Import.

Trace Sample Math

Despite the clipping, the amplitude reference value was still high. The Trace Sample Math was then used to apply a multiplying factor to the amplitude values, so that these do not cause any problems in the subsequent computational

operations (in this case, they were reduced by a factor of 100; Figure IV.12). The processing tool to perform this can be found in the Editing processing category.

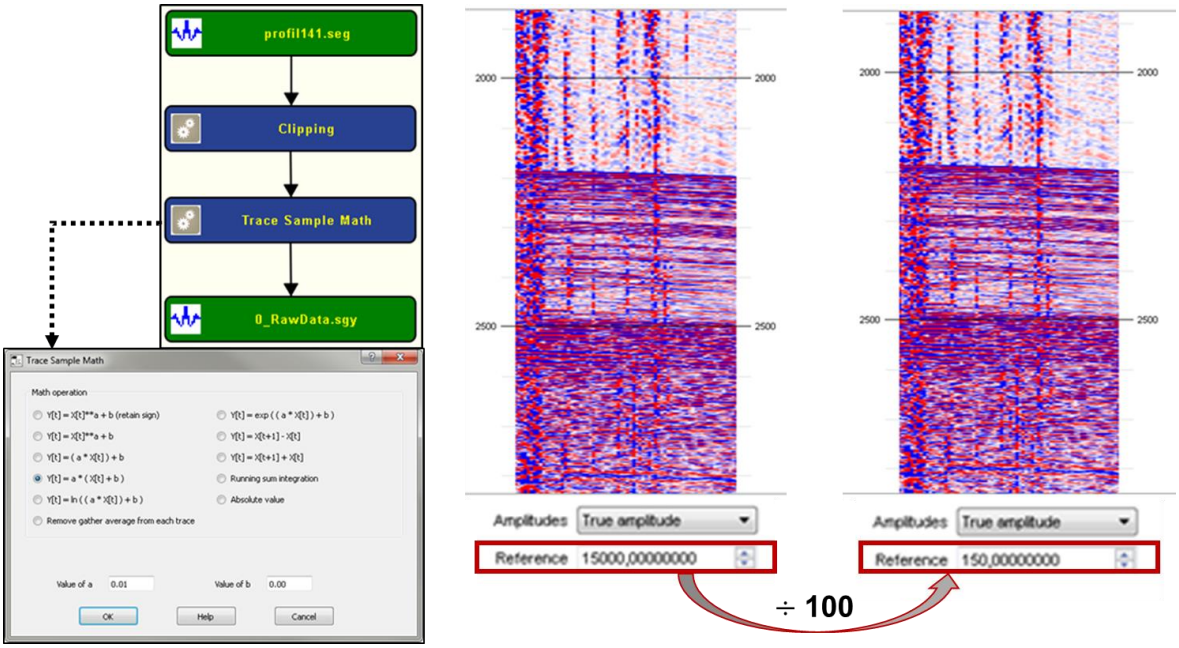

Figure IV.12 - Before and after the application of Trace Sample Math processing tool in the trace amplitude values.

The seismic profiles were “cut” onboard (specifically, the water column), due to limited storage available. This shift has to be corrected here in order to avoid future problems in the processing flows. This requires two processing tools: *Resample Seismic* and *Apply Static Shifts*.

Resample Seismic

The current trace length for the seismic profile is 4000 ms, but the true trace length is 7000 ms. To move the seismic data 3000 ms down it is necessary to create the missing time first. The *Resample Seismic* tool allows changing the start time and trace length of the data (Figure IV.13). Also, in this step, the sample interval can be changed, but that is not required in this specific case. This processing tool is also found in the *Editing* processing category.

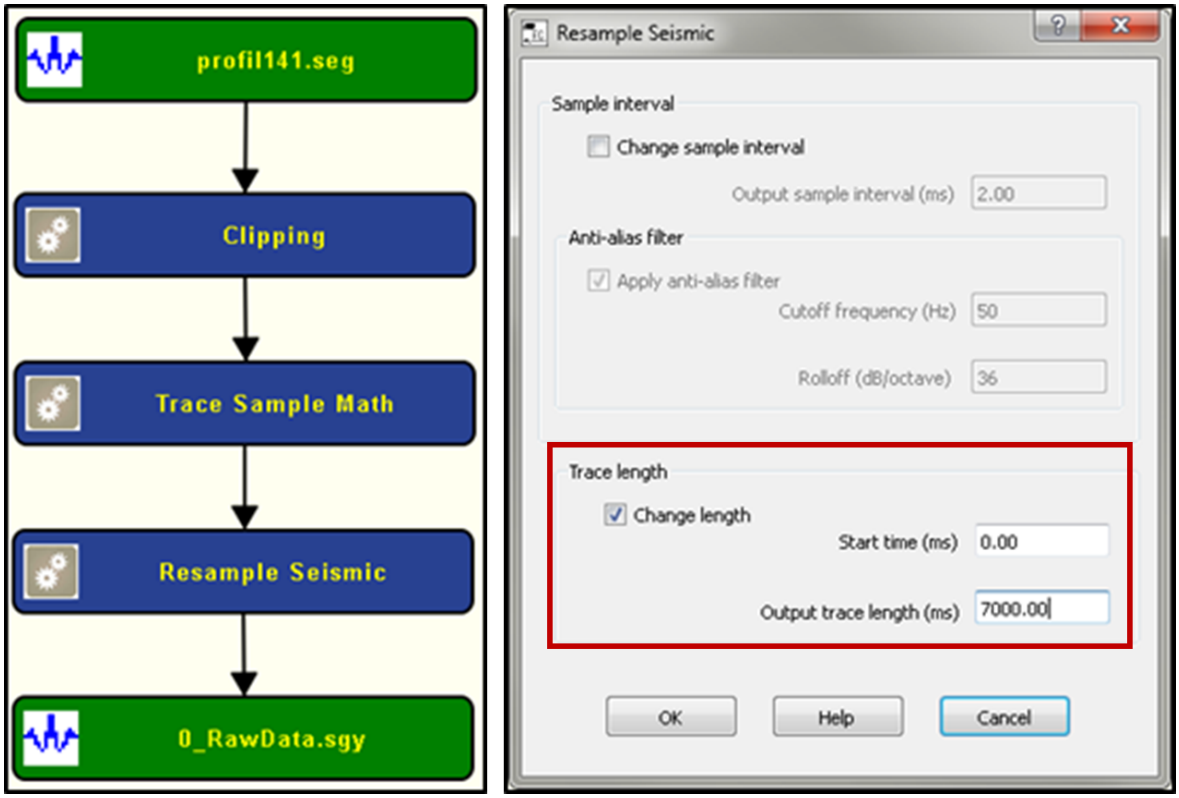

Figure IV.13 - The amplitude correction flow and the Resample Seismic dialog.

Apply Static Shifts

This processing step allowed applying a 3000 ms bulk shift to all the seismic data traces (Figure IV.14), so that the sea-bottom and subsurface reflections are now at the correct time.

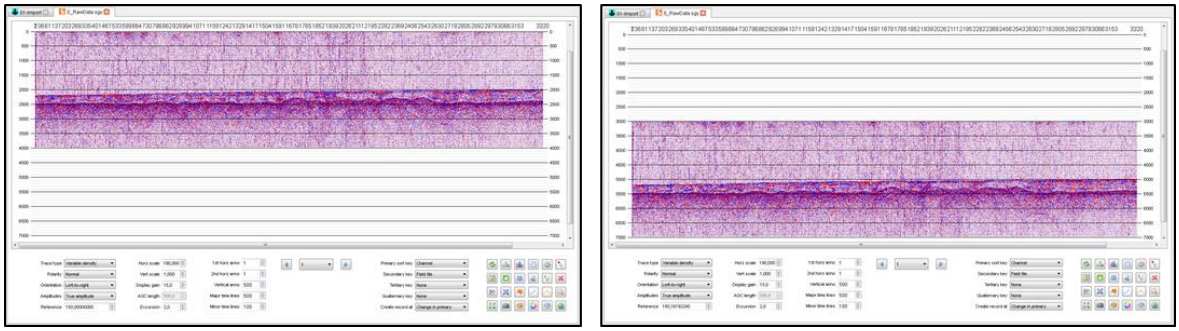

Figure IV.14 - Application of a 3000 ms bulk shift to all the seismic data traces.

IV.3.2 Quality control and frequency filtering tests

The quality control step is extremely important in the so-called “pre-processing” phase. It is also common to repeat this step at strategic points in the processing sequence, as the data response to many processes is not always uniform and predictable (Hatton et al., 1986).

All seismic traces from each channel were displayed as shot gathers (Figure IV.15). The main problems detected are consistently bad or reversed polarity channels, some coherent noise, potential multiples and interference over narrow frequency bands (Hatton et al., 1986).

After a cautious observation of all traces it was noted that the first nine traces showed some low frequency noise in the firsts channels, principally. In the last traces, a coherent noise also appears, but it should be highly reduced through stacking. Low frequency noise from channels 26 and 47 affect all traces (Figure IV.15).

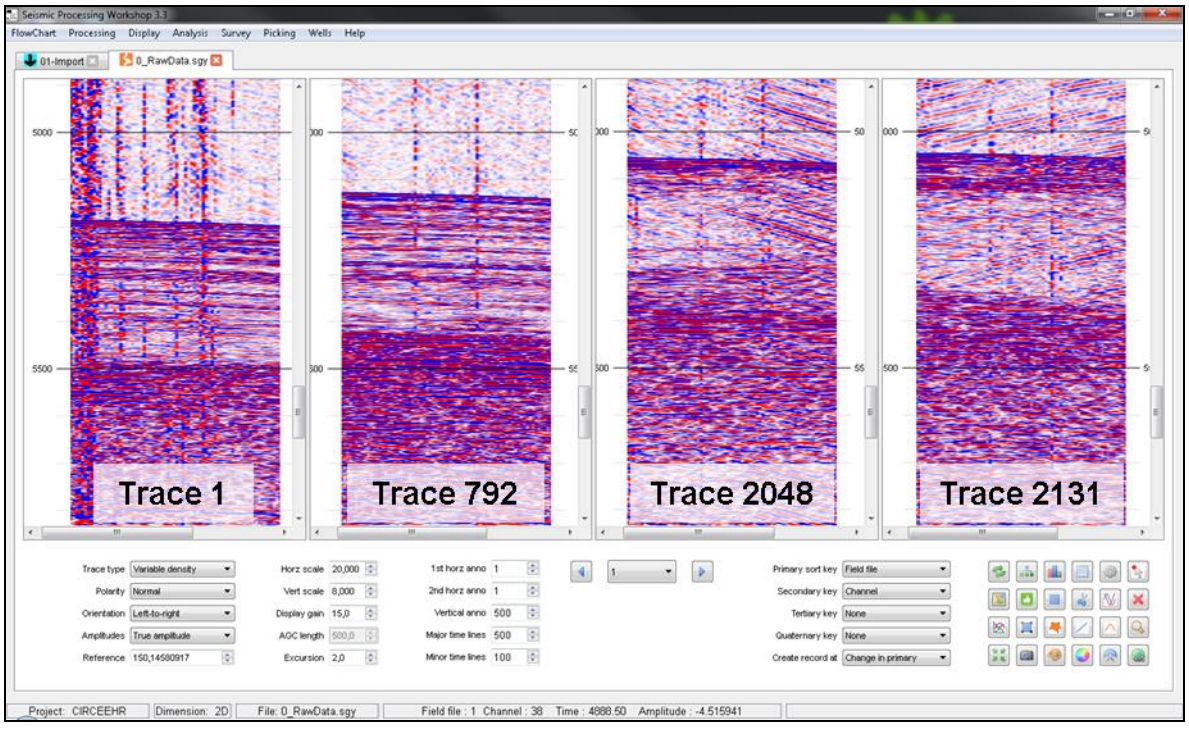

Figure IV.15 - Shot gathers of Field File Numbers 1, 792, 2048 and 2131, showing the different types of noise recorded in the data.

After observation trace by trace, the seismic file was displayed in the form of channel gathers, to better analyze the noisy channels previously identified. The first four channels show a little more noise than the other ones, except for the most critical: channels 26 and 47 (Figure IV.16)

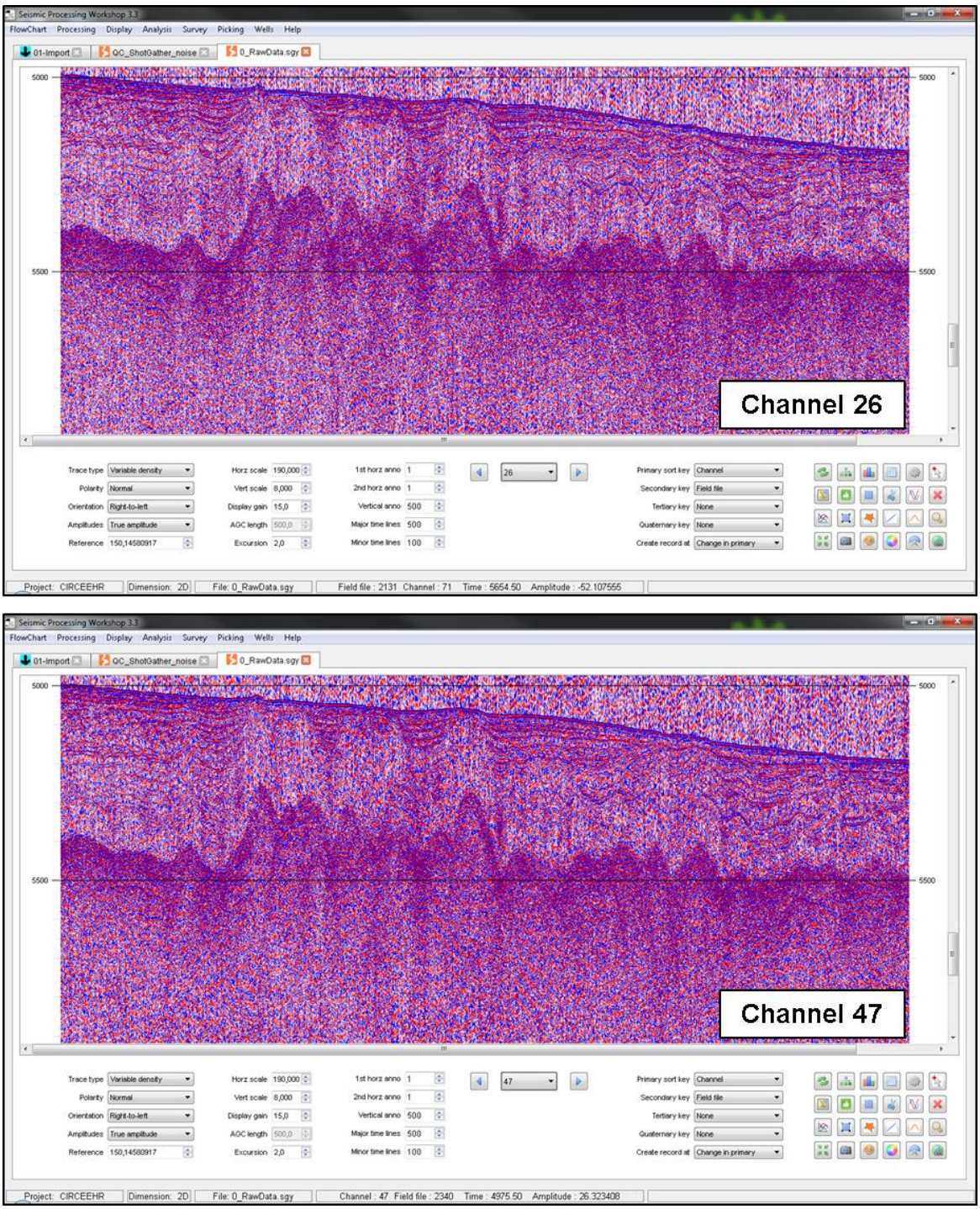

Figure IV.16 - Channel gathers from channels 26 and 47.

Frequency filtering tests

To maintain the frequency content of the seismic signal within a certain range of interest (to preserve the information desirable), frequency filters are applied to the seismic data. Band-pass filtering is commonly used, because a seismic trace typically contains both low-frequency noise, such as ground roll or other, and some high-frequency ambient noise (Yilmaz, 2001a).

A spectral analysis of the seismic data and noise is fundamental to find out which frequencies should be eliminated. First the noise frequency content was analyzed (Figure IV.17), and it was concluded that most of the noise frequency was lower than 50 Hz.

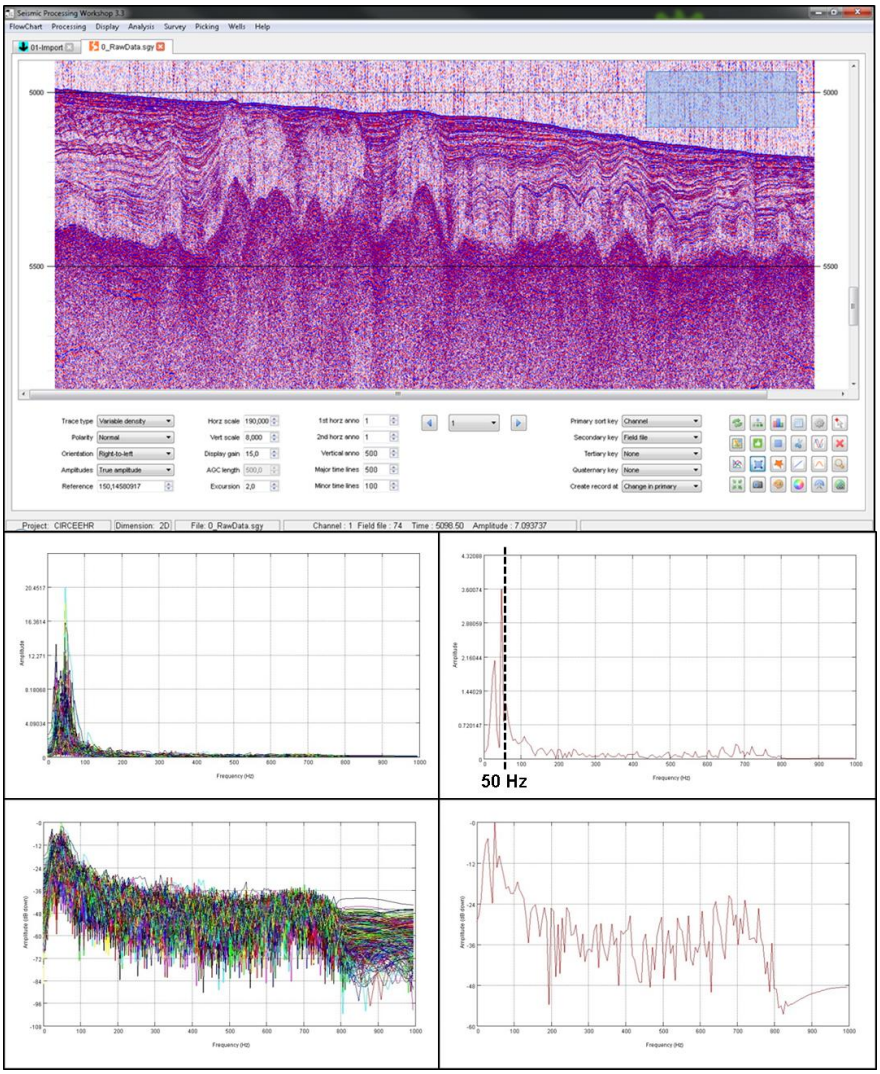

Figure IV.17 - Spectrum analysis of the noise frequency content (on top, amplitude spectrum; in normal scale; below, amplitude spectrum in a logarithmic scale - dB).

Then, using the same procedure, the data frequency was analyzed (Figure V.18). The amplitude spectrum generated shows that the most frequency content is below 350 Hz, although some information still remains up to 700 Hz.

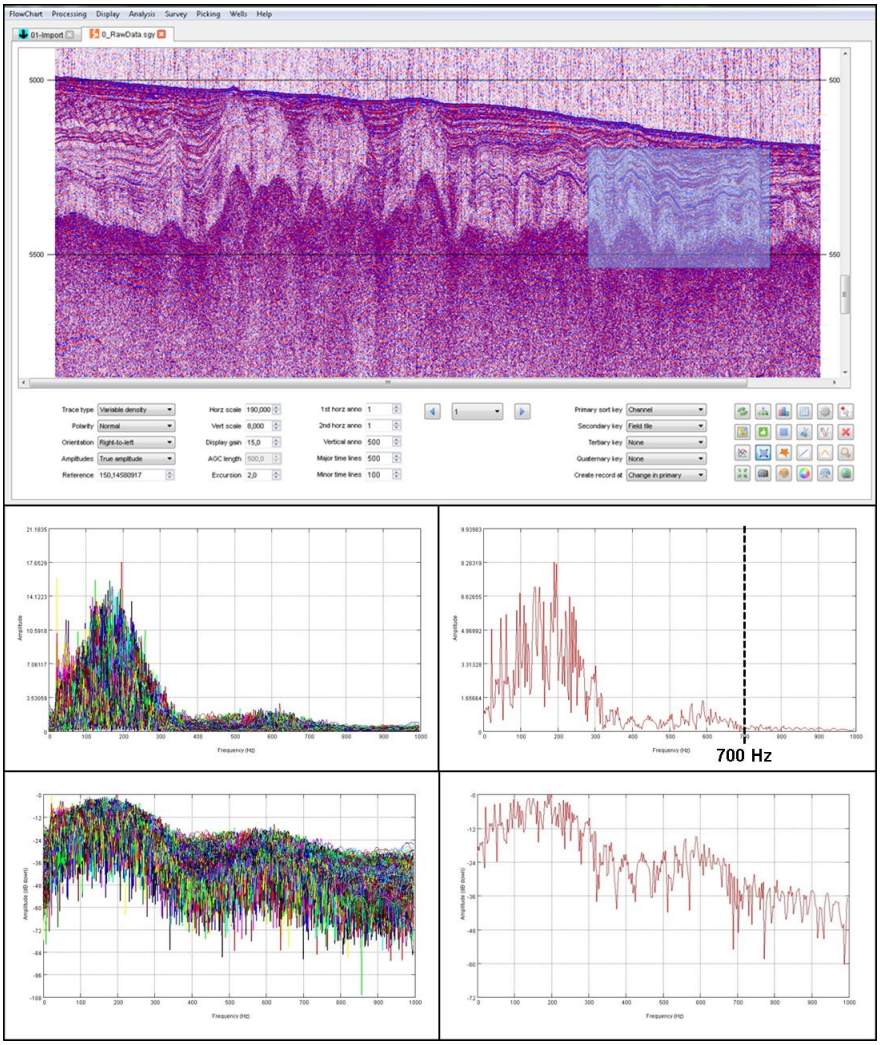

Figure IV.18 - Spectrum analysis of the data frequency content (on top, amplitude spectrum; in normal scale; below, amplitude spectrum in a logarithmic scale - dB).

Four low frequency filtering tests were made. In the first one was applied a 70 Hz Butterworth filter; these limits were chosen because they were used in onboard processing (Figure IV.19). The other high-cut chosen frequencies were 40 Hz (Figure IV.20), 50 Hz (Figure IV.21) and 60 Hz (Figure IV.22). Due to the high level of noise in channel 26 (and 47 too), this channel was chosen to perform a comparison between these four low-cut frequencies (Figure IV.23). The final decision was to cut all the low frequencies up to 50 Hz.

Also, three high-frequencies tests were made (Figure IV.24). In the onboard processing, the high-cut frequency used was 425 Hz; therefore so one of the tests used this value. High-cut frequencies as 300 Hz and 700 Hz were also tested. To preserve the maximum frequency content, considering that no significant high frequency noise was observed in the data, a high cut of 700 Hz was chosen.

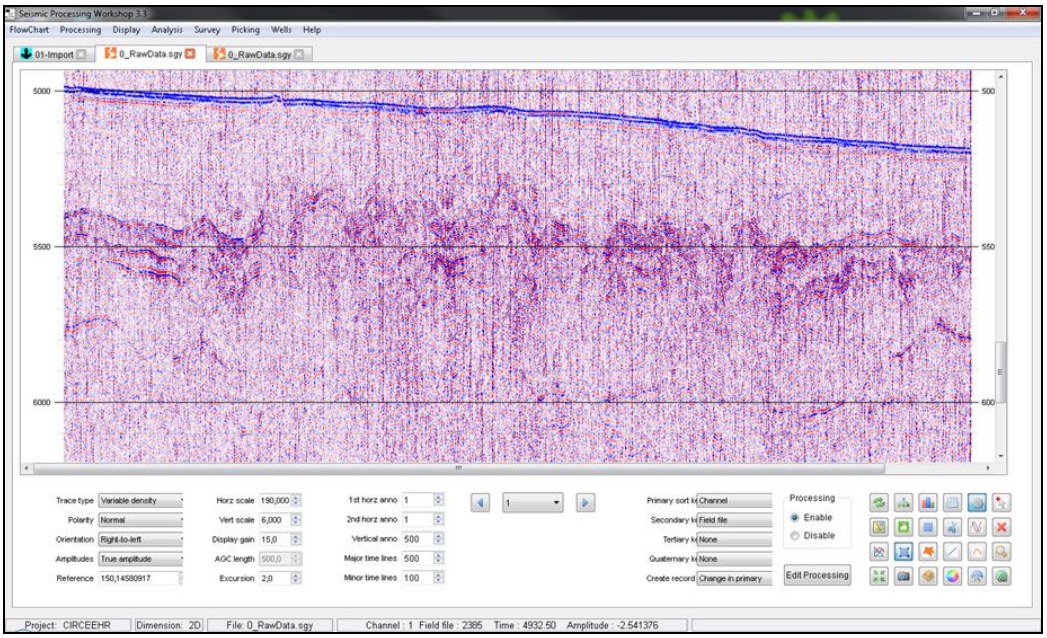

Figure IV.19 - First filtering test using 70 Hz as high-cut frequency.

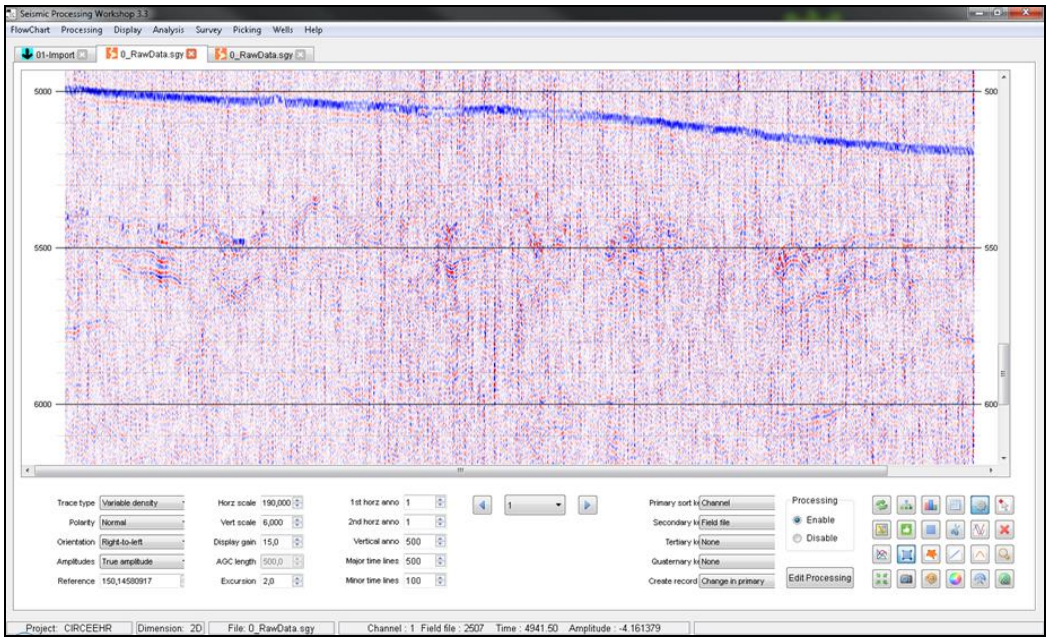

Figure IV.20 - Second filtering test using 40 Hz as high-cut frequency.

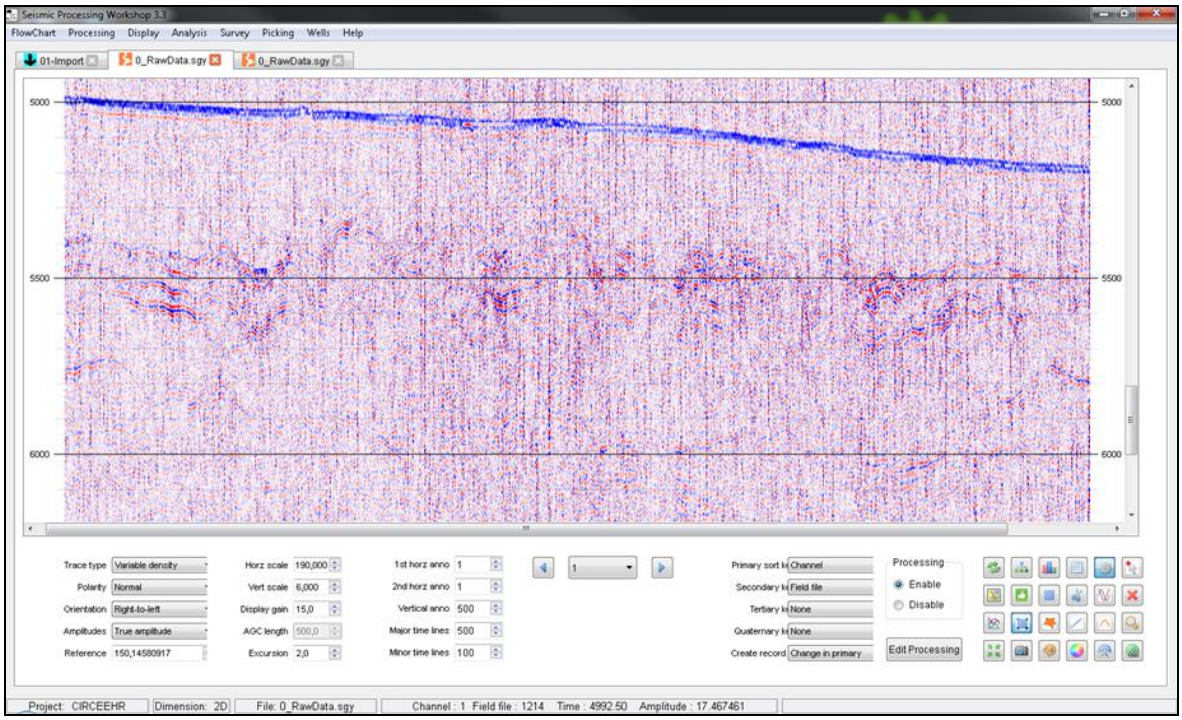

Figure IV.21 - Third filtering test using 50 Hz as high-cut frequency.

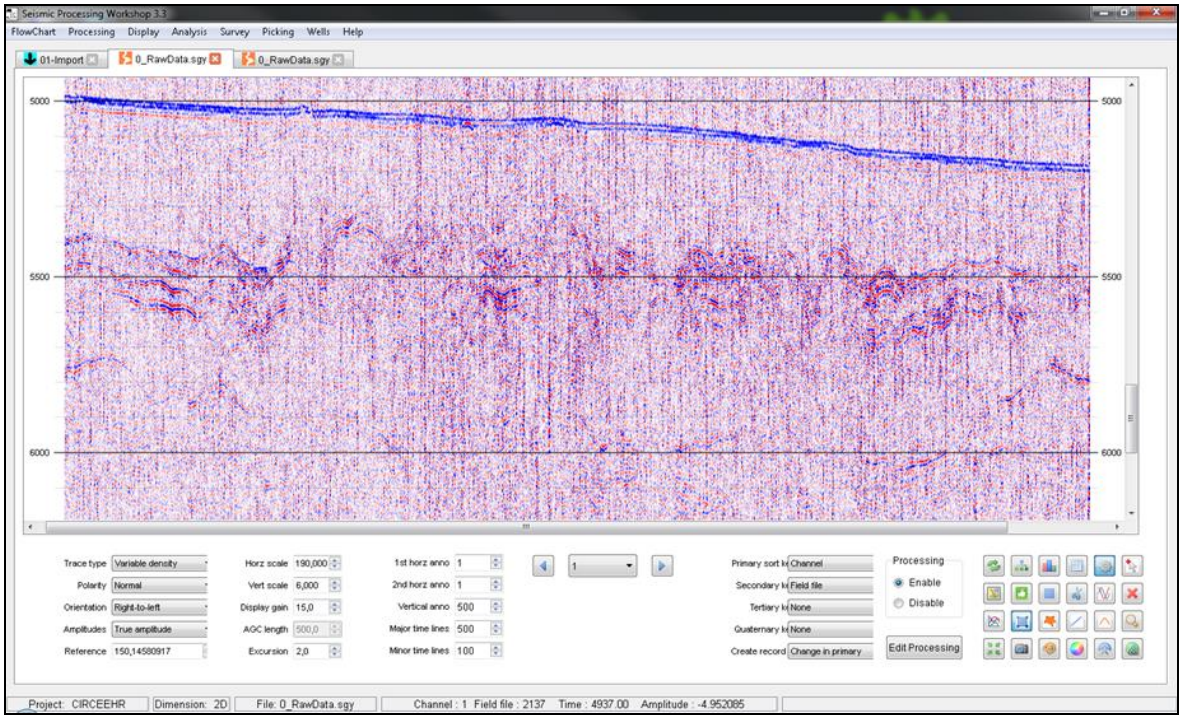

Figure IV.22 - Fourth filtering test using 60 Hz as high-cut frequency.

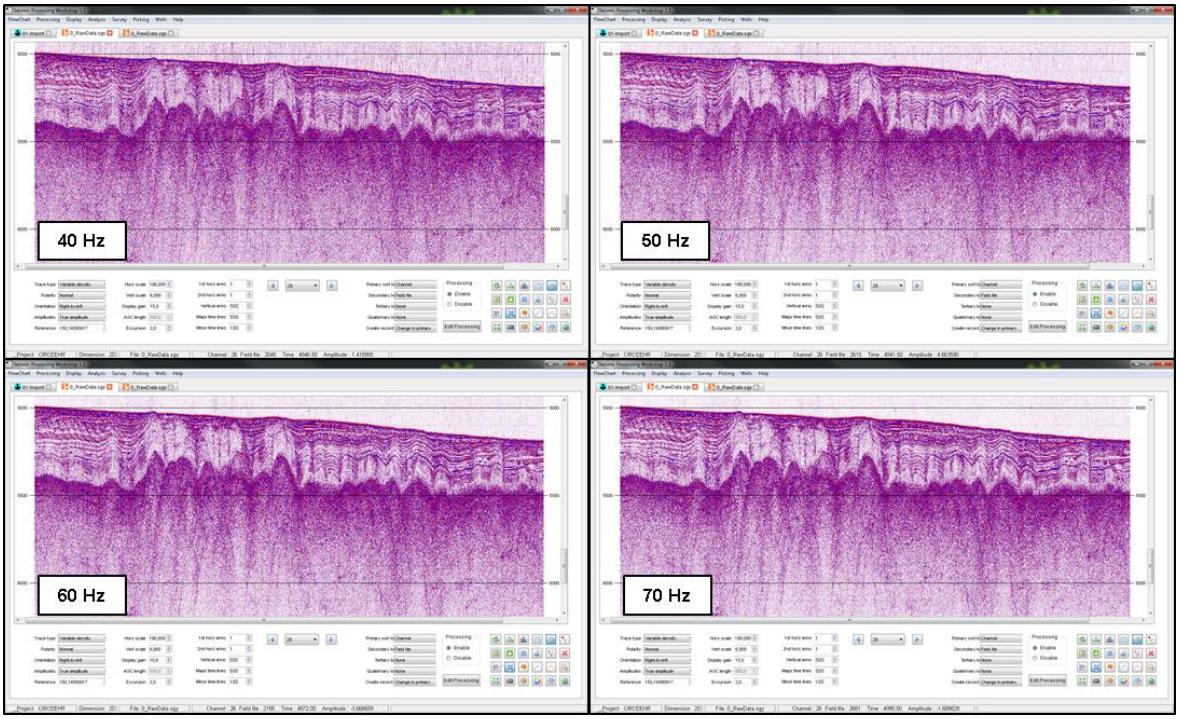

Figure IV.23 - Comparison of the testing four low-cut frequencies on channel 26.

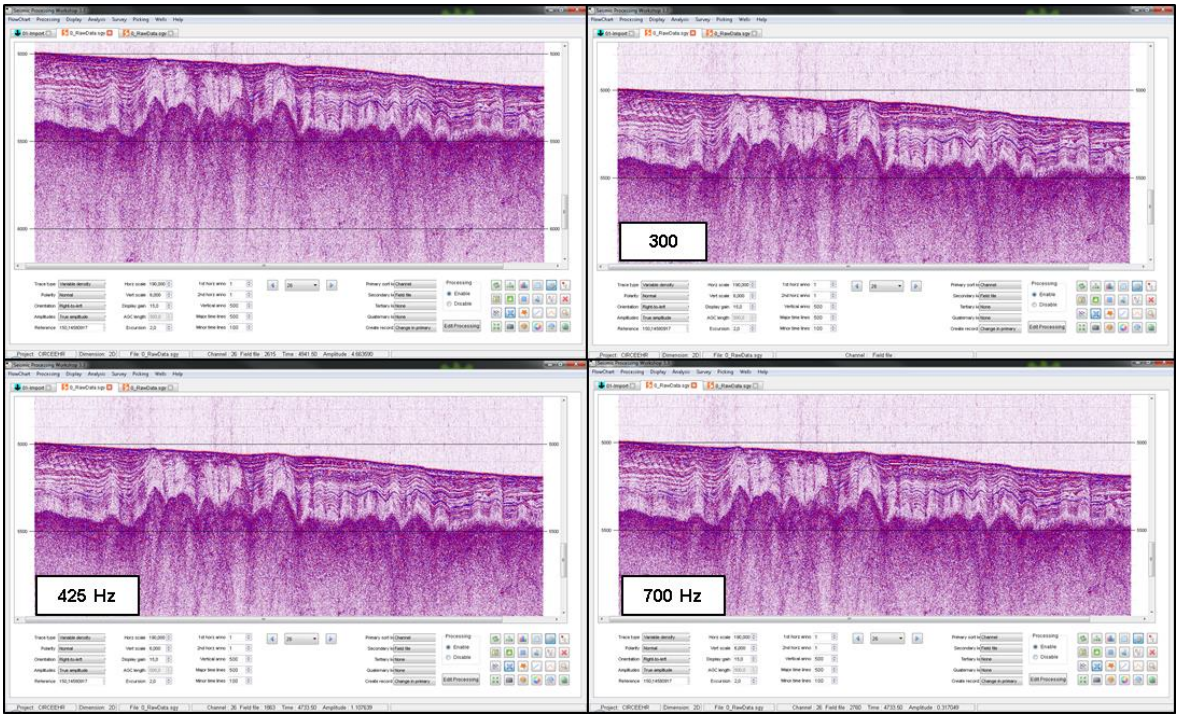

Figure IV.24 - Comparison of the testing three high-cut frequencies on channel 26 with no high frequency filtering.

IV.3.3 Flow 02 – Geometry

The processing flow 02 – Geometry (Figure IV.25) is composed by the following processes: *Simple Marine Geometry*, *Butterworth Filtering* and *Spherical Divergence*.

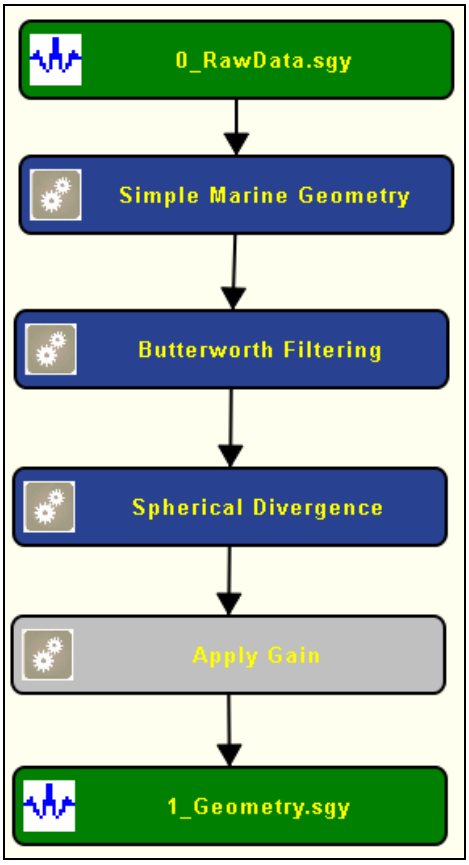

Figure IV.25 - Flow 02 - Geometry.

Simple Marine Geometry

The correct geometry assignment is crucial for a precise and accurate seismic processing. After this processing phase, the correct location of each shot, seismic receiver and CMP location are written into the headers of the seismic file. A mistake in this step has a large impact on subsequent processing stages (e.g. migration).

For the geometry assignment of marine seismic data it is necessary to define some seismic acquisition parameters (Figure IV.26), such as the shooting interval, the number of active channels, the channel interval and the source-receiver offset.

SPW works with its own integer units and not with real geometry parameters (metric system). Consequently, the first step of geometry assignment phase is to select a value which will correspond to an integer SPW unit; normally it should be a submultiple of both the seismic shooting interval and the channel spacing. The shooting interval from CIRCEE-HR dataset is approximately 16 meters (shot cadence about 6s), according to the report, and the channel spacing is 6.25 meters. The least common multiple in this case should be 3.125m (1 SPW = 3.125m), because it is half of channel spacing and a fifth of shooting interval (it will be considered 15.625m).

SPW software has a specific processing tool for marine acquisition (Figure IV.27). It is easy to fill (as long as everything is clearly defined before), and prevents possible user calculations errors.

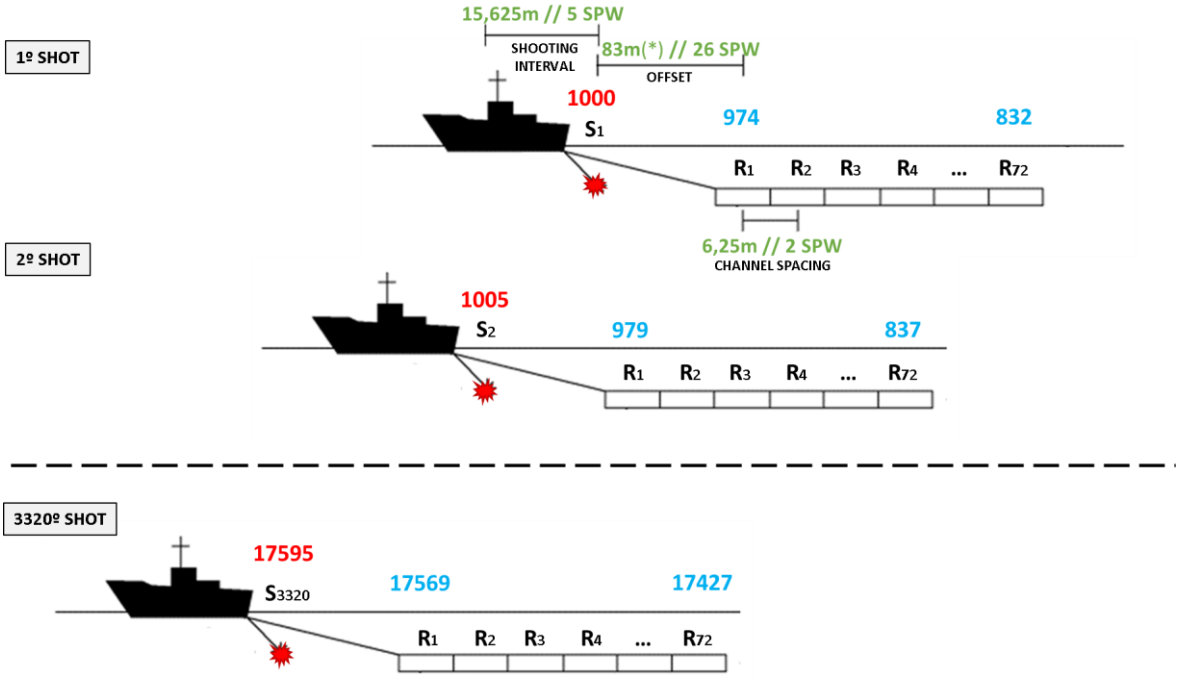

Figure IV.26 - Scheme of multichannel seismic acquisition geometry, adopted on the CIRCEE-HR scientific cruise, for line 14, in metric and SPW units. As 26 SPW units are equal to 81.25m the 1.75m difference will be added to the source coordinates or subtracted to the receivers' coordinates, to keep the shot-receiver offsets connect.

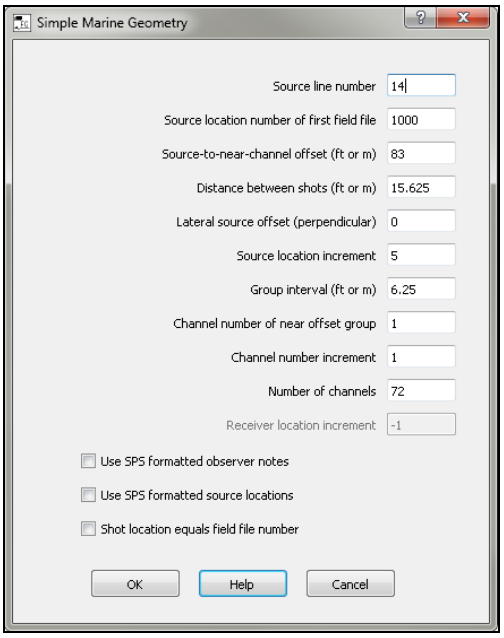

Figure IV.27 - Simple Marine Geometry processing card.

Butterworth Filtering

Following the results from the filtering tests described above, a 50-700 Hz Butterworth filter was applied, in order to preserve as much high frequency information as possible (Figure IV.28), considering that no high frequency noise was observed.

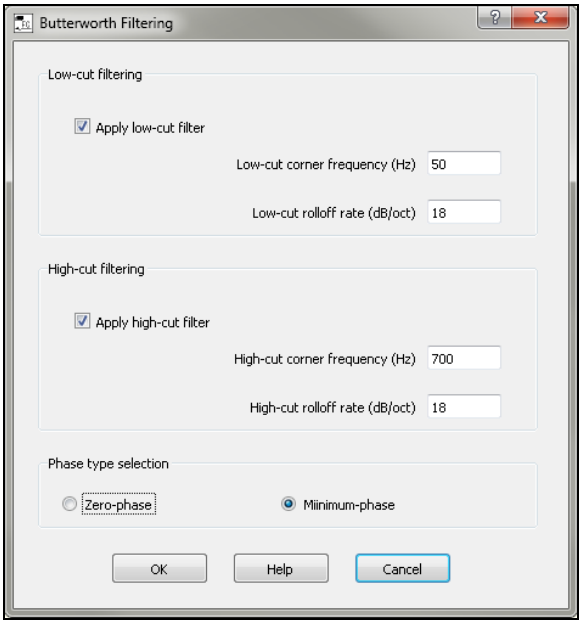

Figure IV.28 - Butterworth Filtering process card.

Spherical Divergence

There are many factors which affect the amplitude of the seismic signal as it propagates through the Earth. One of them is called spherical divergence. In a homogeneous medium, the wavefront from a point on the reflector will be spherical. As the wavefront expands, the energy of the disturbance is spread over a larger and larger area, so that the energy density of the seismic wave decreases with propagation distance (McQuillin *et al*., 1984; Figure IV.29).

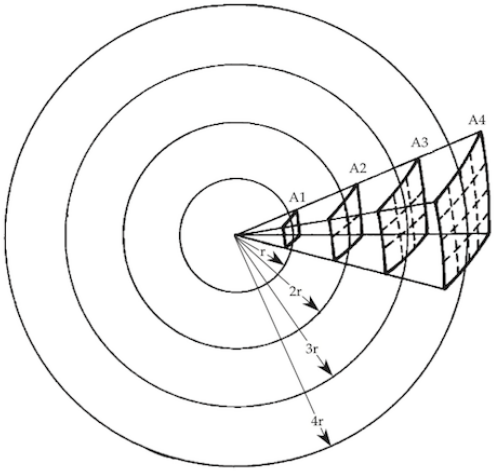

Figure IV.29 - Schematic representation of spherical divergence showing the spreading of the initial acoustic energy over an ever increasing wavefront surface with distance (http://theflavorful.com/classes/cooking-with-sound/sound-reference/).

The spherical divergence correction process increases the gain of the data using a spatially averaged velocity function with the time, compensating in this way the loss of amplitude of deeper reflections due to geometrical spreading over a larger area. This processing tool is found in the *Amplitude Adjustment* processing category; default parameters were applied (Figure IV.30).

Sometimes a gain function is also used to compensate for attenuation losses (increasing the amplitude content of the data in the deeper section). This processing step was not performed because the processing tool *Apply Gain* was not correctly working in this SPW version.

Figure IV.31 compares the seismic profile after running flow 01-Import and flow 02-Geometry, where the notorious difference is the low frequency noise decrease.

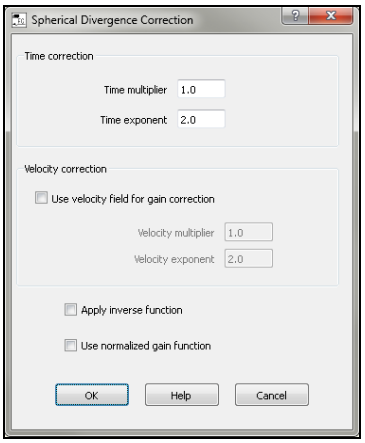

Figure IV.30 - Spherical Divergence Correction process card.

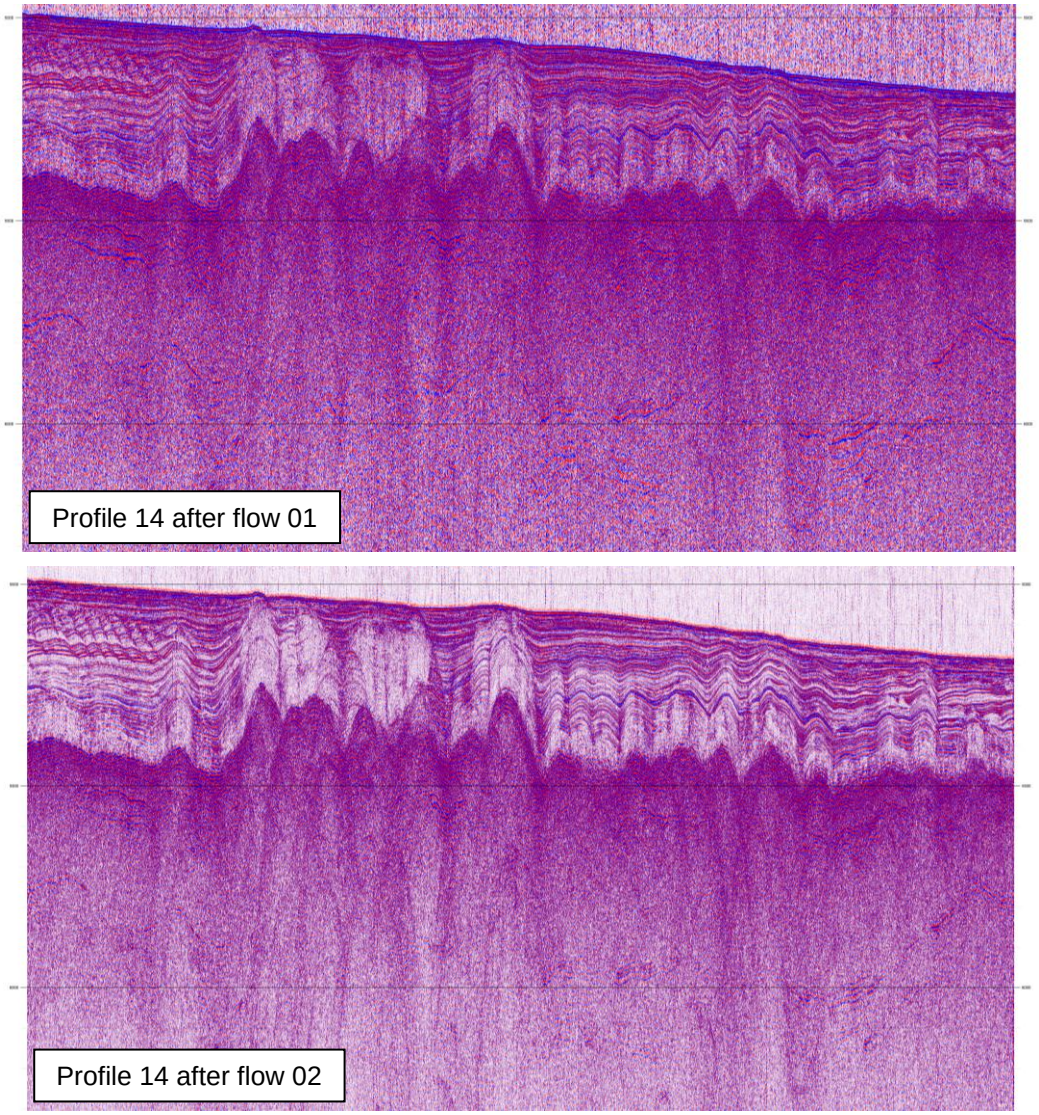

Figure IV.31 - Comparison between the output single channel seismic profiles after flow 01 - Import (above) and flow 02 - Geometry (bellow).

IV.3.4 Velocity Analysis

After the geometry definition, the filtering and the amplitude correction steps, a velocity analysis is performed, which will be used for the stack and migration algorithms.

To perform this processing step the Velocity Analysis Builder was opened on [Analysis] → [Velocity Analysis]. The input file was the seismic file with the geometry assignment. The analysis outputs chosen were Velocity semblance, CMP gather and velocity picks. The parametrization used can be seen on Figure IV.32.

Due to the short streamer (only 450 m of active sections) used in this multichannel seismic reflection survey, it was impossible to make a good velocity analysis (see Figure IV.33). That is why in the following steps (Normal moveout, stacking and migration) a constant velocity of 1540 m/s was used.

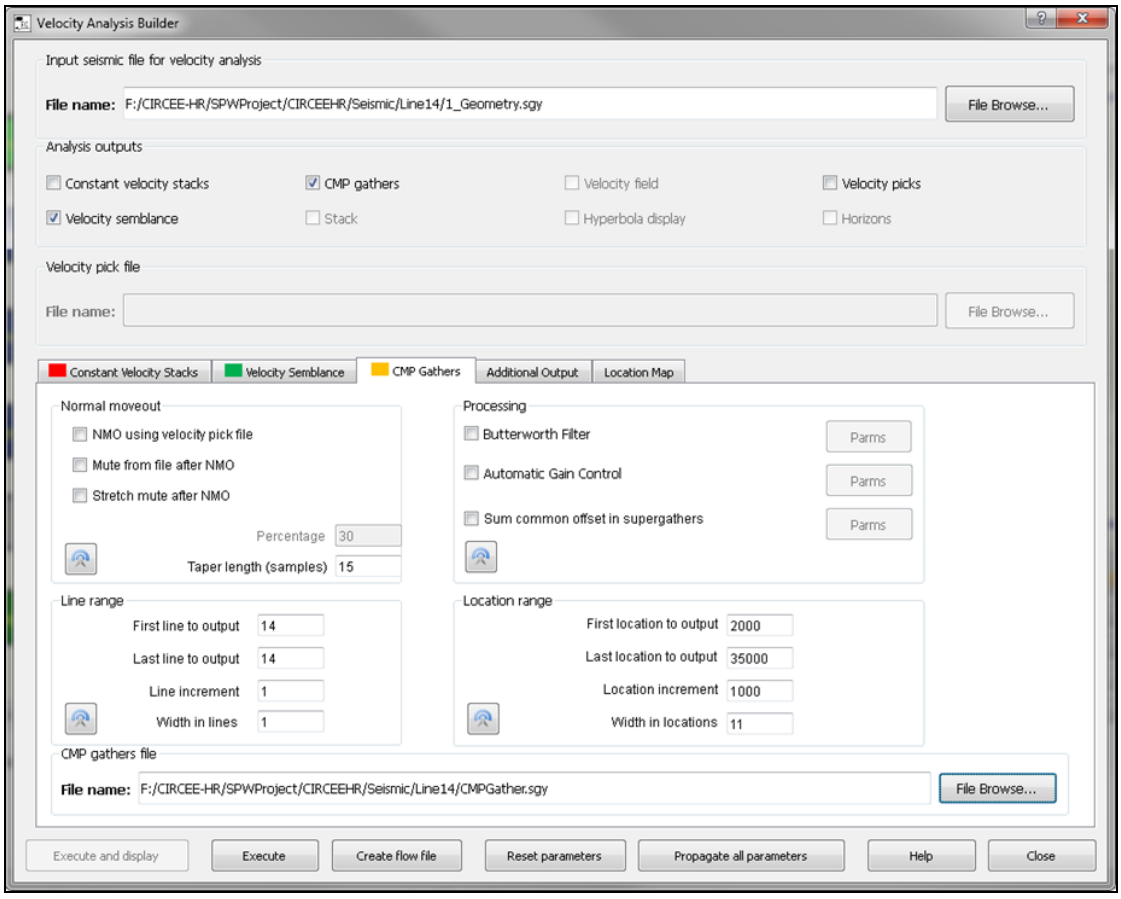

Figure IV.32 - Velocity Analysis Builder.

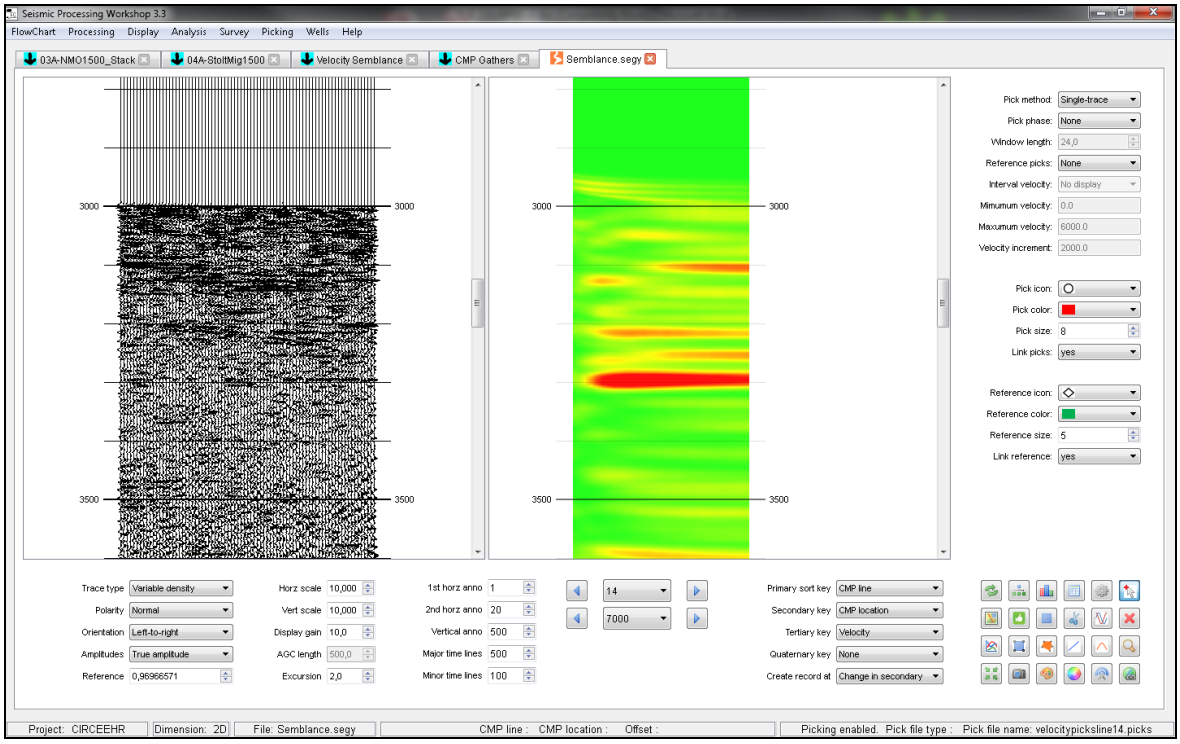

Figure IV.33 - Velocity Analysis display. In the left: the CMP. In the right: the velocity semblance, showing that the short offsets do not allow an adequate velocity analysis.

IV.3.5 Flow 03 – NMO_Stack

The processing flow 03 – NMO_Stack (Figure IV.34) is composed by the following processes: *Apply Normal Moveout* and *CMP Stack*.

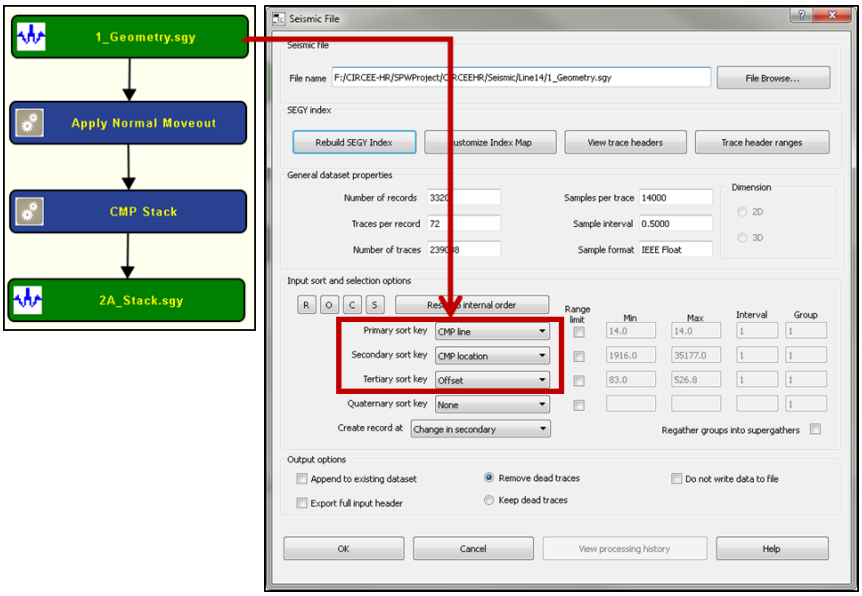

Figure IV.34 - On the left: flow 03 - NMO_Stack. On the right: CMP sorting of the input seismic file.

Before applying the NMO (normal moveout), the sort keys of the input file 1_Geometry must be: CMP line (primary key), CMP location (secondary key) and Offset (tertiary key; Figure IV.34). See Section III.2.3 for more detailed information on CMP sorting.

Apply Normal Moveout

This step corrects the time shift for each trace in a gather due to the offsets between receivers and sources on the arrival time corresponding to a same reflection point. Since the velocity analysis could not give good results due to the short offsets, as previously explained, a constant velocity of 1540 m/s was used for this correction. Several constant velocities were tested to improve the stack, but the final choice was the same adopted in onboard processing. The remaining parameters of the process card were filled with the default parameters, which are adequate in this case (Figure IV.35).

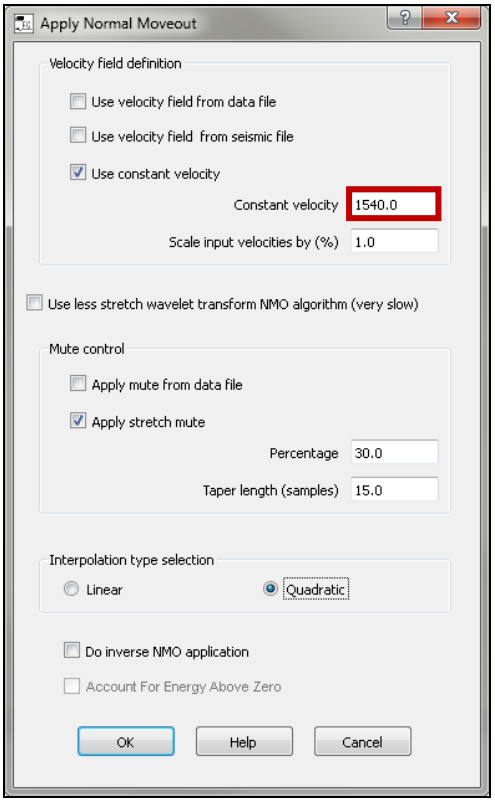

Figure IV.35 - Apply Normal Moveout process card.

CMP Stack

Common-midpoint stacking is the most important data-processing step in improving the imaging quality of the data. The traces within a common-midpoint gather are summed, along horizontal NMO-corrected seismic events, to yield a single stacked trace. The stacking of a seismic section severely increases the overall signal-to-noise ratio and attenuates most multiples and other coherent noise events that do not follow a hyperbolic path in the CMPs (Figure IV.36). The stack seismic section can be viewed in Figure IV.37.

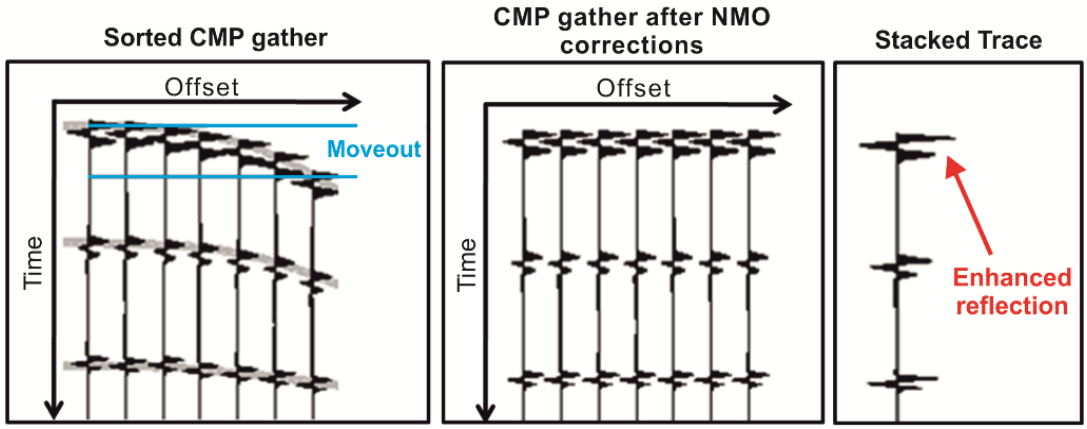

Figure IV.36 - CMP gathers before and after NMO correction, and stacking (modified from http://www.gsj.go.jp).

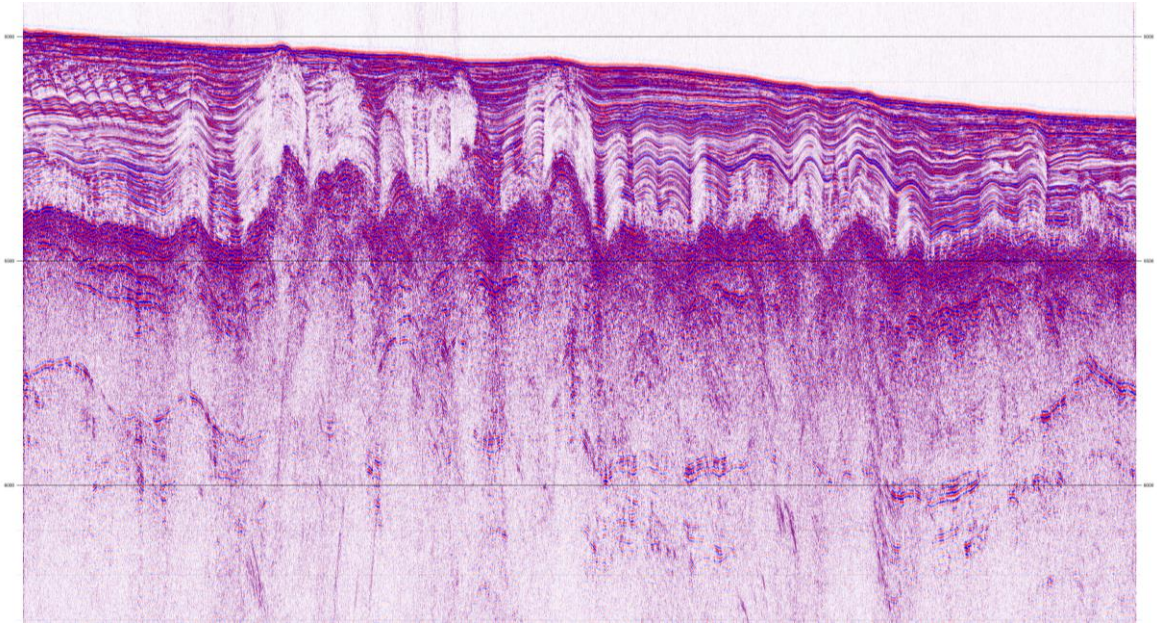

Figure IV.37 - Seismic profile 14 after normal move-out correction and stacking.

IV.3.6 Flow 04A – StoltMig1540

The processing flow **04A – StoltMig1500** (Figure IV.38) consists of the *Stolt (FK) Migration* process (using a constant velocity of 1540 m/s).

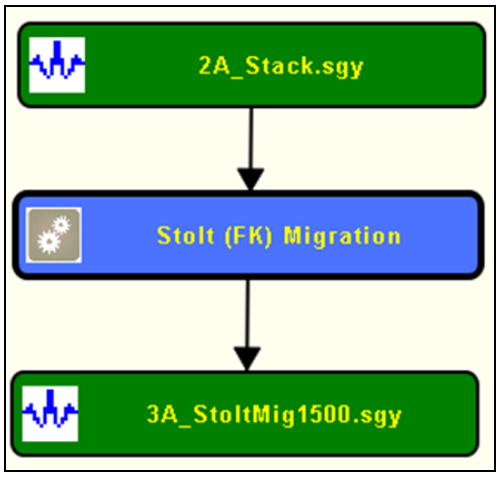

Figure IV.38 - Flow 04A - StoltMig1500.

Seismic Migration

Seismic migration is the procedure by which an image of the correctly positioned subsurface reflecting interfaces is obtained from a seismic time section (Figure IV.39). Correctly implemented, it is a transform from the unmigrated time domain to the migrated time or depth domain. The most important parameter in the migration process is to estimate reliable migration velocity model at all subsurface positions (Yilmaz, 2001a). When a seismic section is migrated, two undesirable effects may happen as a result of inadequate use of higher or lower seismic velocities: overmigration and undermigration, respectively.

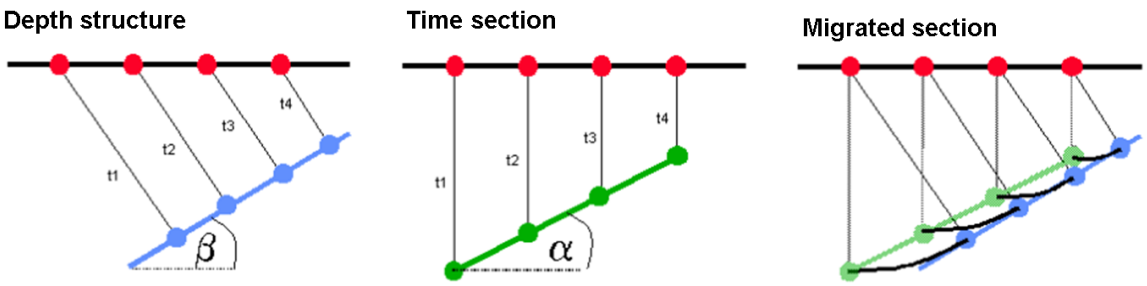

Figure IV.39 - Seismic time migration diagram. Blue: actual reflector. Green: apparent reflector; α: apparent dip. B: real dip (in www.xsgeo.com).

There are many types of migration algorithms available: (a) based on differential methods, (b) implemented in the FK domain (e.g. Stolt method), and (c) based on integral methods (e.g. Kirchhoff method). The migration algorithms can be applied before or after stack. Regardless of the migration algorithm used, the interpretability of a migrated section is dependent on the signal-to-noise ratio, on the velocities used in migration, and on the quality of the stacked section (when dealing with post-stack data; Yilmaz, 2001a).

The Stolt (FK) migration method was the first to be applied to the seismic line due to its faster algorithm for post-stack time migration. No velocity cards were linked. Instead, a 1540 m/s constant velocity was used, as it in the onboard processing (Figure IV.40). The final section can be seen in Figure IV.41.

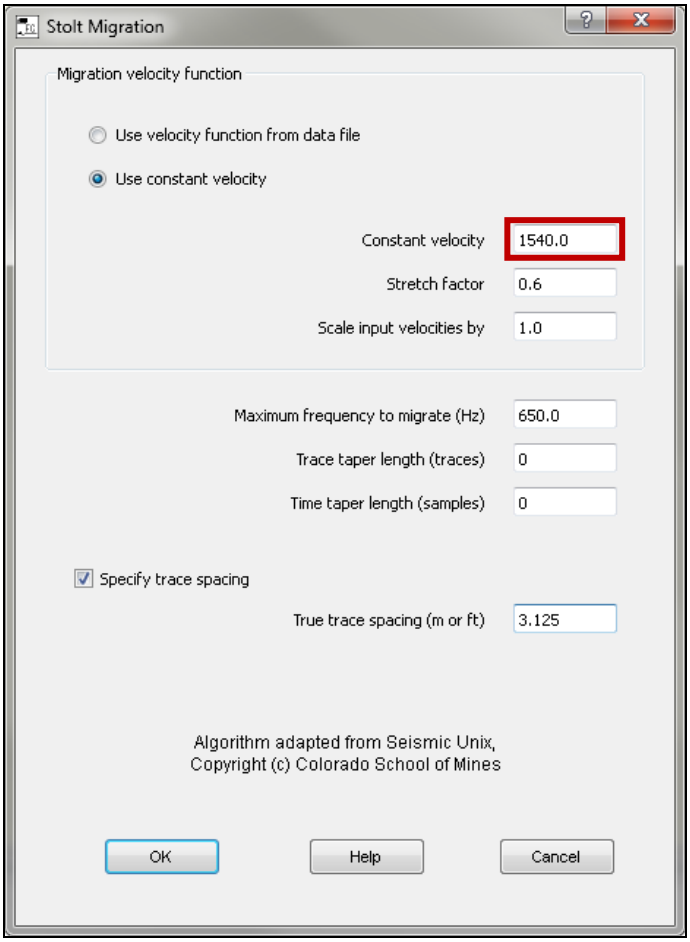

Figure IV.40 - Stolt (FK) Migration process card.

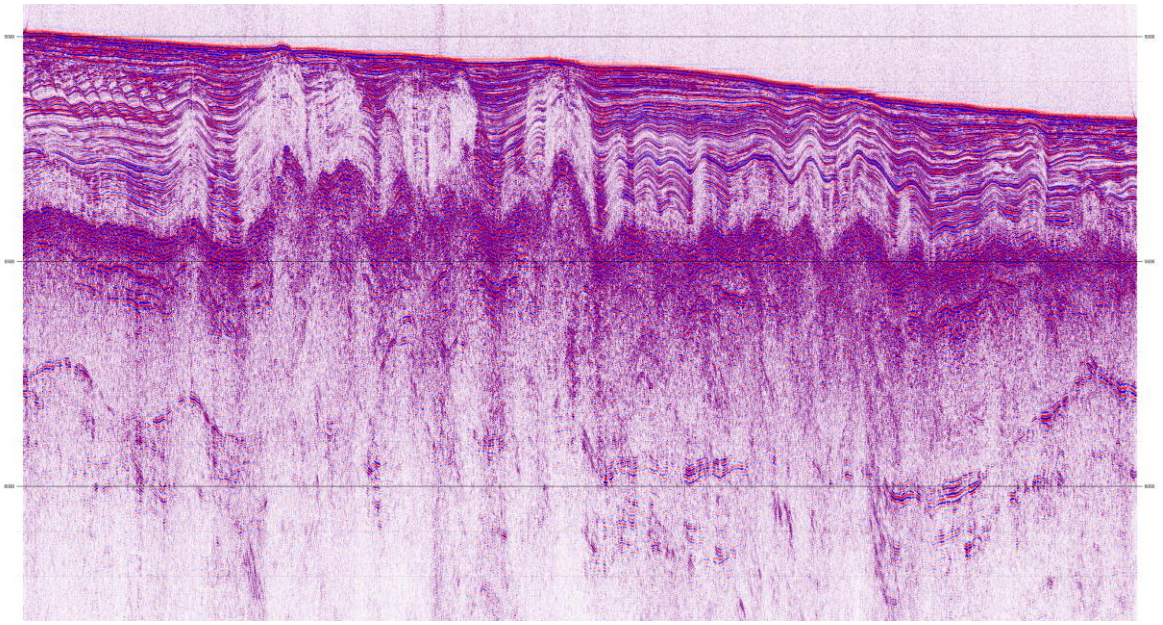

Figure IV.41 - Seismic line after Stolt (FK) migration.

IV.3.7 Flow 05A – PreStackKirchhoffMig1540

The pre-stack migration has the same principles as a post-stack migration but handles correctly the reflectors inclination from the beginning, instead of trying to correct for it after stack. Here, the migration algorithm is applied in each CMP gather and not in just each CMP location. It is therefore more time and computational consumer processing, but it allows, in most of the cases, better results, particularly for the deeper positions of the seismic sections in cases of very complex geology.

Kirchhoff's Prestack Time Migration was tested on one of the lines, to see if any improvement could be obtained (Figure IV.42). However, as expected, due to the lack of a good velocity model from the velocity analysis step (short length streamer to the massive water column and complex geology), no improvement could be obtained, as no reliable velocities could be assigned. The final section pre-stack migrated section can be seen in Figure IV.43.

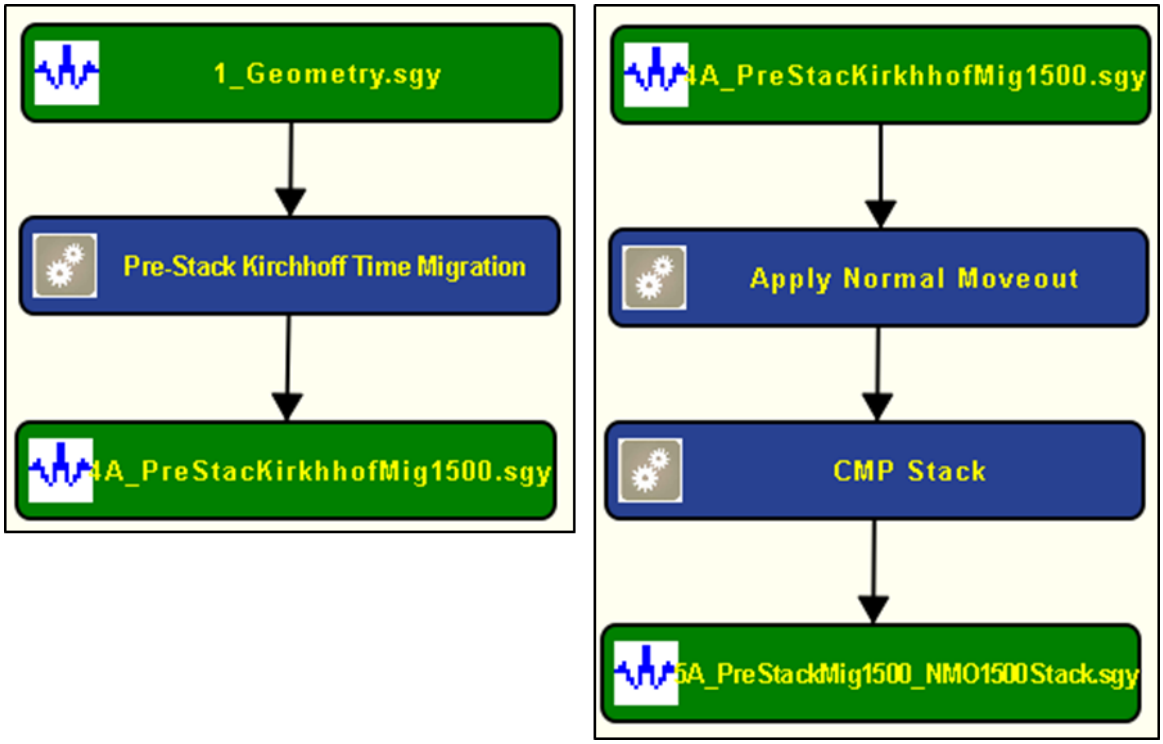

Figure IV.42 - Flow 05A - PreStackKirchhoffMig1500.

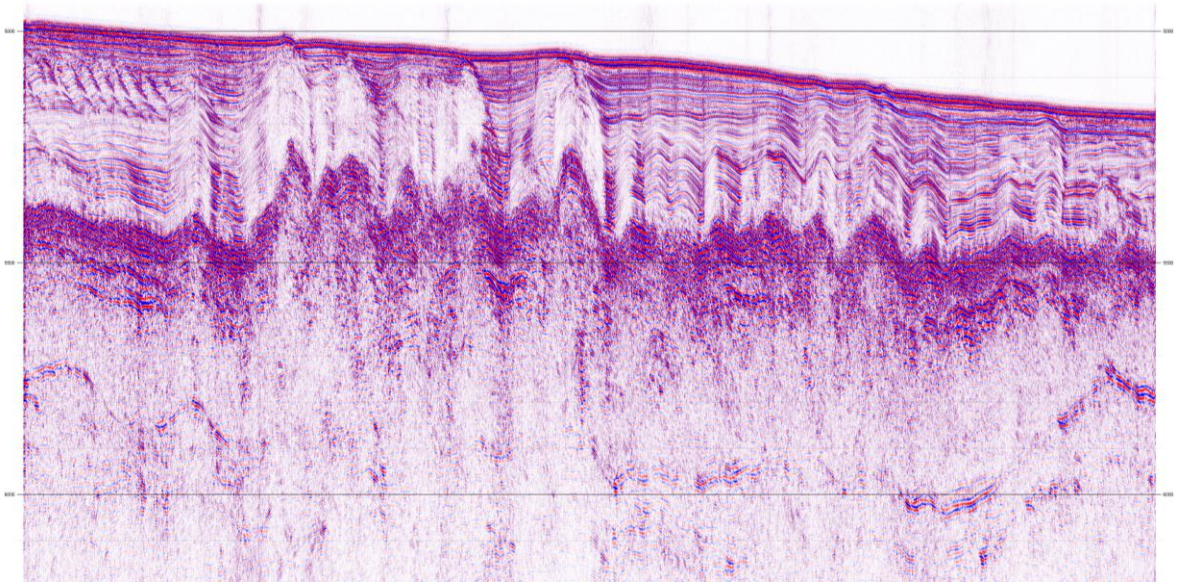

Figure IV.43 - PreStack Kirchhoff Time Migration seismic section (with a constant velocity of 1540 m/s).

IV.4 Comparison with onboard processing

The re-processing clearly improved the imaging of deeper horizons, which was one of the main aims in this work, since the upper part of the seismic sections was already well imaged. This was achieved largely because of the larger filter used (preserved frequencies between 50 Hz to 700 Hz. A comparison between on board processing profile and re-processing profile after migration can be viewed in Figure IV.44.

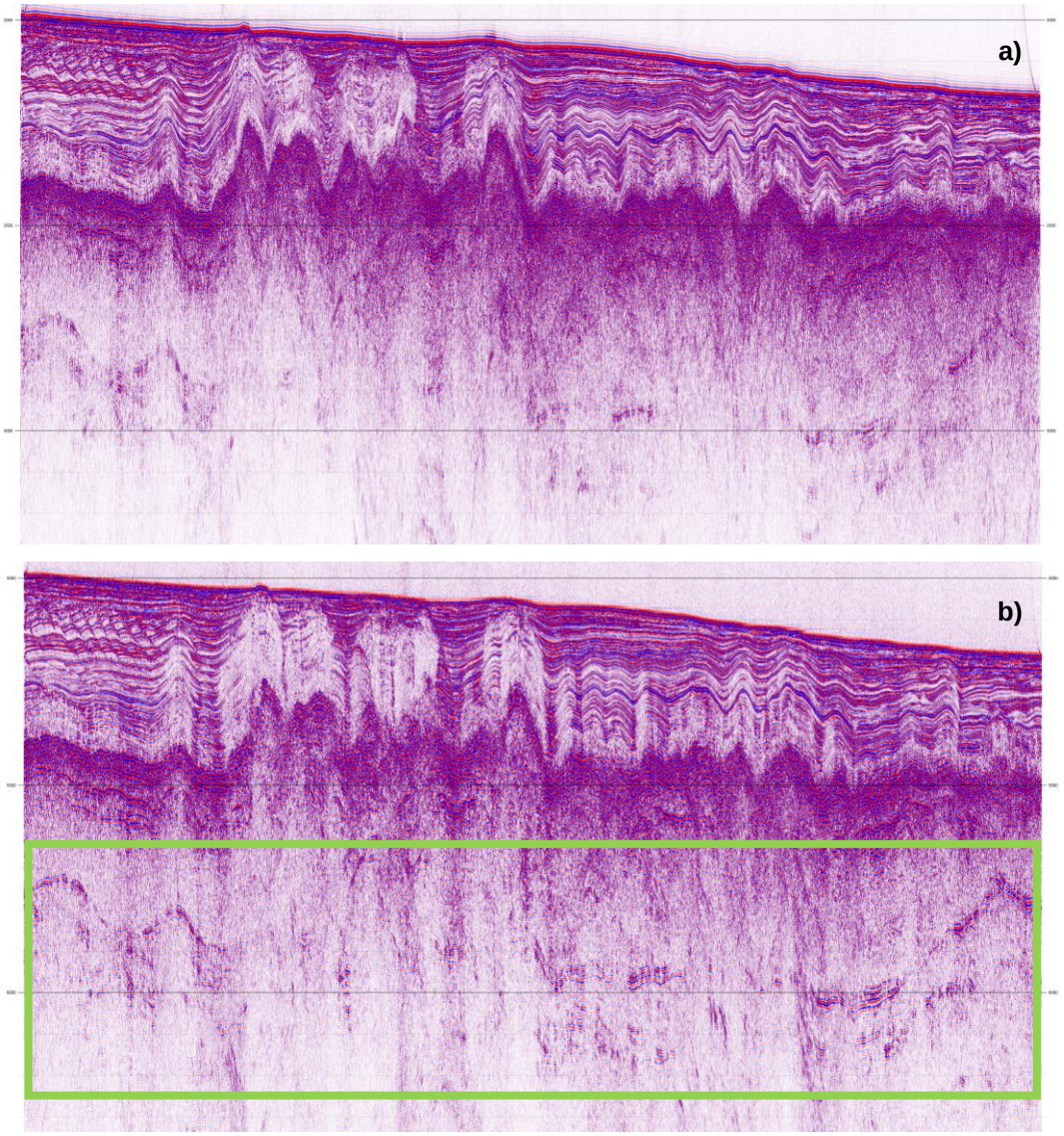

Figure IV.44 - Comparison between on-board processing profile (a) and re-processing profile (b), after Stolt migration. The light green rectangle highlights the deepest part of the seismic section where reflectors are better imaged than in Figure IV.43 a). These figures are shown in more detail in Figures IV.44 and IV.45.

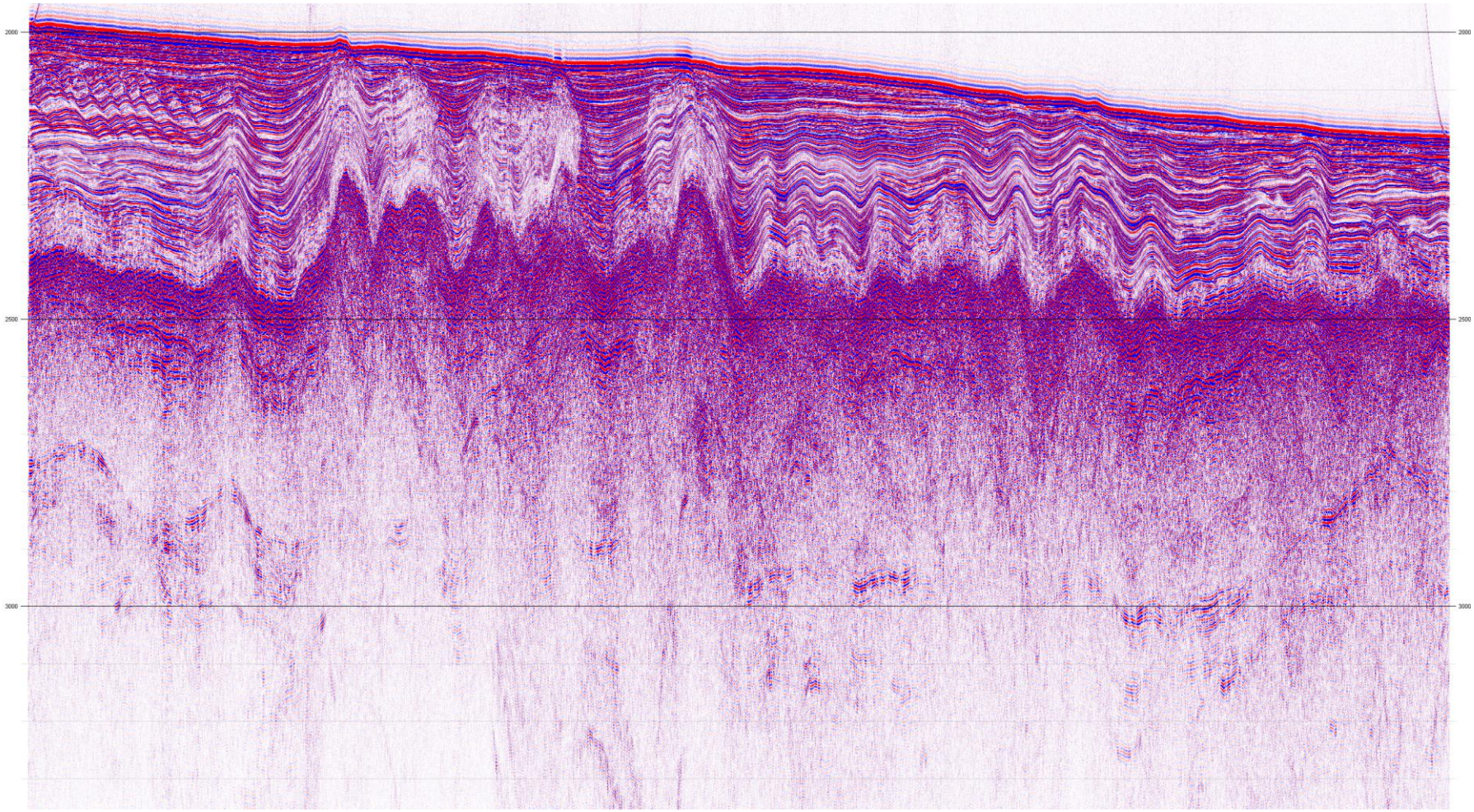

Figure IV.45 - On-board processing profile 14 after Stolt migration (detailed seismic section from Figure IV.43a).

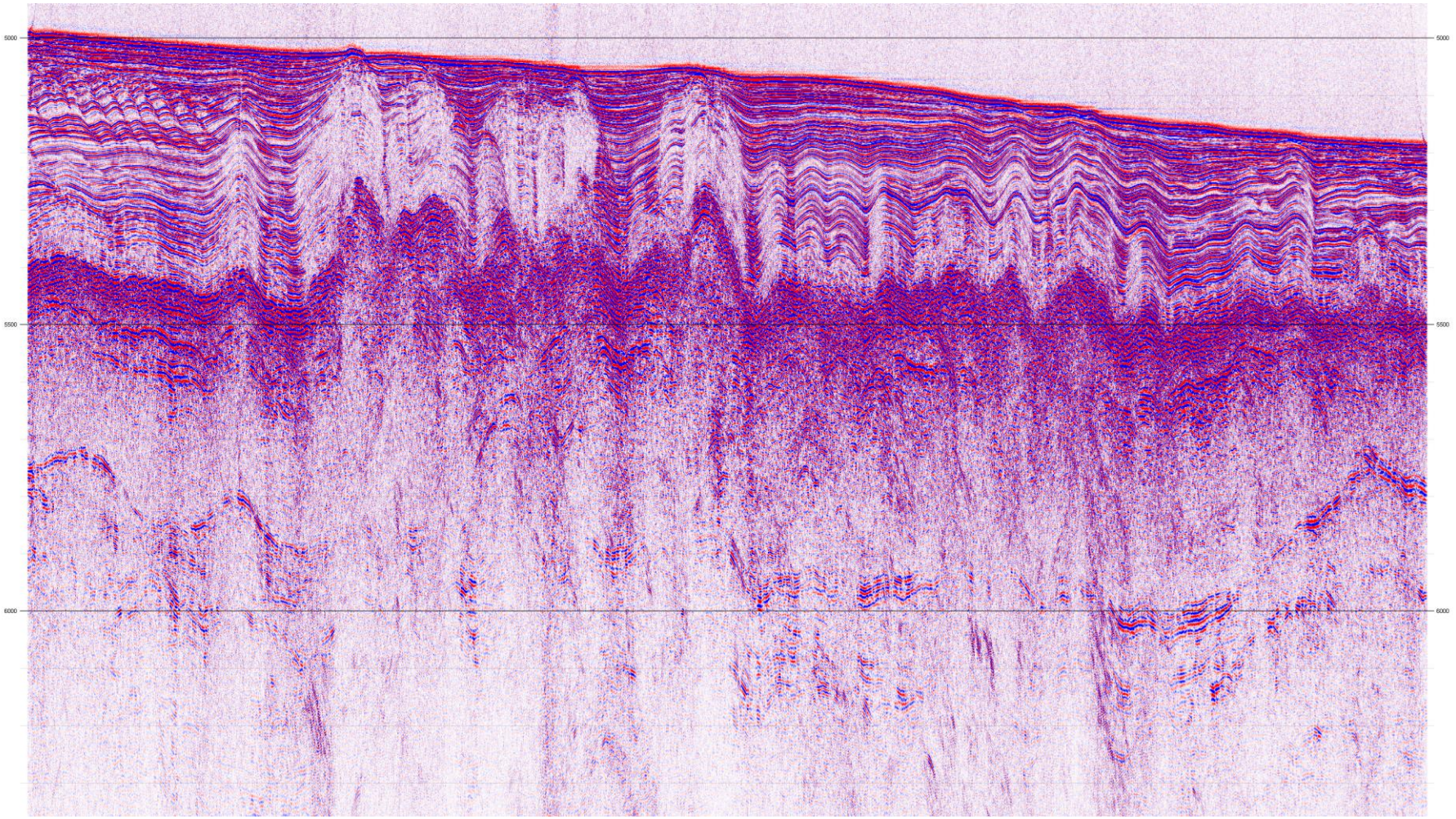

Figure IV.46 – Re-processing profile 14 after Stolt migration (detailed seismic section from Figure IV.43b).

Chapter V. Migrating Sediment Waves

Wynn et al. (2000c) defined sediment waves as a large-scale, undulating, depositional bedforms generated beneath a current flowing at, or close to, the seafloor.

Sediment waves occur in a variety of environments and water depths, and a display a wide range of morphologies, dimensions and sediment types (Wynn et al., 2000c). Deep-water sediment waves have been studied by marine geologists for almost 60 years; however, their formation mechanisms still are not fully understood. Despite this, in general, it is accepted that it always involves flows at or close to the sea floor (Wynn and Stow, 2002).

V.1 Global significance

Sediment waves have been observed in a wide variety of sedimentary and tectonic setting all over the world. In this chapter we present several examples such sedimentary structures. Damuth (1979), Reeder *et al*. (2010), Gong *et al*. (2011) and Li *et al.* (2013) reported the existence of several fields of sediment waves in the South China Sea, whose formation mechanisms and characteristics are clearly distinct. Previously, Karl *et al.* (1986) speculated that internal wave currents were the responsible formation mechanism for the Navarinsky Canyon sand waves. Recently, Droghei *et al.* (2016) proposed internal solitary waves as the formation mechanism of the sediment waves in the Messina Strait. Migeon *et al.* (2000) reported and compared the evolution of two fields of sediment waves (superficial and fossil) on the Var deep-sea fan, Ligurian Sea.

South China Sea

Damuth (1979) discovered a large field of migrating sediment waves on the gently dipping seaward wall of the Manila Trench, northern South China Basin (Figure V.1). Their wavelengths range from 200 m to 5 km, and their amplitudes range from 5 to 50 m. The internal structure of the waves suggests upslope migration. The regional setting and sediments characteristics of these sediment waves,

together with the apparent absence of contour current activity indicate that probably formed by turbidity currents or related down-slope flows.

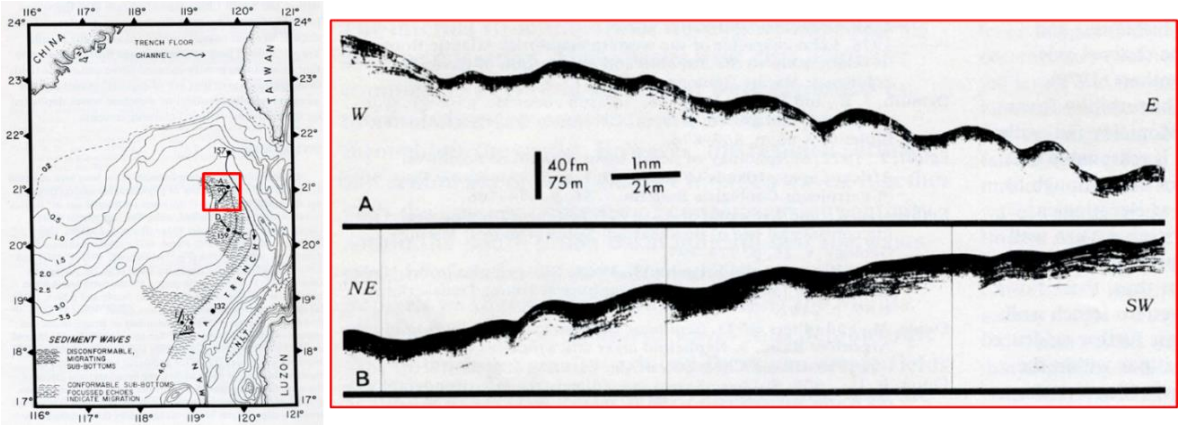

Figure V.1 - In the left, location of the sediment waves on seaward wall of Manila Trench at northern end of South China Basin. In the right, two echograms (3.5 kHz) across migrating sediment waves (location shown by the red square in the map). Modified from Damuth (1979).

Gong *et al.* (2011) identified two fields of sediment waves on the South China Sea Slope off southwestern Taiwan (Figure V.2 and V.3). Field 1 is located in the lower slope and the sediment waves there are overall oriented perpendicular to the direction of the down-slope gravity flow and canyon axis. Asymmetrical morphologies (the wavelengths range from 0.5 to 4 km, and the wave heights range between 7 and 117 m) and internal discontinuous seismic reflections suggest that the sediment waves underwent significant up-slope migration. The development of the sediment waves in field 1 in interpreted as the result of the interactions between down-slope turbidity currents and along-slope bottom (contour) currents. Field 2 is located near the continental rise and, in contrast, the sediment waves show more symmetrical morphologies (the wavelengths range from 1.5 to 5.4 km and the wave heights can be up to 110 m) and continuous reflections (that can be traced from one wave to another) suggesting a predominant vertical aggradation rather than up-slope migration. The development of the sediment waves in this field is mainly controlled by the WSW flowing bottom (contour) currents induced by the intrusion of the Northern Pacific Deep Water into the South China Sea.

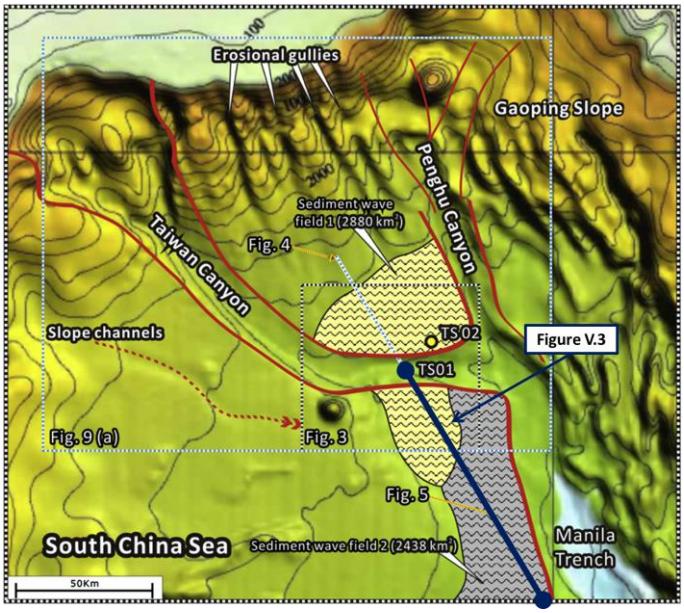

Figure V.2 - Bathymetric and location map of the two fields of sediment waves on the South China Sea Slope off southwestern Taiwan (Gong *et al.,* 2011). Sediment wave field 1 is in yellow and sediment wave field 2 is in grey. Dark blue line show the location of the seismic profiles shown in Figure V.3.

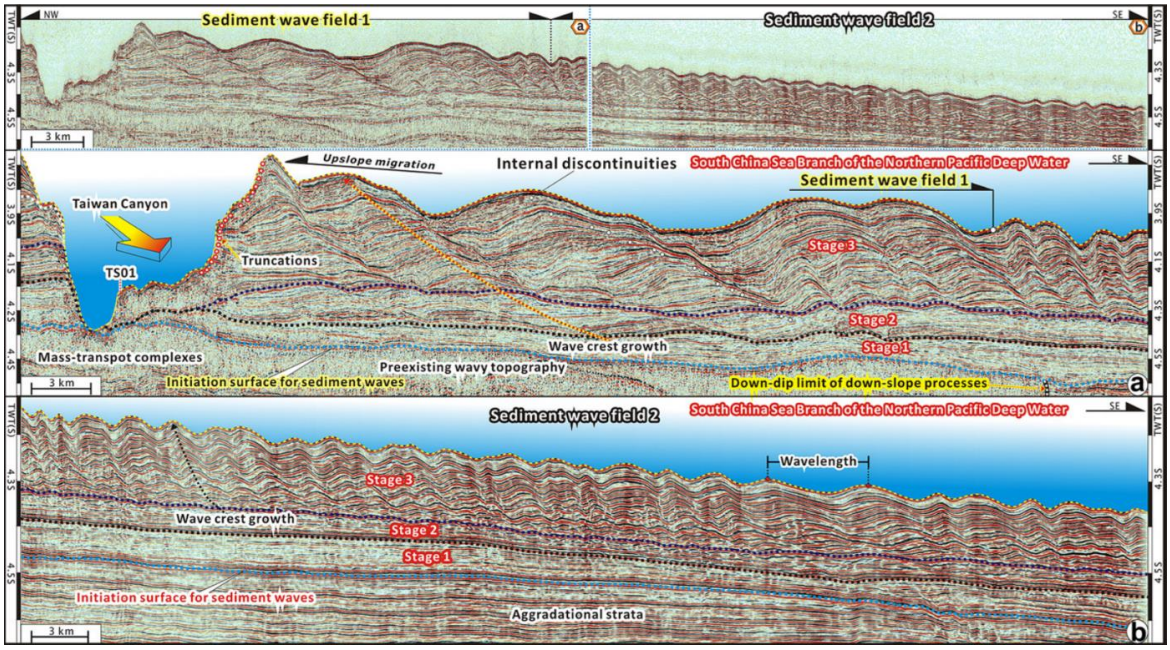

Figure V.3 - High-resolution seismic profiles showing the difference in geometries, morphology, and seismic reflection configurations between the sediment waves in fields 1 and 2 on the South China Sea Slope off southwestern Taiwan (Gong et al., 2011). See profile location in Figure V.2.

Li *et al.* (2013) studied the Plio-Quaternary unidirectionally migrating channels and contourites (which include sediment waves) on the northern slope of the South

China Sea, at water depths from 200 to 3000 m (Figure V.4). Here, the sediment waves' characteristics are upslope migration and an asymmetric geometry whose wavelengths and wave heights vary between 0.34 to 3.12 km and 14.7 to 125.7 m, respectively. Some of them developed on the drifts (Figure V.5).

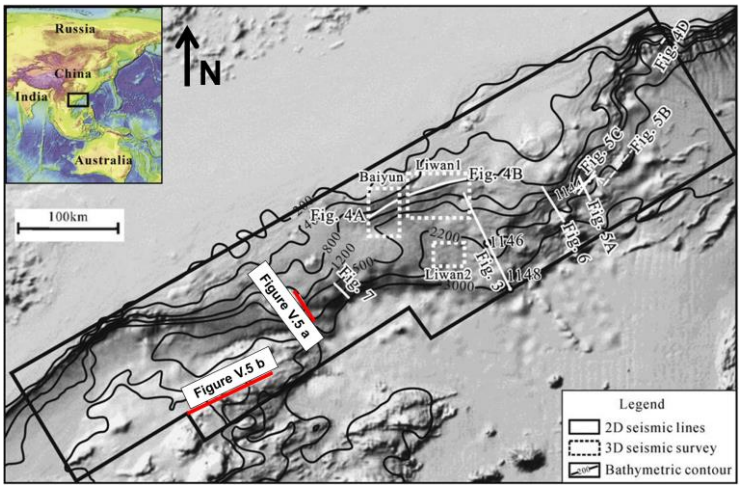

Figure V.4 - Location of the seismic section shown in Figure V.5 in the northern slope of the South China Sea (modified from Li *et al*., 2013).

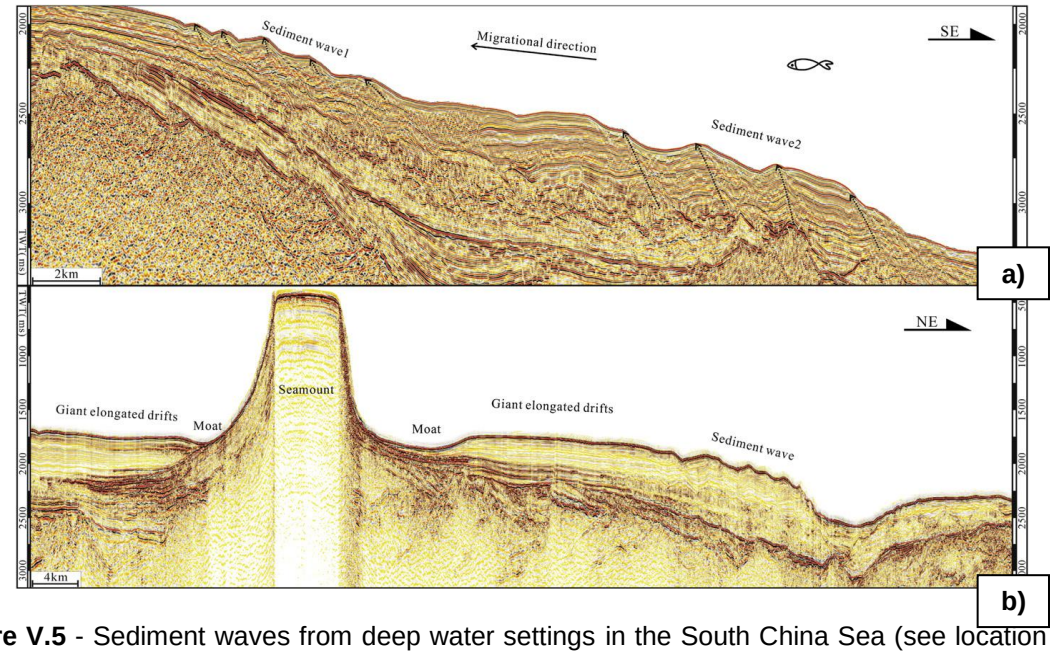

Figure V.5 - Sediment waves from deep water settings in the South China Sea (see location map in Figure V.4). Top profile (a): asymmetric waveforms, upslope migration, parallel to subparallel, moderate to low amplitude seismic reflection. Bottom profile (b): Some sediment waves develop with drifts (Li *et al.,* 2013).

Reeder *et al.* (2010) propose a distinctive formation mechanism for sand waves on the upper continental slope of the northern South China Sea, between 160 and 600 m water depth: internal solitary waves. These internal solitary waves, also called solitons, are generate from tidal forcing on the Luzon Ridge on the east side of the South China Sea and propagate west across the deep basin with amplitudes regularly exceeding 100 m (Figure V.6), dissipating extremely large amounts of energy via turbulent interaction with the continental slope, suspending and redistributing the bottom sediment (approximate 60 episodic, extremely energetic, large amplitude events each lunar cycle). The sand dunes are composed of fine to medium sand, with amplitudes exceeding 16 m and wavelengths exceeding 350 m and they exhibit an intermittent, irregular distribution over the slope (Figures V.7 and V.8).

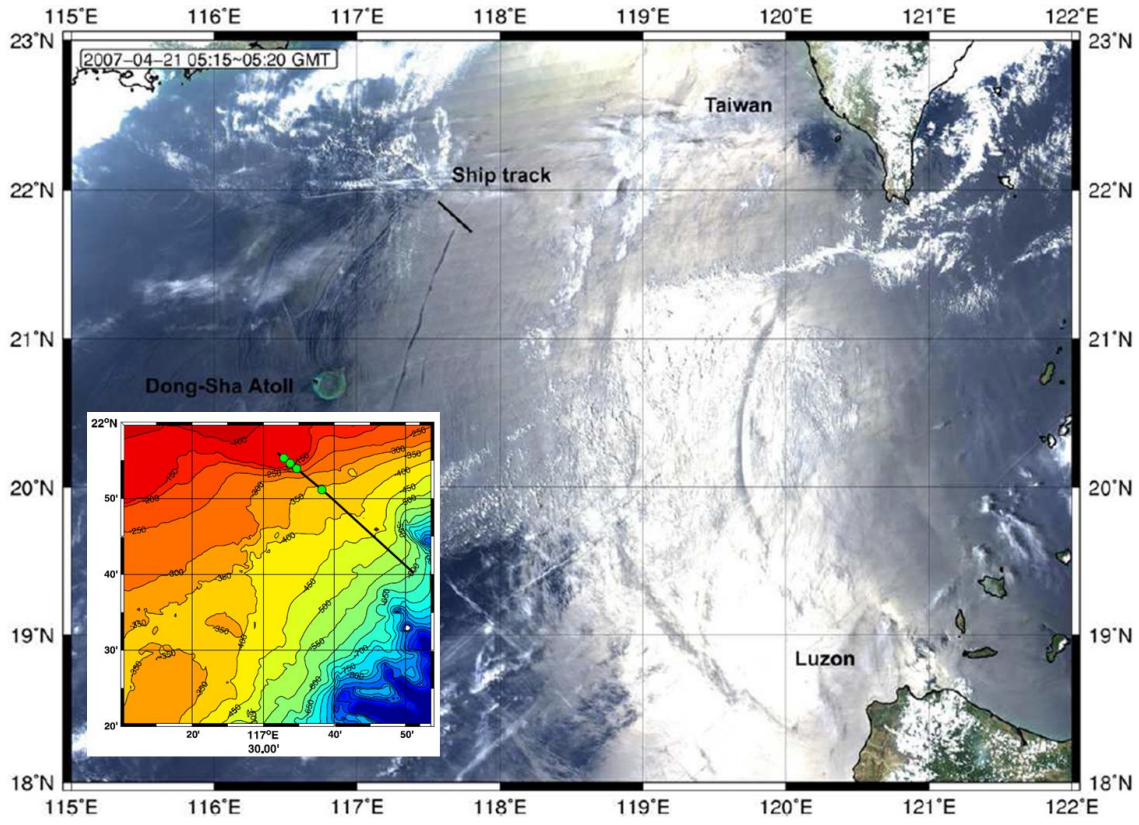

Figure V.6 - Bathymetric map of the upper continental slope in the South China Sea, with the acoustic profiling transect (black line; Figure V.7) and the locations of sediment grab samples (green circles). Depth in meters; (Reeder *et al.,* 2011). The dark circular bands represent the surface expressions pf Internal Solitary Waves.

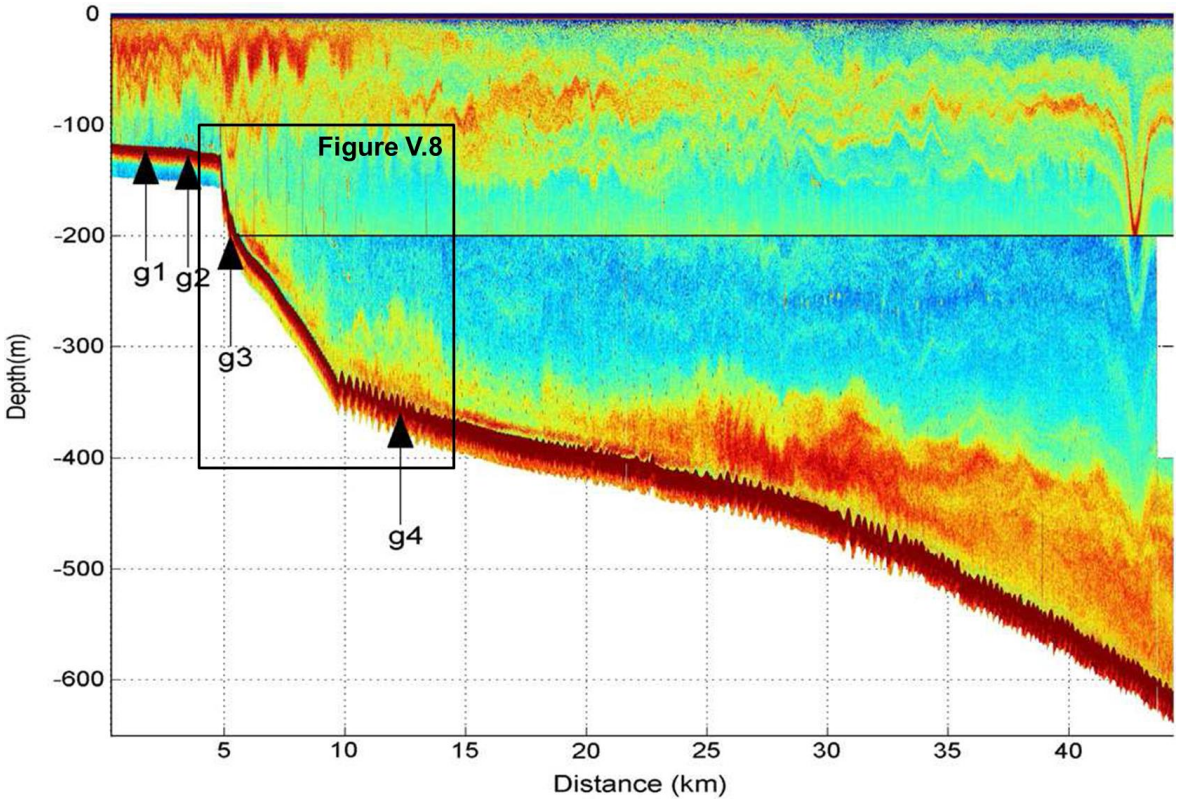

Figure V.7 - The water column structure of the Internal Solitary Waves (ISW) in the South China Sea. The ISW is propagating along the thermocline in the form of a single, large depression wave of 125 m amplitude. See location of the acoustic profile and the sediment grab samples (g1, g2, g3 and g4) in Figure V.6 (Reeder et al., 2010).

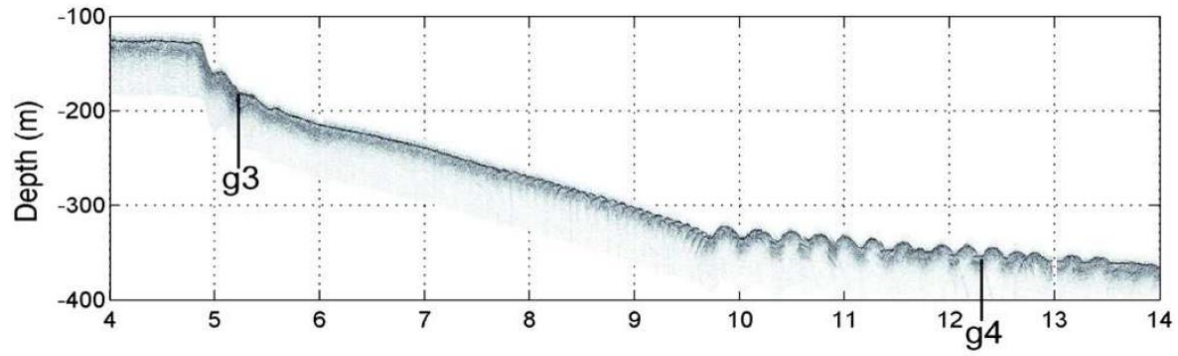

Figure V.8 - Sub-bottom profile acquired by a 3.5 kHz chirp sonar system showing part of the sand dunes observed (Reeder et al., 2010). See location in Figure V.7.

Previously, Karl *et al.* (1986) considered that internal-wave currents were responsible for the sand waves' occurrence in Navarinsky Canyon, Bering Sea, between 175 and 650 m water depth (Figure V.9 and V.10). They listed three main

reasons: (1) the energy of the internal waves could be amplified at the head of Navarinsky Canyon; (2) upslope boundary-layer intensification of internal-wave currents might be sufficient to move the sediments, and (3) the wavelengths of higher-frequency internal waves closely match the spacing of the sand waves. The best-developed sand waves' wavelengths and amplitudes range from 600 to 650 m and 5 to 15 m, respectively, at 150 to 225 m of water depth. The wavelength of the one-hour-period internal-wave ranges from 350 to 650 m in those water depths, suggesting a kinematic relationship between high-frequency internal waves and the sand waves.

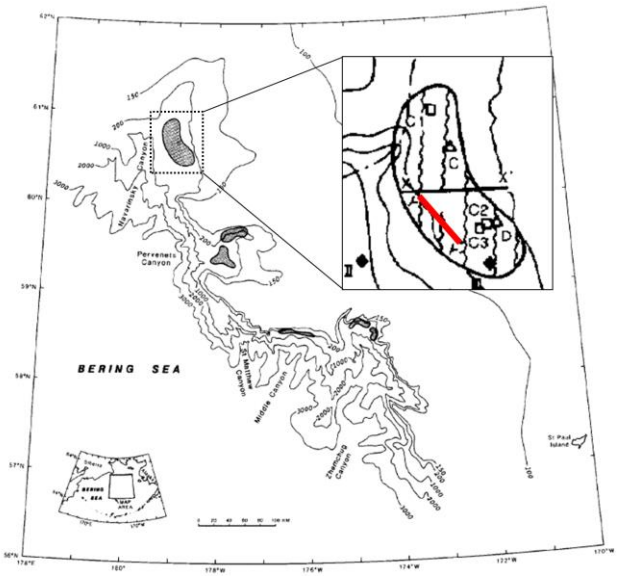

Figure V.9 - Location of the profile shown in Figure V.10 (red line), in the Navarinsky sand-wave field, Bering Sea (Karl et al., 1986).

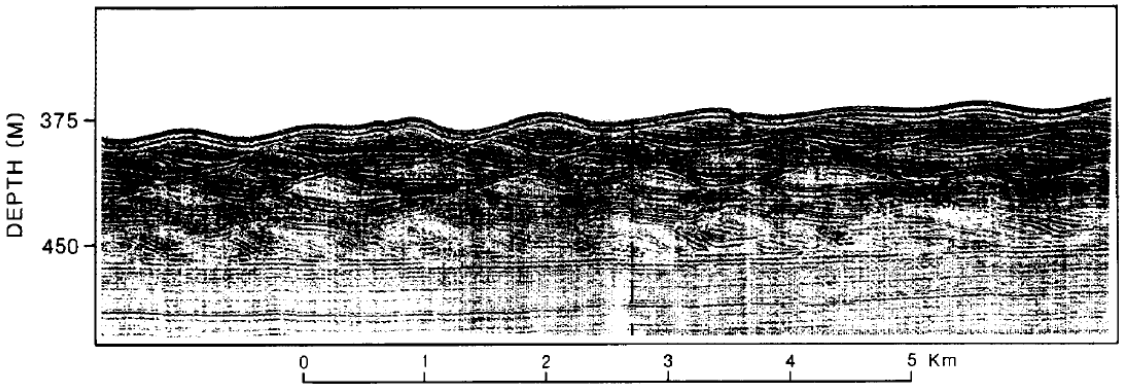

Figure V.10 - Mini-sparker profile showing examples f sand waves in the head of Navarinsky Canyon. Note the upslope asymmetry (Karl et al., 1986).

Messina Strait, Mediterranean Sea

More recently, Droghei *et al.* (2016) proposed that internal solitary waves (ISWs) induced by tides can produce an effective, unidirectional boundary "current" that forms asymmetric sand waves. They tested this hypothesis by examining a sand-wave field off the north entrance of the Messina Strait (Figure V.11), between 200 and 300 m water depth. The sand waves here have wavelengths between 60 and 120 m, and wave heights of 1.5 to 5 m; wave dimensions tend to increase northward. After combining field observations and numerical modelling, they present three key features to show ISWs can be the responsible mechanism for the sediment wave formation: (1) they produce fluid velocities capable of mobilizing bottom sediments; (2) the predicted refraction pattern resulting from the interaction of ISWs with bottom topography matches the observed deflection of the sand waves; and (3) predicted migration rates of sand waves match empirical estimates.

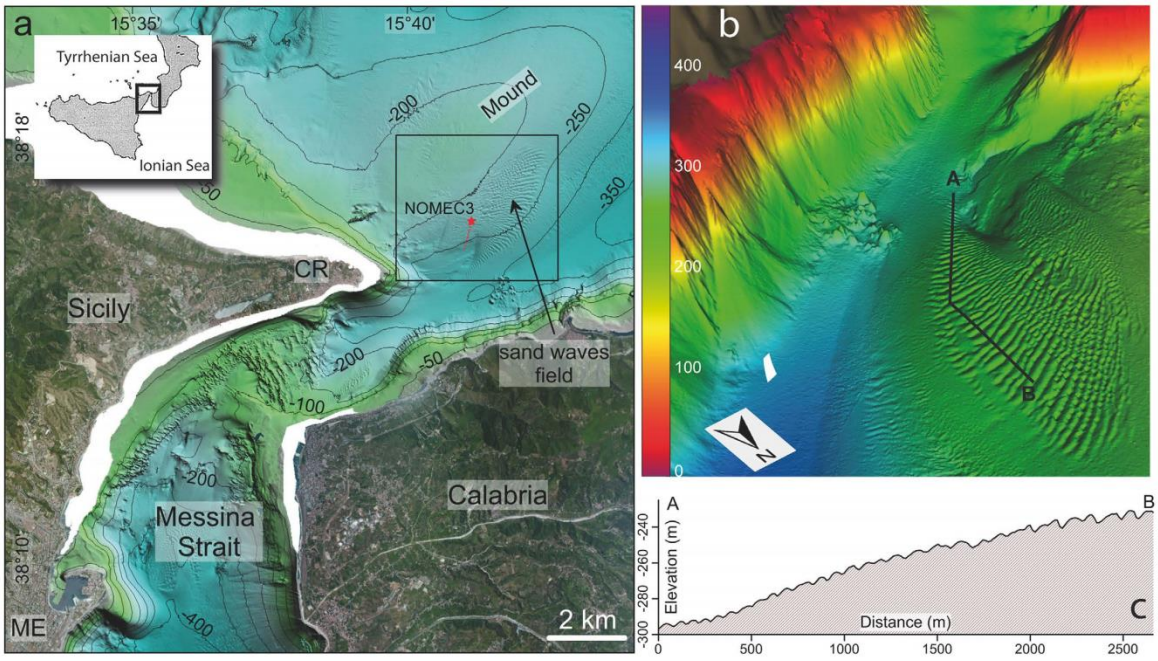

Figure V.11 - The Messina Strait and the observed sand-wave field. (a) Bathymetric map of the Messina Strait; (b) 3D zoom of the sand-wave field; (c) Bathymetric section of the sand-wave crests. Sand waves show variable cross-sections, from asymmetric (longer stoss side followed by shorter and steeper lee side) to more symmetric moving northward (Droghei *et al.,* 2016).

Var Sedimentary Ridge, Ligurian Sea

Migeon *et al.* (2000) studied the evolution of two fields of sediment waves (a surficial and a subsurface field) on the Var deep-sea fan (Ligurian Sea; see Figure V.12), at depths between 2000 and 2600 m.

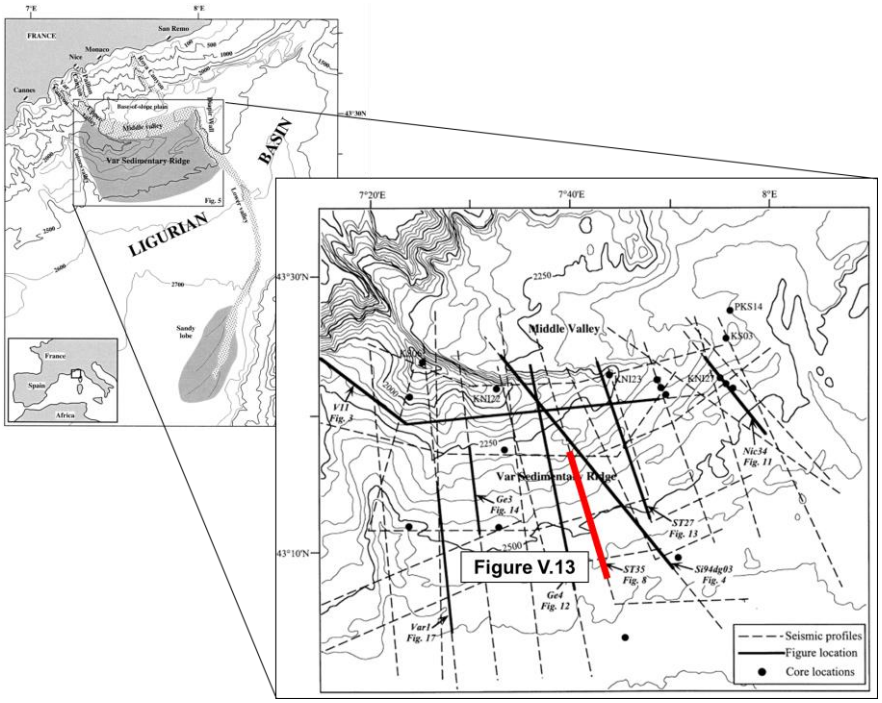

Figure V.12 - Location of the Var turbidite system within the Ligurian Basin. Red line: seismic profile of Figure V.13.

In the surficial field, sediment waves amplitudes range from less than 5 m to up as much as 60 m, with an average of about 20 m. Their wavelengths range from 600 to 7000 m, with an average of about 2200 m. The wave crests are subparallel to the Middle Valley and to the crest of the ridge. In the subsurface fossil wave field, amplitudes range from less than 10 to 50 m, with an average of about 25 m, and wavelengths range from 900 to 4400 m, with an average of about 2200 (this values only approximate the true wavelengths and amplitudes at the time of their deposition, because of the effects of sediment compaction and possible erosion of the crests). These sediment waves are constructed by turbidity currents that spill-over and spread sediments across the Ridge. The authors pointed out that spill-over energy, pre-existing morphology and sediment supply appear to be important control factors of the sediment wave distribution and evolution. Also, salt diapirs

may influence the formation of the sediment waves locally by deforming the upper sediment deposits and creating a pre-existing wavy topography. The development of sediment waves appears to be the fundamental element controlling the manner in which levees within an asymmetrical turbidite system may prograde, aggrade and migrate (Figure V.13).

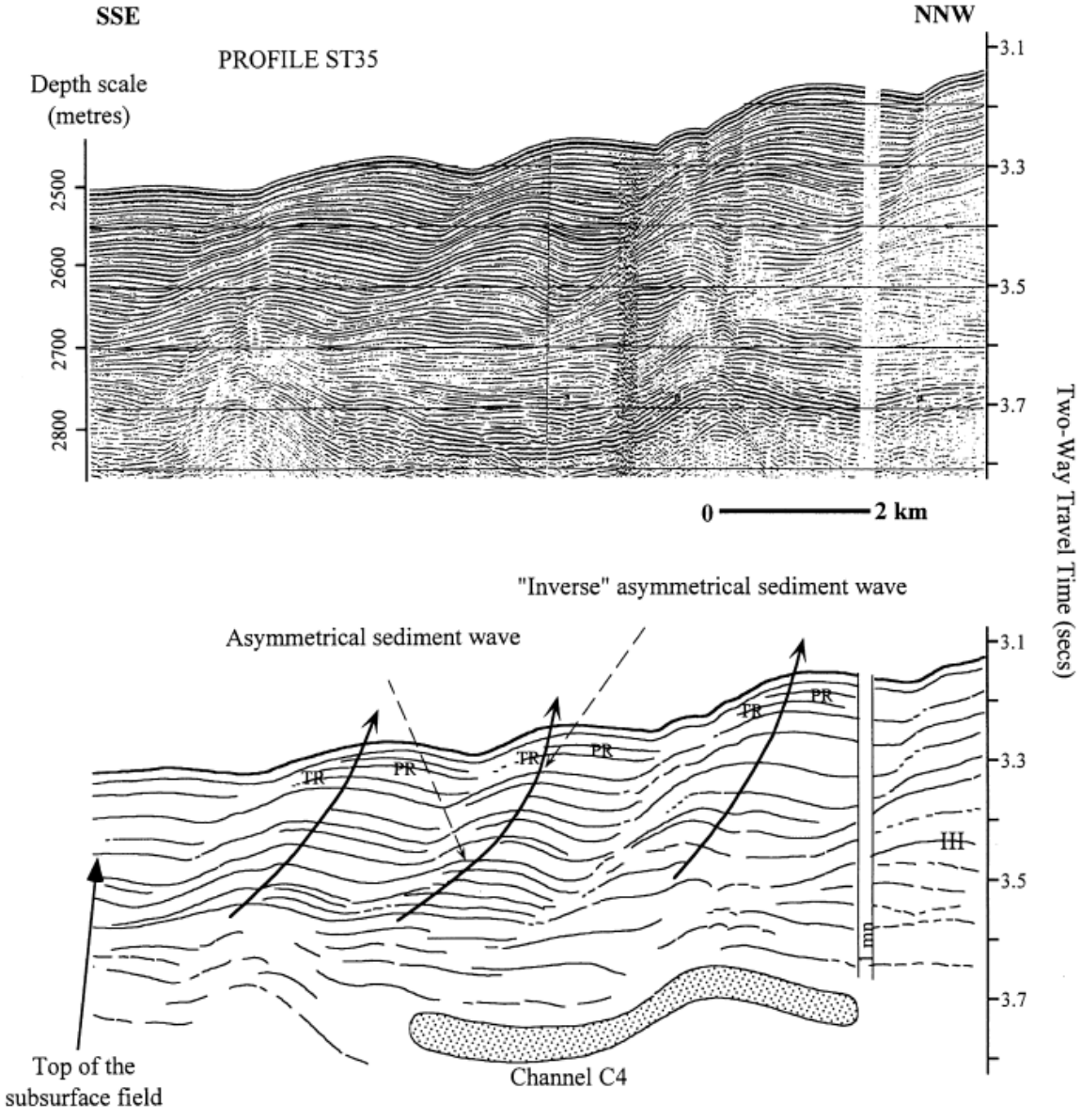

Figure V.13 - Sediment waves field in the middle part of the Var Sedimentary Ridge (Migeon et al., 2000). See profile location in Figure V.12.

V.2 Formation mechanisms and classification

Formation mechanisms

In summary, four main formation mechanisms have been proposed for sediment wave formation: (A) bottom currents; (B) turbidity currents; (C) internal waves; and (D) internal solitary waves.

(A) Bottom currents and (B) turbidite currents are the best studied mechanisms of sediment waves' formation (Figure V.14), in response to the 90's boom in climate change studies and due to the increasing demand for data on turbidity systems from the hydrocarbon exploration and production industry (Wynn & Stow, 2002). Bottom currents include also contourite currents and thermohaline currents. These types of sediment waves have been grouped on the basis of grain size into fine- and coarse-grained sediment waves by Wynn & Stow (2002) (see Table V.1). Fine-grained sediment waves are commonly found in areas where turbidity currents flow unconfined, as on the back slopes of channel levees (e.g. Var Sedimentary Ridge; Figure V.9; Migeon et al., 2000; Cartigny et al., 2011). The fine-grained sediment waves consist of mud to fine sand, with the coarser grain sizes deposited on the stoss side (Ercilla et al., 2002). The coarse-grained sediment waves are often located in the proximal part of the submarine fan systems, such as in canyons, channels, and channel-lobe transitions (e.g. Monterey Canyon; Xu et al., 2008; Wynn & Stow, 2002).

(C) Another proposed formation mechanism is internal waves (Karl et al., 1986; Flood, 1988; Flood & Giosan, 2002; Xu et al., 2008; Reeder et al., 2011; Droghei et al., 2016). Ocean internal waves are waves in the interior of the ocean which are generated when the interface between layers of different water densities (caused by a water temperature or salinity difference) is disturbed, usually caused by tidal flow over shallow bathymetry (iwww.link.springer.com). Flood (1988) presented the lee-wave model (Figure V.15), where a weakly stratified bottom flow is perturbed by the sediment topography leading to a change in the velocity structure of the flow. He showed that the near-bottom flow field associated with the lee waves creates a cross-wave asymmetry in bottom current velocity. This model

suggests that for a given wave, the ratio of downstream-upstream sedimentation rate varies primarily with flow velocity.

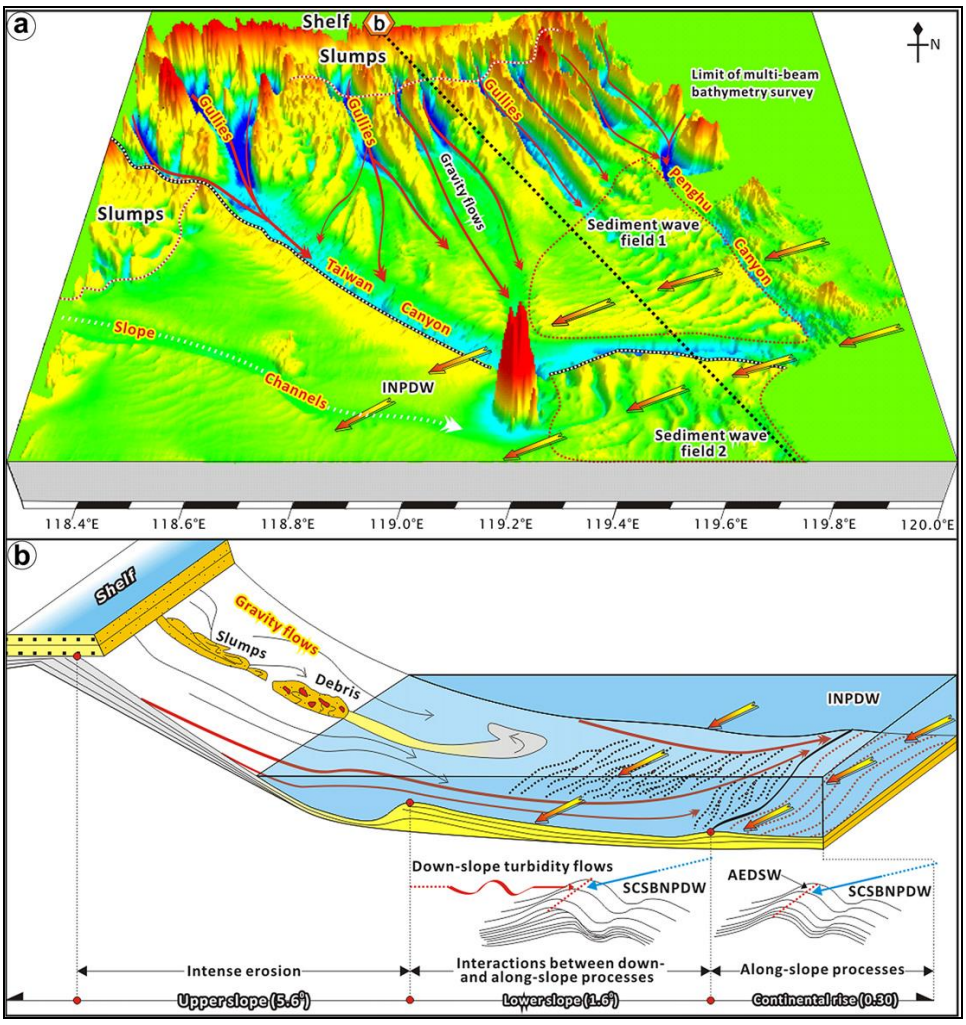

Figure V.14 - Example of bottom currents and turbidity currents interaction as a formation mechanism of sediment waves fields in South China Sea (Gong et al., 2012). (a) Three-dimensional bathymetric image showing the morphology and major depositional elements. Two sediment wave fields are shown up clearly in plan view. (b) Schematic diagram summarizing the major depositional processes in different region of the referred area. The upper slope is characterized by gravity flow erosion and sediment bypass. Sediments shed from the upper slope are transported basinward into the lower slope where the interactions of down-slope turbidity currents and along-slope bottom (contour) currents induced by the intrusion of the Northern Pacific Deep Water into the referred area (INPDW) result in the development of sediment wave field 1. Further basinward into the continental rise where sediment wave field 2 is develop, turbidity currents are diluted and along-slope bottom currents are the dominant processes. AEDSW = average elongation direction of sediment waves. SCSBNPDW = South China Sea Bottom (?) Northern Pacific Deep Water.

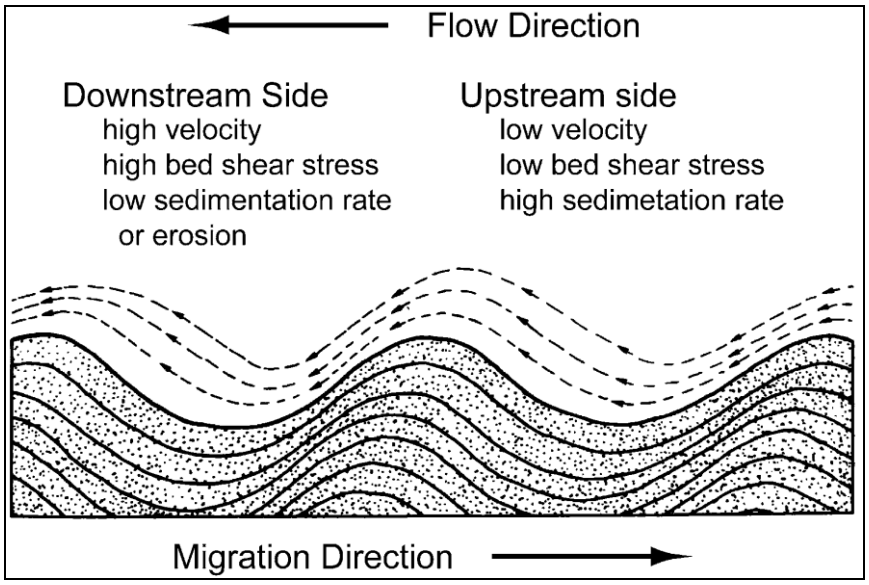

Figure V.15 - The lee-wave model of sediment wave evolution showing the interaction of a flowing stratified water column flowing over the sediment wave profile (Flood and Giosan, 2002).

D) Some authors relate the formation of sediment waves to a specific type of internal waves called internal solitary waves, or solitons (Figure V.5; Reeder *et al.,* 2011; Droghei *et al.,* 2016). These waves are generated by tidally forced currents flowing over topographical features in a stratified ocean (Reeder *et al.*, 2011).

In recent years, some large erosional sediment waves also have been interpreted as cyclic steps, Cartigny et al. (2011) made a general comparison between sediment waves and cyclic steps, which are a series of slowly upslope migrating bedforms, where each downward step (the lee side of the bedform) is manifested by a steeply dropping flow passing through a hydraulic jump before re-accelerating on the flat stoss side (Figure V.16; comparison in Figure V.17).

It is likely that all these processes have a role in sediment wave formation, depending on the specific depositional, hydrodynamic and tectonic setting.

Classification of sediment waves

Using a combination of grain size and wave-forming process, Wynn and Stow (2002) proposed the following sediment waves' classification: (1) bottom current sediment waves, (2) turbidity current sediment waves, or just (2) sediment waves, if the origin is "unknown" (see Table V.1).

Figure V.16 - Schematic drawing of a train of downslope asymmetrical cyclic steps, beneath a turbidity current (Cartigny et al., 2011).

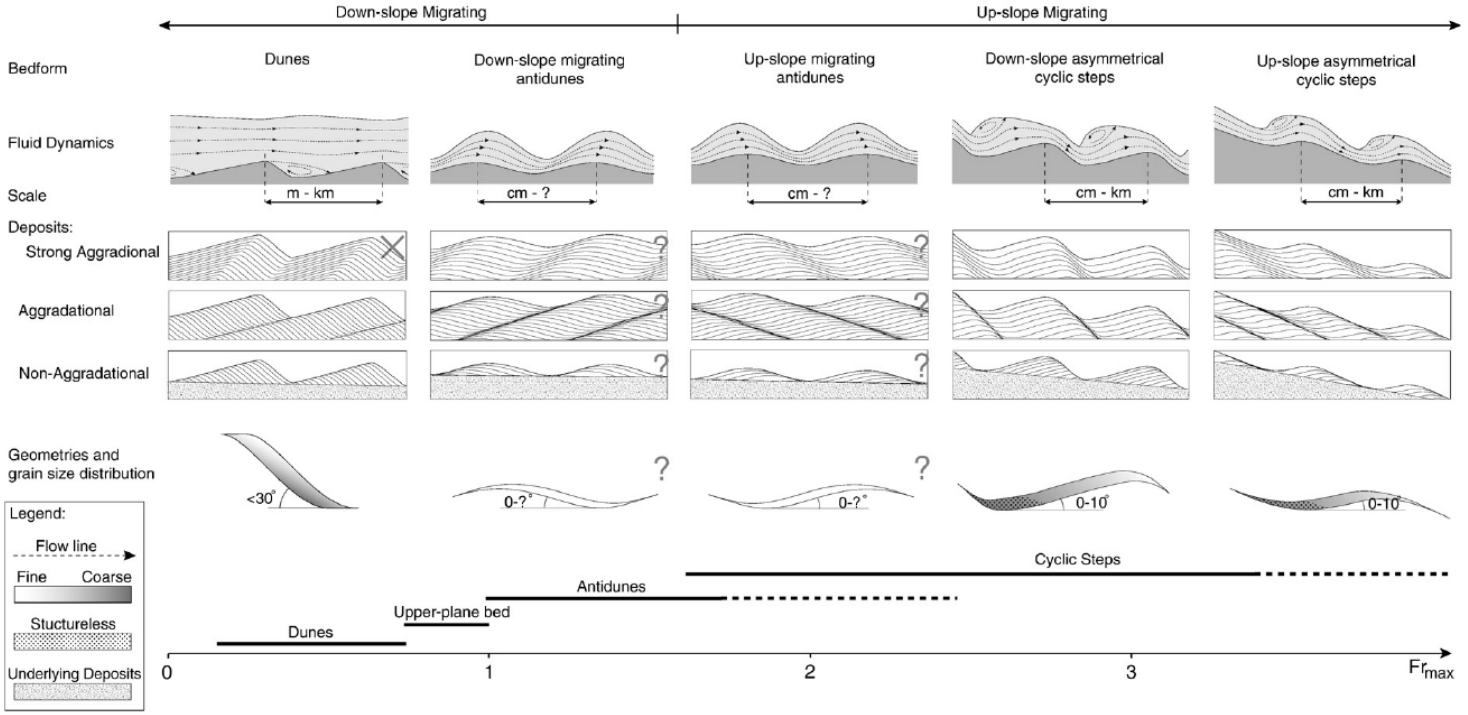

Figure V.17 - Comparison of properties of three possible interpretations of sediment waves: dunes, antidunes and cyclic steps (Cartigny et al., 2011). The bars of the lowermost graph show the different bedforms related to their formation conditions expressed by the maximum value of the Froude number over a bedform.

Table V.1 - Summary of characteristics for different types of sediment waves and also soft sediment deformation features (modified from Wynn and Stow, 2002).

Wave-forming process	Turbidity current	Turbidity current	Bottom current	Bottom current	Soft sediment deformation (e.g. creep folds)
Sediment grain size	Fine-grained (mud and silt dominated)	Coarse-grained (sand and gravel dominated)	Fine-grained (mud and silt dominated)	Coarse-grained (sand and gravel dominated)	Varied – usually fine-grained (mud/silt dominated)
Environment	Channel levees, continental slope/rise	Canyons, channels and canyon/channel mouths	Sediment drifts on basin floor/lower slope/rise	Topographic ridges, continental slope, b-c passages	Varied – potentially any submarine slope
Wavelength	Up to 7 km	Usually up to 1 km, rarely larger	Up to 10 km	Up to 200 m	Up to 10 km
Wave height	Up to 80 m	Up to 10 m	Up to 150 m	A few metres	Up to 100 m
Key features	Usually on slopes of 0.1–0.7° Wave dimensions progressively decrease downslope Wave asymmetry usually decreases downslope Crests are roughly parallel to regional slope Waves migrate upslope/ upcurrent	Crests aligned perpendicular to flow direction Can show decrease in dimensions at channel margin Morphology is often irregular/disrupted Migration direction variable Often associated with erosional scours	Wave dimensions decrease near edge of wave field Wave symmetry decreases near edge of wave field Waves on slopes are aligned oblique to slope Most waves on slopes migrate upcurrent and upslope Crests are straight or slightly sinuous	Can occur as straight waves or barchans Both types aligned perpendicular to flow Barchans common where sediment supply is poor Barchan migration is downcurrent Ripple patterns show peak flow near barchan crest	Most common on slopes of >2° Oriented perpendicular to maximum slope Do not show true lateral migration Usually show broad crests and narrow troughs Typically random scatter of dimensions

Chapter VI. Migrating sediment waves in the Ionian Sea

In this chapter we describe the three major fields of migrating sediment waves that can be observed in the Ionian Sea, on the basis of the available data for this study. We analyze each area in turn and show the evidence available from high resolution seismic profiles and from multibeam bathymetry.

In order to be able to correlate the observations between the different seismic profiles, some of the major unconformities (delimiting seismic sequences) and well defined major turbidites (Homogenite/Augias Turbidite, HAT – 365 AD; Polonia et al., 2013; Deep Transparent Layer, DTL – 14kyr b.p.; Polonia et al., 2013; and Thick Transparent Layers, TTL – 650kyr±100kyr; Hieke et al., 2000) have been identified on the few available seismic profiles and correlate using the Kingdom Suite Software.

In the absence of borehole constrained age interpretations of seismic profiles in the study area, and in order to assign tentative dates to the various episodes of sediment wave formation, the top of the Messinian (5.3 Myr) was interpreted on all the relevant seismic profiles. If a constant sedimentation rate is assumed until present, a value of 10cm/1000yr is obtained; However, according to Cita, Ryan & Kidd (1979) a value of 14cm/1000yr has been determined, for the Pleistocene, and an average value of about 6cm/1000yr for the Pliocene, obtained at DSDP Site 374 in the Ionian Sea, close to the study area (Cita, Ryan and Kidd, 1978). An age of 2.58Myr was assumed for the Plio-Pleistocene boundary (International Chronostratigraphic Chart, v2016/12).

After tentative dates have been assigned to the relevant reflectors, we show how the sediment wave pattern has changed through time in the three main fields, if the sediment waves are migrating or if only vertical aggradation is taking place, and propose a tentative age for end of the sediment wave formation in Line14.

We conclude this chapter with a proposal of possible formation mechanisms for the observed fossil and active sediment waves, and relate them with the active tectonics in the study area.

VI.1 Major Fields of Sediment Waves in the Ionian Sea

Gutscher *et al.* (2015) and San Pedro *et al.* (2016) identified for the first time the presence of active sediment waves in the study area based on bathymetric surveys (see alternating green and blue lines in Figure II.7; see purple lines delimited by dashed rectangles in Figure VI.1). However, to our knowledge, fossil seismic wave fields have never been identified before in this area. Here we report the first identification of several fossil migrating sediment wave fields detected in the Ionian Sea and also images of the active fields at depth, based on high resolution seismic profiles acquired during the CIRCEE Cruise (Gutscher *et al.*, 2013; 2015).

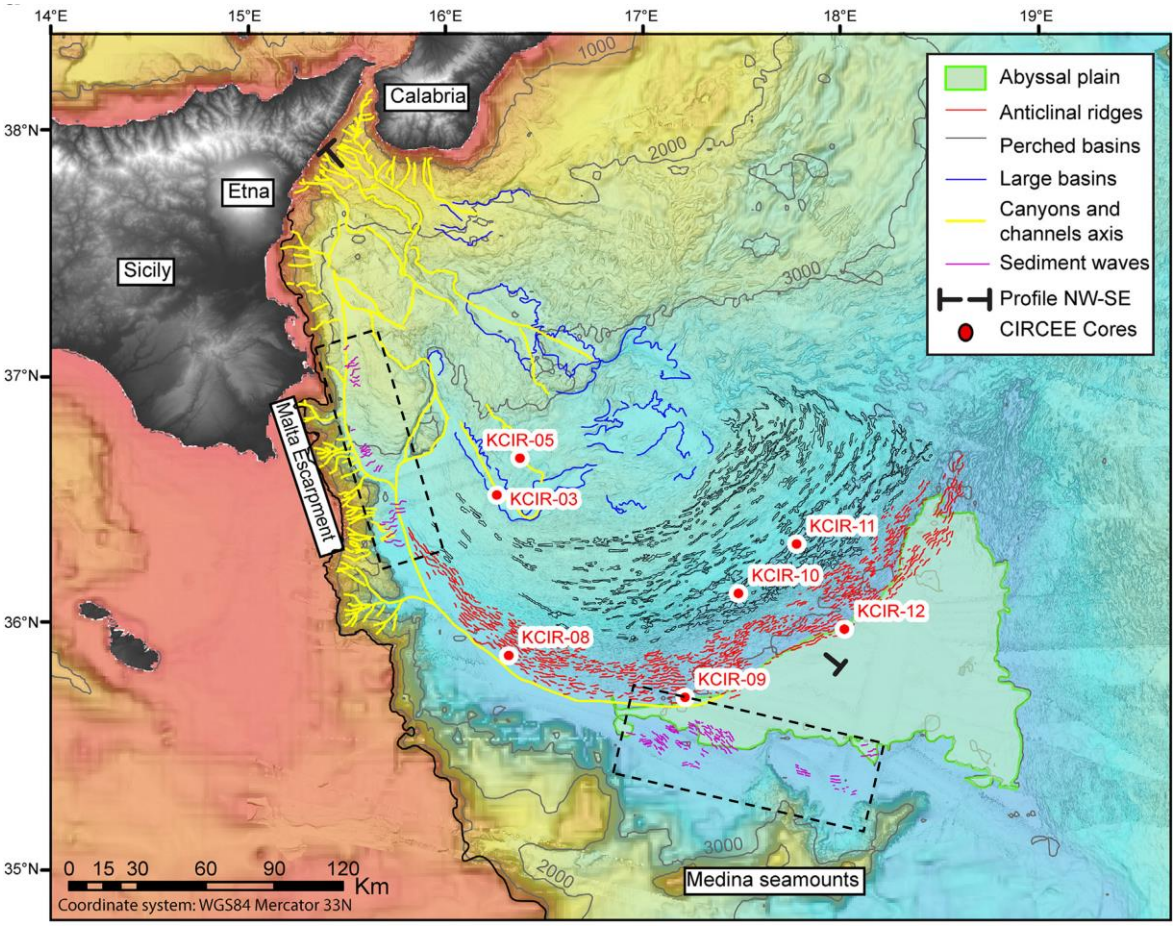

Figure VI.1 - Morpho-bathymetric interpretation of the Calabrian accretionary wedge (modified from San Pedro et al., 2016). Yellow lines: canyons and channels axis. Purple lines delimited by dashed rectangles: active sediment waves.

In total, eight seismic reflection profiles were interpreted to characterize these sedimentary structures: profiles 01, 08-02, 09, 10, 11-01, 13, 14 and 15 (Figure VI.2). An unpublished high-resolution bathymetric image for area A was also kindly made available for this study by M.-A. Gutscher, in which it is possible to observe a presently-active sediment wave field and correlate it with the seismic profiles that cross that area (Figure V.3).

A detailed observation of the seismic profiles has allowed the identification of three sediment wave fields in the study area (Figure VI.2). These include both presently-active sediment waves (observed in fields A and C) and fossil sediment waves (observed in all three fields, A, B and C).

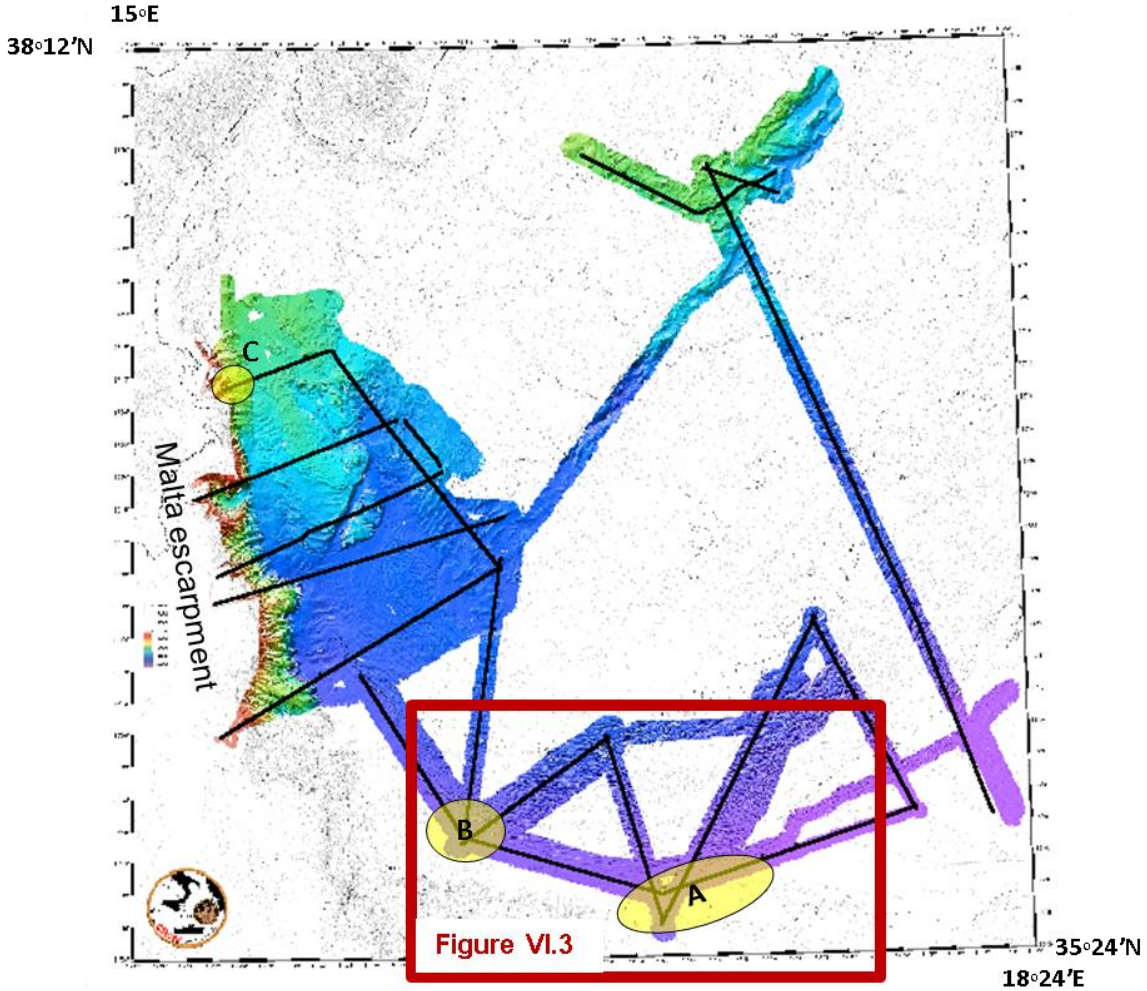

Figure VI.2 - Bathymetry map from CIRCEE survey with the multichannel seismic reflection profiles, respectively. Yellow areas represent the location of the sediment waves' fields observed and studied in this work, based only on the observation of the seismic profiles.

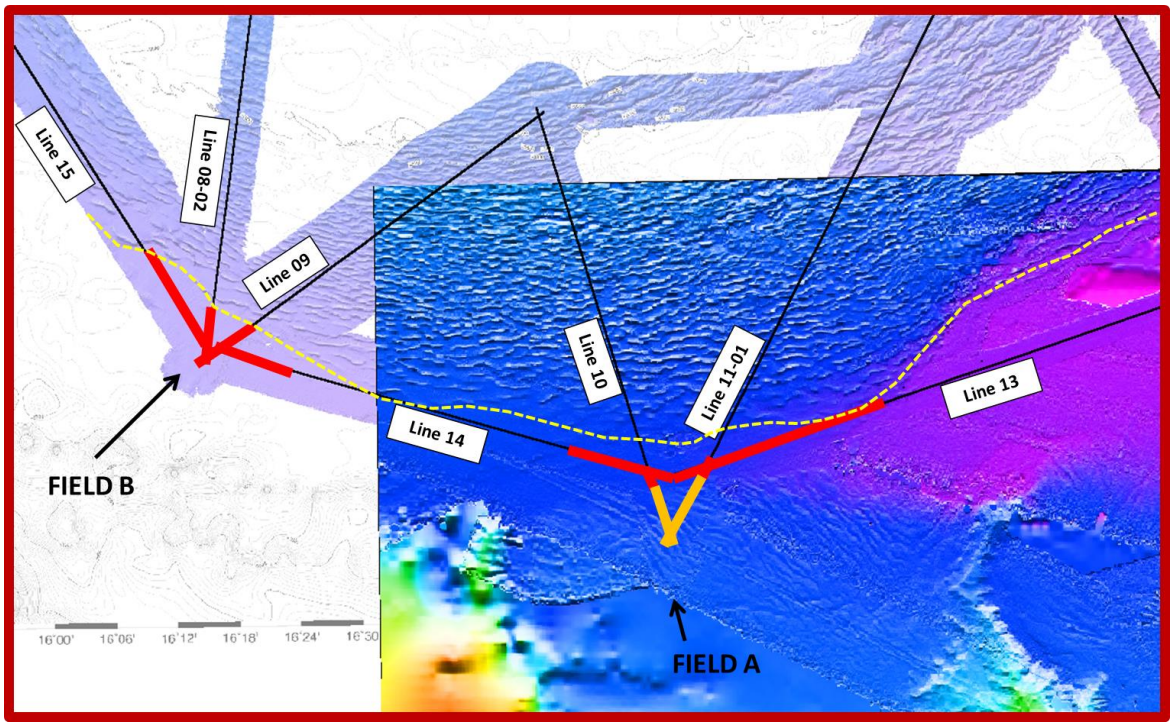

Figure VI.3 – Detailed unpublished bathymetric image around sediment wave field A on top of the bathymetric survey depicted in Figure VI.2 on the sediment wave fields A and B. The color traces indicates the segments of the seismic profiles where the sediment waves were observed. Yellow lines: present-active sediment waves. Red lines: fossil sediment waves. Light yellow dashed line: deformation front of the Calabrian accretionary wedge. The high-resolution bathymetry map shows clearly a present-active sediment field in Area A (courtesy from Marc-Andre Gutscher; MS in prep. Gutscher *et al*.).

Figures VI.4 to VI.12 show seismic images of the sediment wave fields as observed in Areas A, B and C.

Sediment waves in Field A

Field A is the southernmost field of sediment waves in the study area (Figure VI.3). It is located closer to the Ionian Abyssal Plain, between the 3500 and 4000 m isobaths. The crests of the presently-active migrating sediment waves are perceptible from the high-resolution map (Figure VI.3 and VI.19). They seem to be roughly perpendicular / oblique to the main turbidite channel (see yellow line in Figure VI.1) and deformation front of the wedge. These recent bedforms can be seen in two of the seismic profiles that cross this field, lines 10 and 11-01 (Figures VI.5 and VI.6, respectively), which are perpendicular to the deformation front of the

Calabrian accretionary wedge (yellow lines in Figure VI.3). In the all four seismic profiles that cross this field it is possible to identify fossil migrating sediment waves (Figures VI.4 to VI.7).

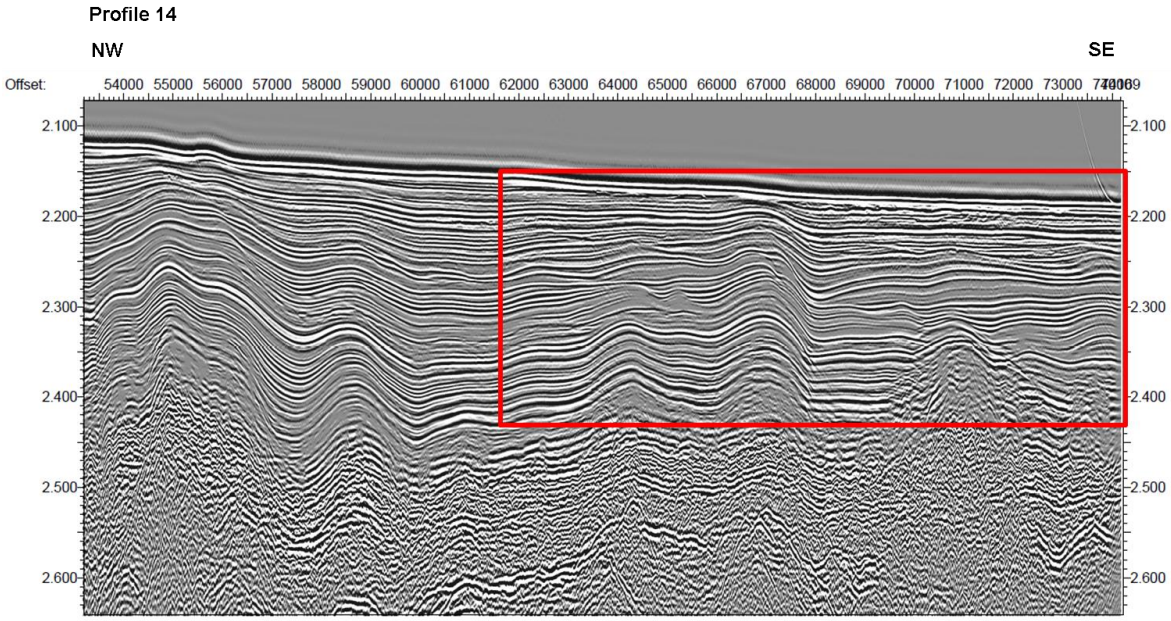

Figure VI.4 - Location of fossil sediment waves (red rectangle) of field A in seismic profile 14. See location of the seismic line in Figure V.3.

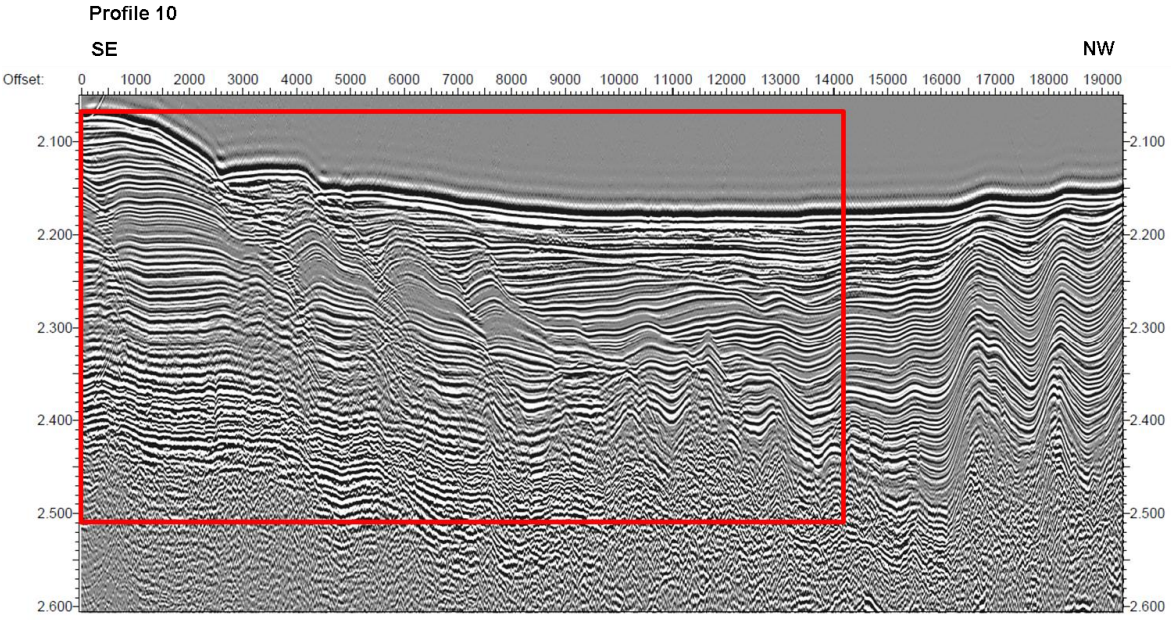

Figure VI.5 - Location of presently-active and fossil sediment waves (red rectangle) of field A in seismic profile 10. See location of the seismic line in Figure V.3.

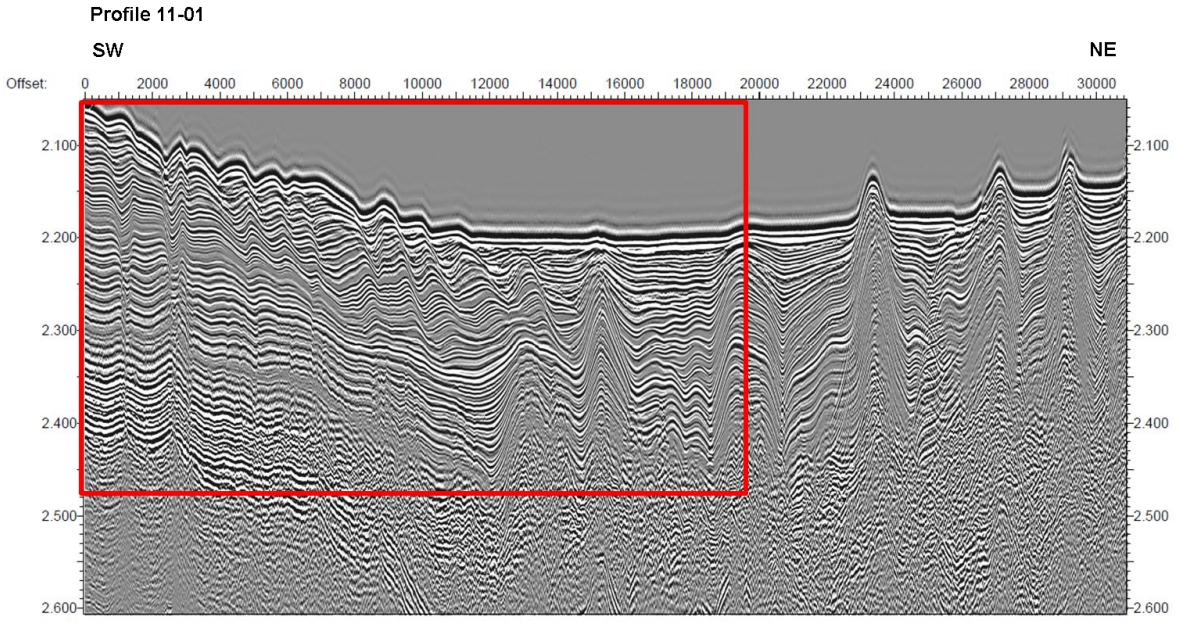

Figure VI.6 - Location of presently-active and fossil sediment waves (red rectangle) of field A in seismic profile 11-01. See location of the seismic line in Figure V.3.

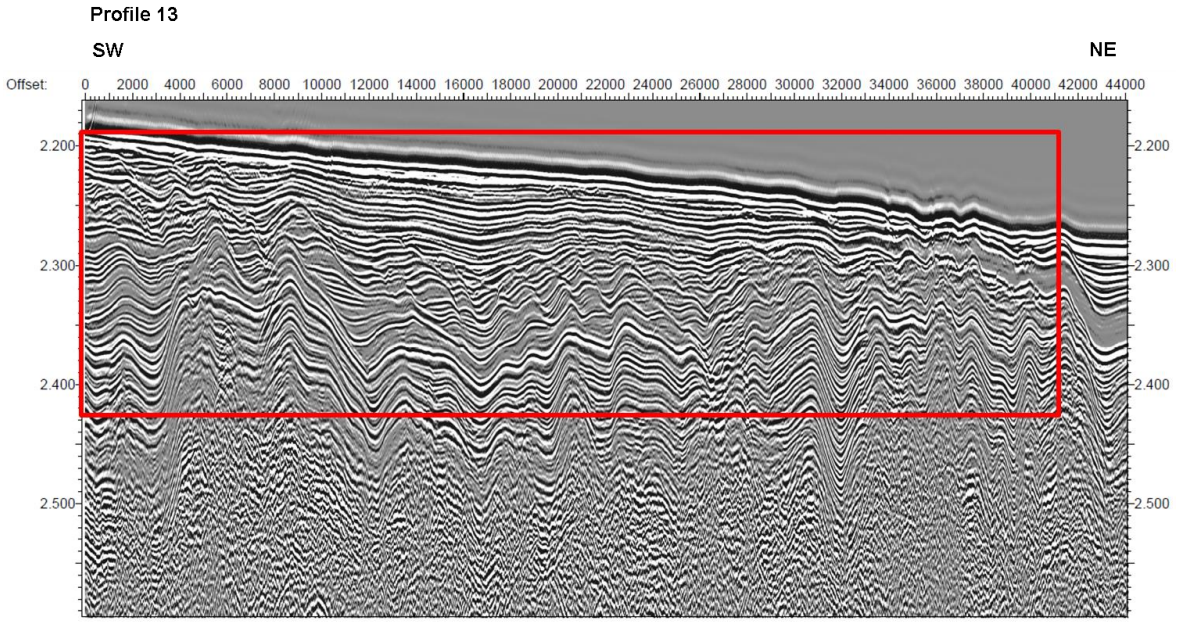

Figure VI.7 - Location of fossil sediment waves of field A in seismic profile 13. See seismic line location in Figure V.3.

Sediment waves in Field B

Field B is located northwest from field A (Figure VI.3), also between 3500 and 4000 m isobaths. There are no bathymetric evidences (CIRCCE data) of active sediment waves in this area, as shown by the seismic profiles that cross this field (Figure VI.8 to VI.11), although they may exist further south. Only fossil sediment waves are visible in the seismic profiles. The perpendicular lines to the deformation front show that these ancient bedforms are buried in the zone turbidite channel that surrounds the deformation front of the accretionary wedge (Figures VI.1, VI.9 and VI.10; San Pedro *et al.,* 2016). In Section IV.2, the fossil sediment waves from profile 14 will be analyzed in detail to date the several episodes of sediment wave formation and abandonment.

Sediment waves in field C

Field C is only represented on seismic profile 01 (Figure VI.12), which was the northernmost acquired seismic line in the CIRCEE-HR survey. This line begins on the midslope offshore Augusta (see location in Figure VI.2). Both active and fossil sediment are observed.

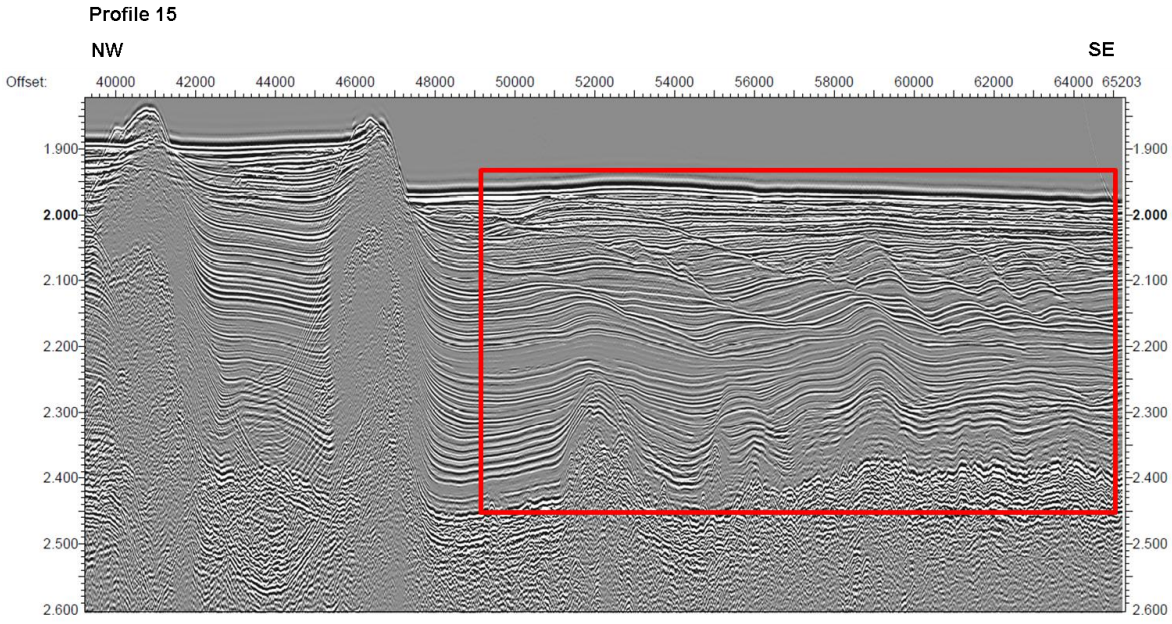

Figure VI.8 - Location of fossil sediment waves (red rectangle) of field B in seismic profile 15. See location of the seismic line in Figure V.3.

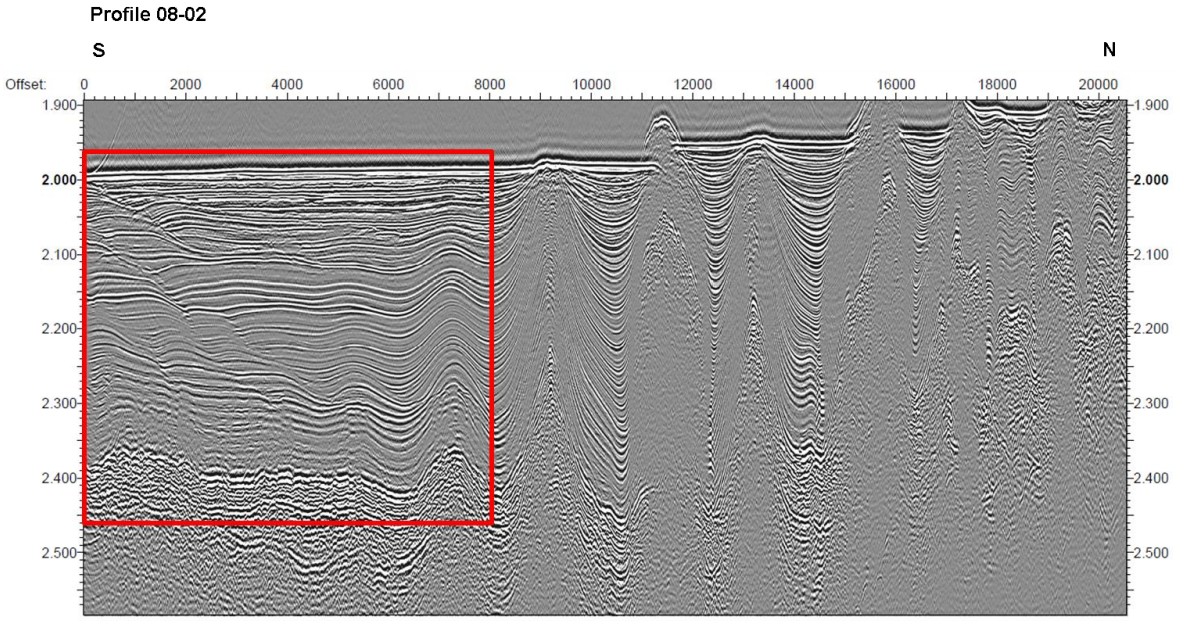

Figure VI.9 - Location of fossil sediment waves (red rectangle) of field B in seismic profile 08-02. See location of the seismic line in Figure V.3.

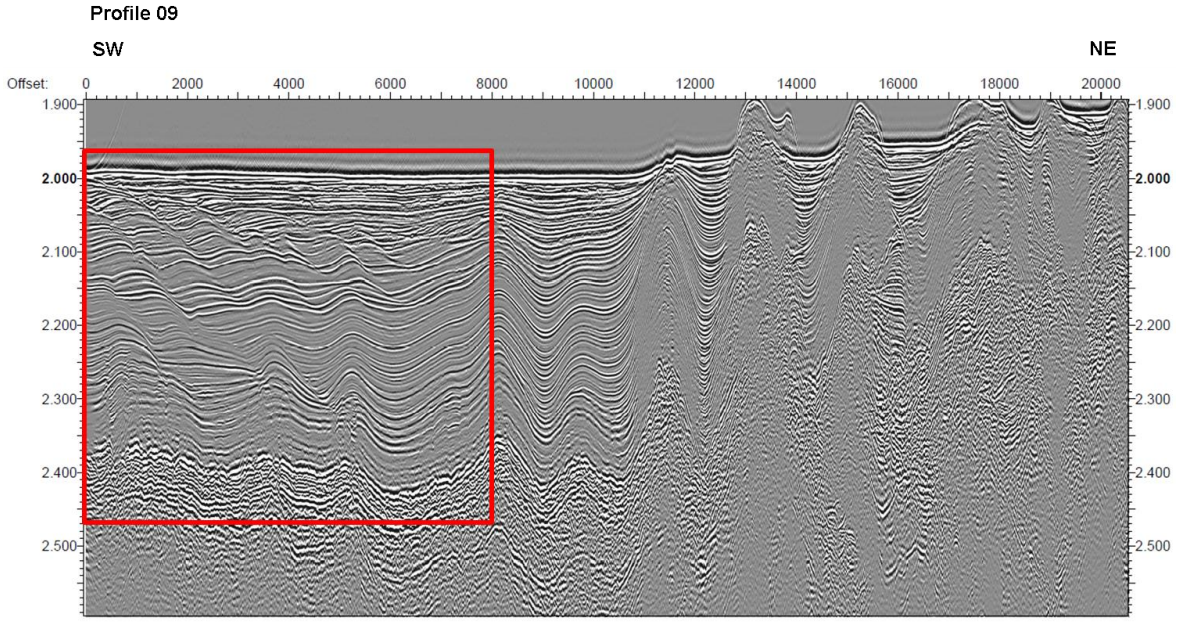

Figure VI.10 - Location of fossil sediment waves (red rectangle) of field B in seismic profile 09. See location of the seismic line in Figure V.3.

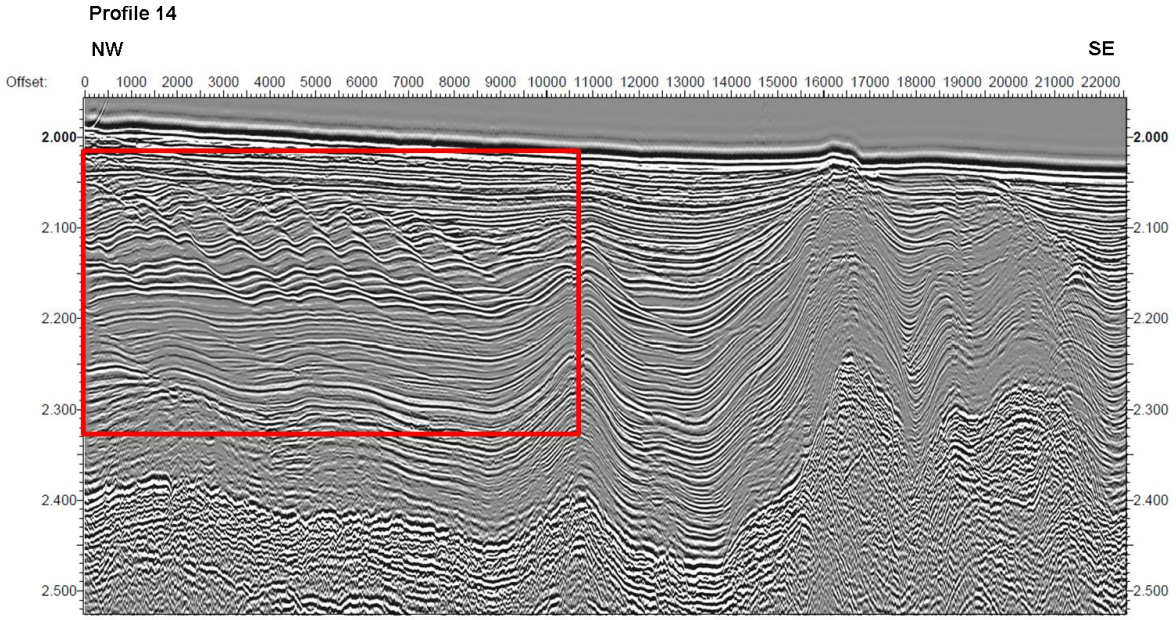

Figure VI.11 - Location of fossil sediment waves (red rectangle) of field B in seismic profile 14. See location of the seismic line in Figure V.3.

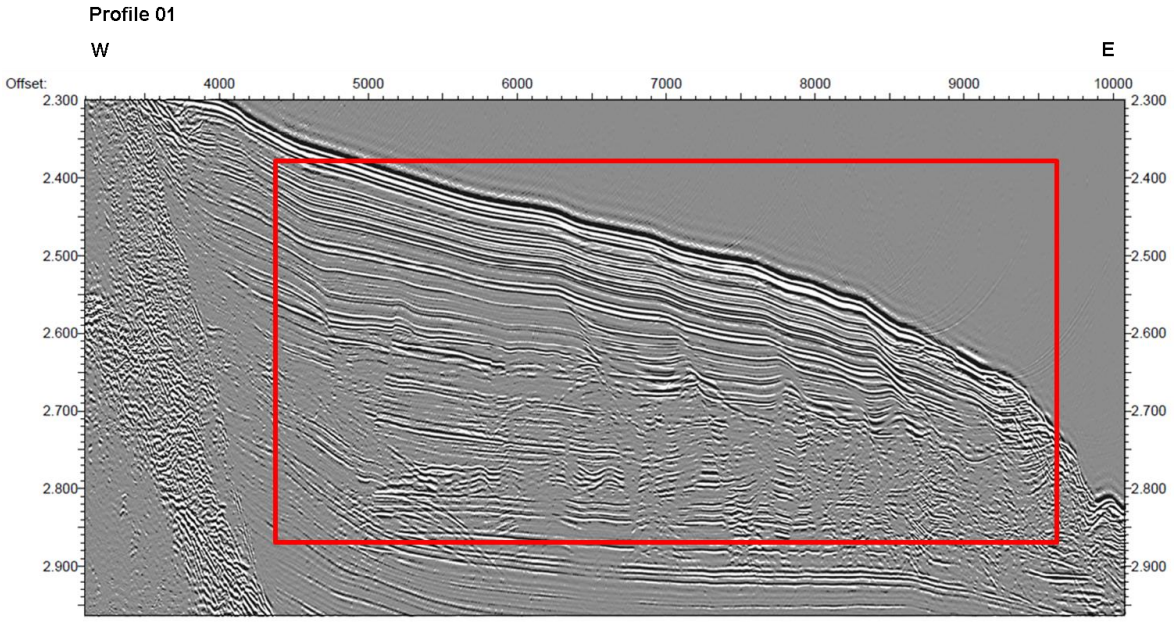

Figure VI.12 - Location of fossil sediment waves of field C in seismic profile 01. See location of the seismic line in Figure V.2.

VI.2 General interpretation of the CIRCEE-HR seismic profiles

In order to produce a geological and seismo-stratigraphic interpretation, the available 2D seismic reflection data from the study area, after navigation correction, was imported into a seismic database and interpreted using the seismic interpretation package, *Kingdom Suite 2015*.

First, major seismic horizons such as the top of the Messinian evaporites or the TTL boundary horizons) were mapped and correlated across the few available multichannel seismic profiles that cross the Ionian Abyssal Plain and the deformation front of the Calabrian accretionary wedge - profiles 12 (Figure VI.14), 13 (Figure VI.15) and 16-01 (Figure V.16). The seismic attribute Envelope was used to better identify the major turbidity episodes and to improve the lateral correlation.

Then, the correlation of those major seismic horizons was extended into the zones in which the sediment waves were observed. Due to the complex geology of the region and to the fact that we only had access to the CIRCEE-HR 2D multichannel seismic survey, the horizons correlation was difficult and sometimes impossible. Despite this, the boundary horizons of the several formation episodes, mainly of the fossil sediment waves, could be correlated with the same confidence.

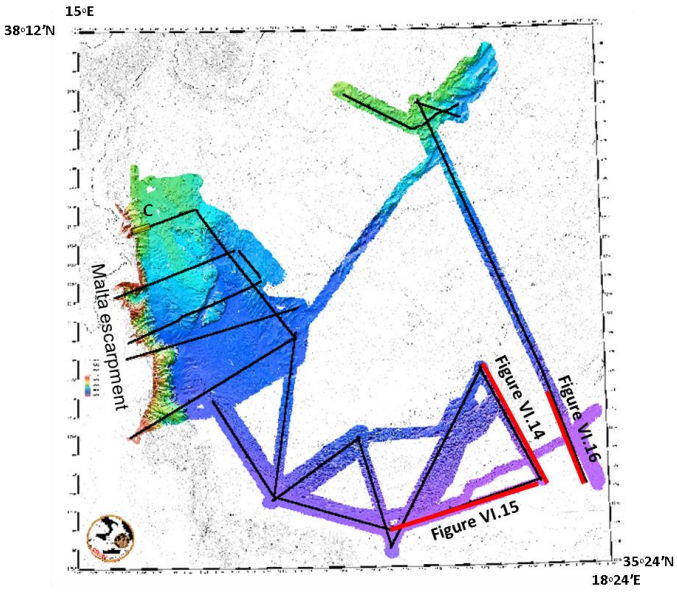

Figure VI.13 - Location map of the CIRCEE seismic profiles and Figures VI.14, VI.15 and VI.16.

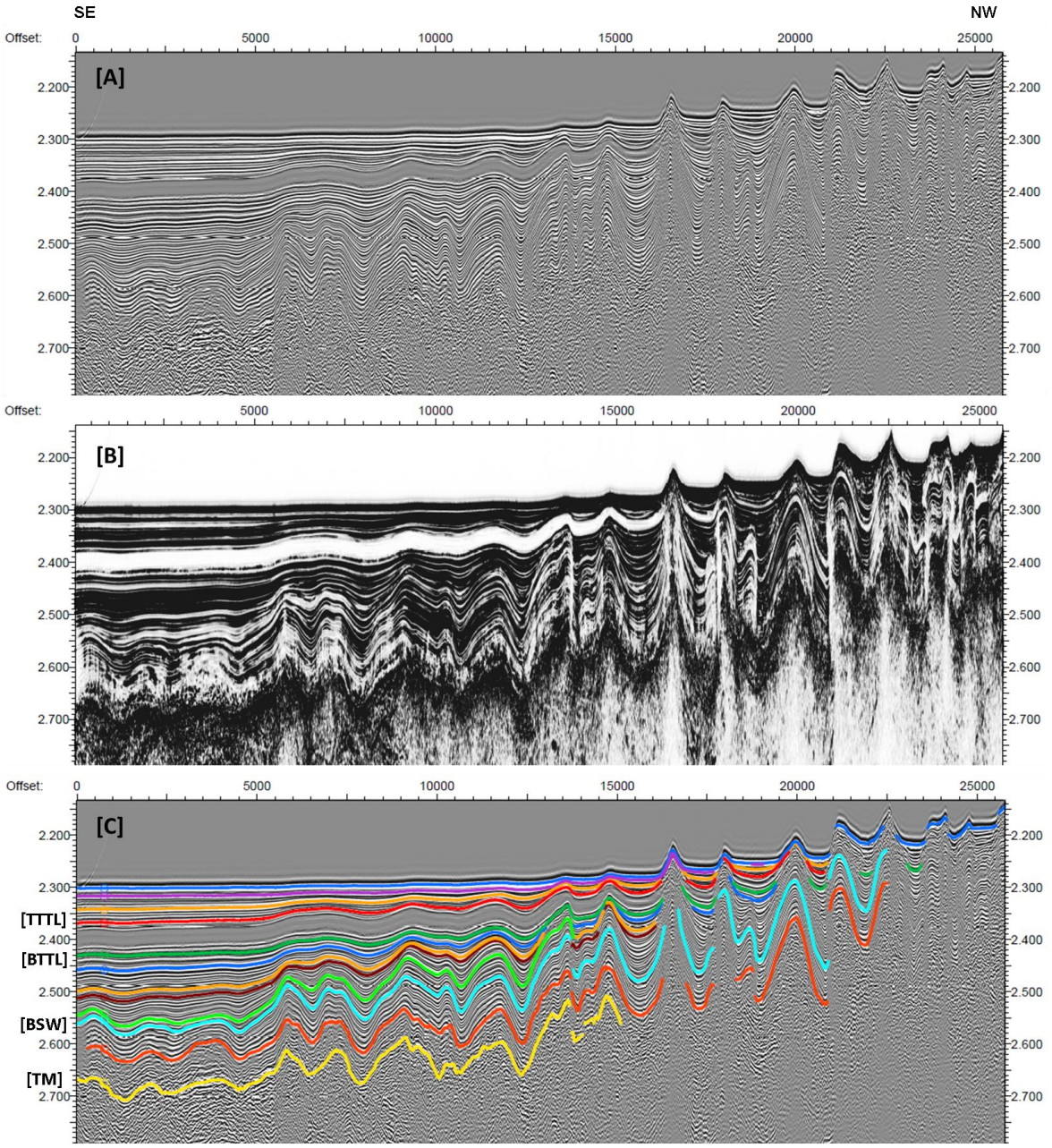

Figure VI.14 – Multichannel seismic profile 12. [A] Seismic section (amplitude). [B] Seismic section using the envelope seismic attribute. [C] Seismic interpretation of the main horizons. Most relevant horizons: top (TTTL) and base (BTTL) of the Thick Transparent Layers (Hieke, 2000). Base of the fossil sediment waves (BSW). Top of the Messinian (TM). See location of the profile in Figure VI.13.

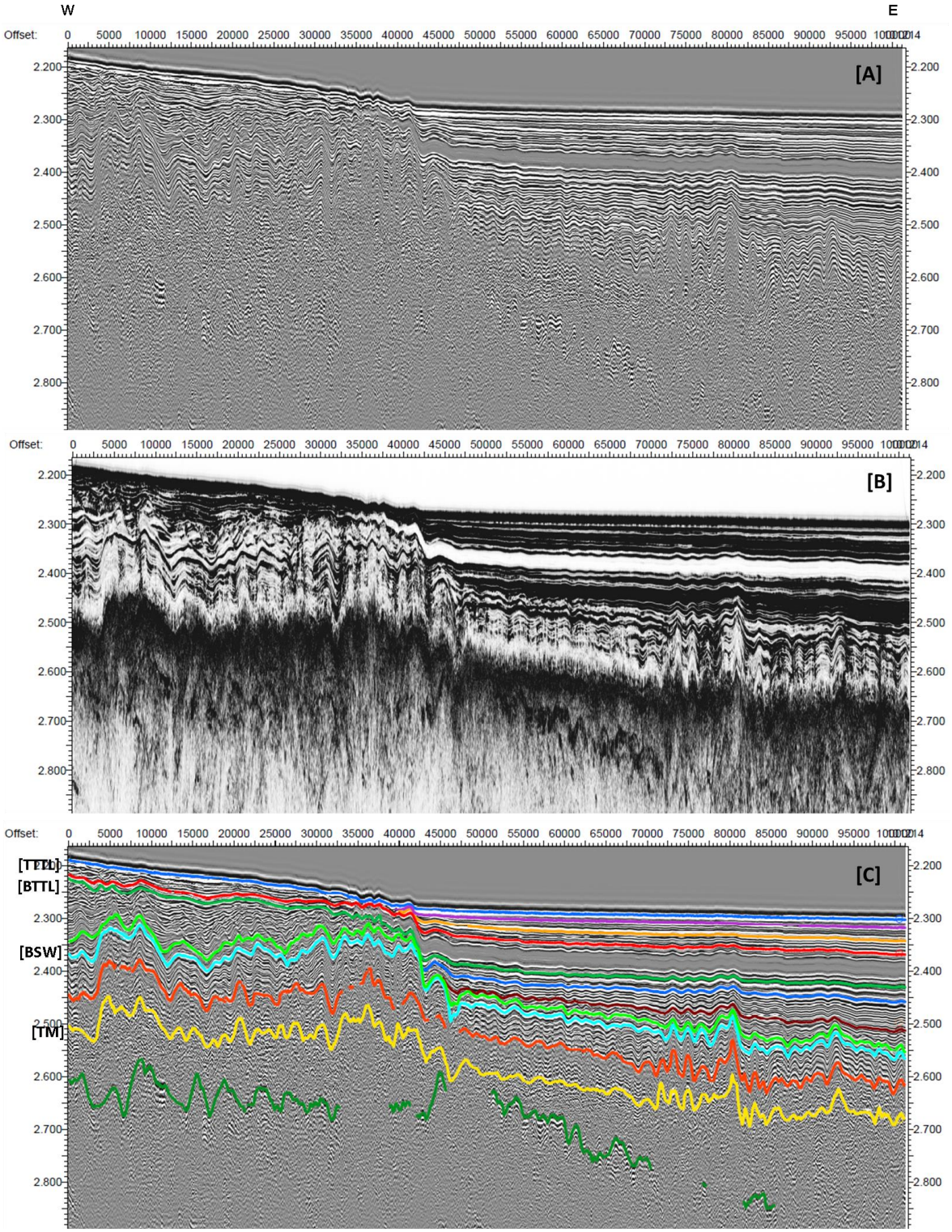

Figure VI.15 - Multichannel seismic profile 13. [A] Seismic section (amplitude). [B] Seismic section using the envelope seismic attribute. [C] Seismic interpretation of the main horizons. Most relevant horizons: top (TTTL) and base (BTTL) of the Thick Transparent Layers (Hieke, 2000). Base of the fossil sediment waves (BSW). Top of the Messinian (TM). See location of the profile in Figure VI.13.

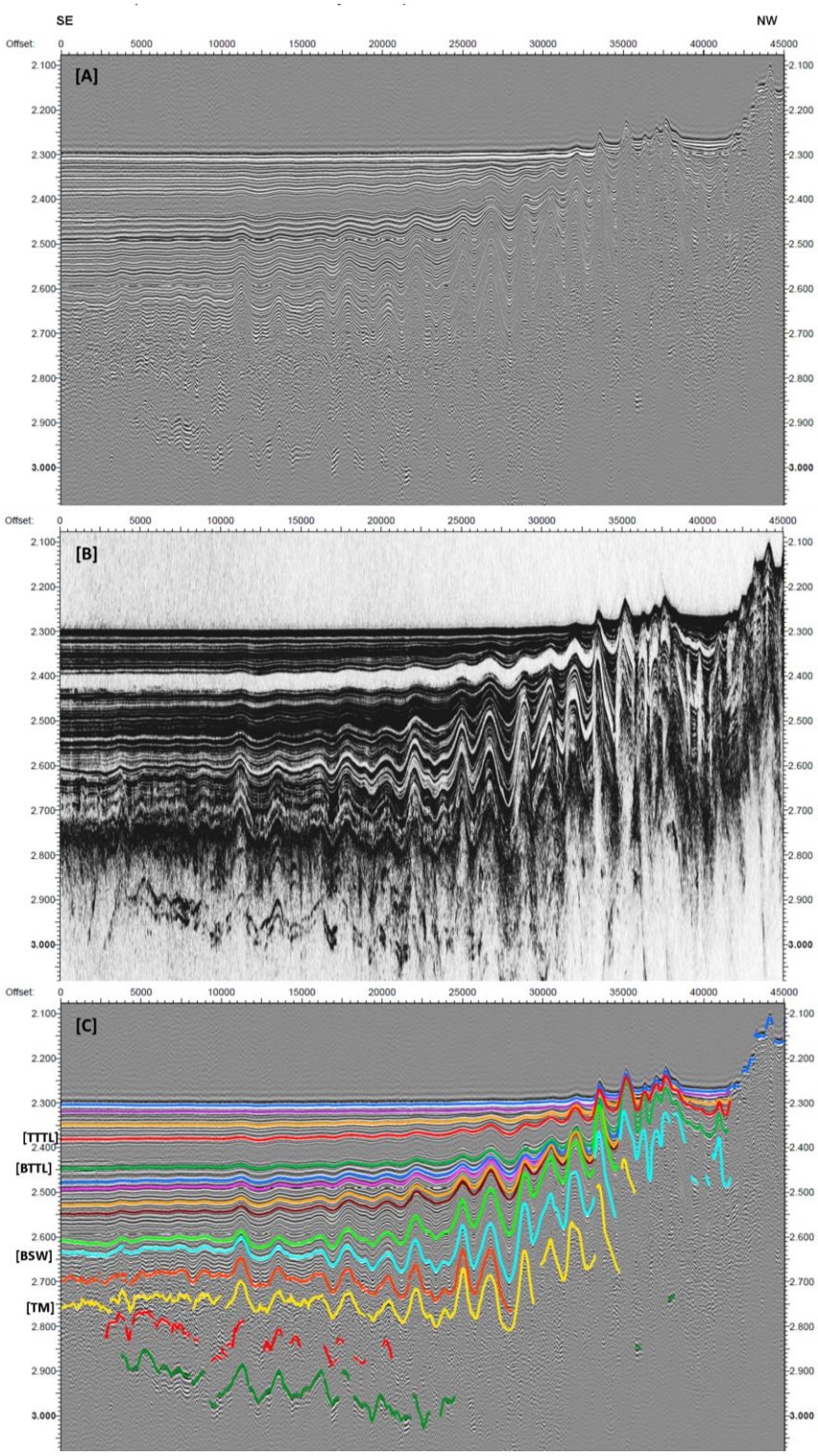

Figure VI.16 - Multichannel seismic profile 16. [A] Seismic section (amplitude). [B] Seismic section using the envelope seismic attribute. [C] Seismic interpretation of the main horizons. Most relevant horizons: top (TTTL) and base (BTTL) of the Thick Transparent Layers (Hieke, 2000). Base of the fossil sediment waves (BSW). Top of the Messinian (TM). See location of the profile in Figure VI.13.

The Thick Transparent Layer (TTL; Hieke, 2000) is well expressed in profiles 12, 13 and 16-1 (Figure VI.17). Assuming seismic velocities of 2500 m/s, the thickness of the TTL could reach up to 83 m Ionian Abyssal Plain (0.066s TWT; profile 16-01). This turbidity deposit is a good marker to delimit the top of fossil sediment waves observed in seismic profiles that cross fields A and B, allowing an age to be assigned to the time of abandonment of sediment wave formation in same areas.

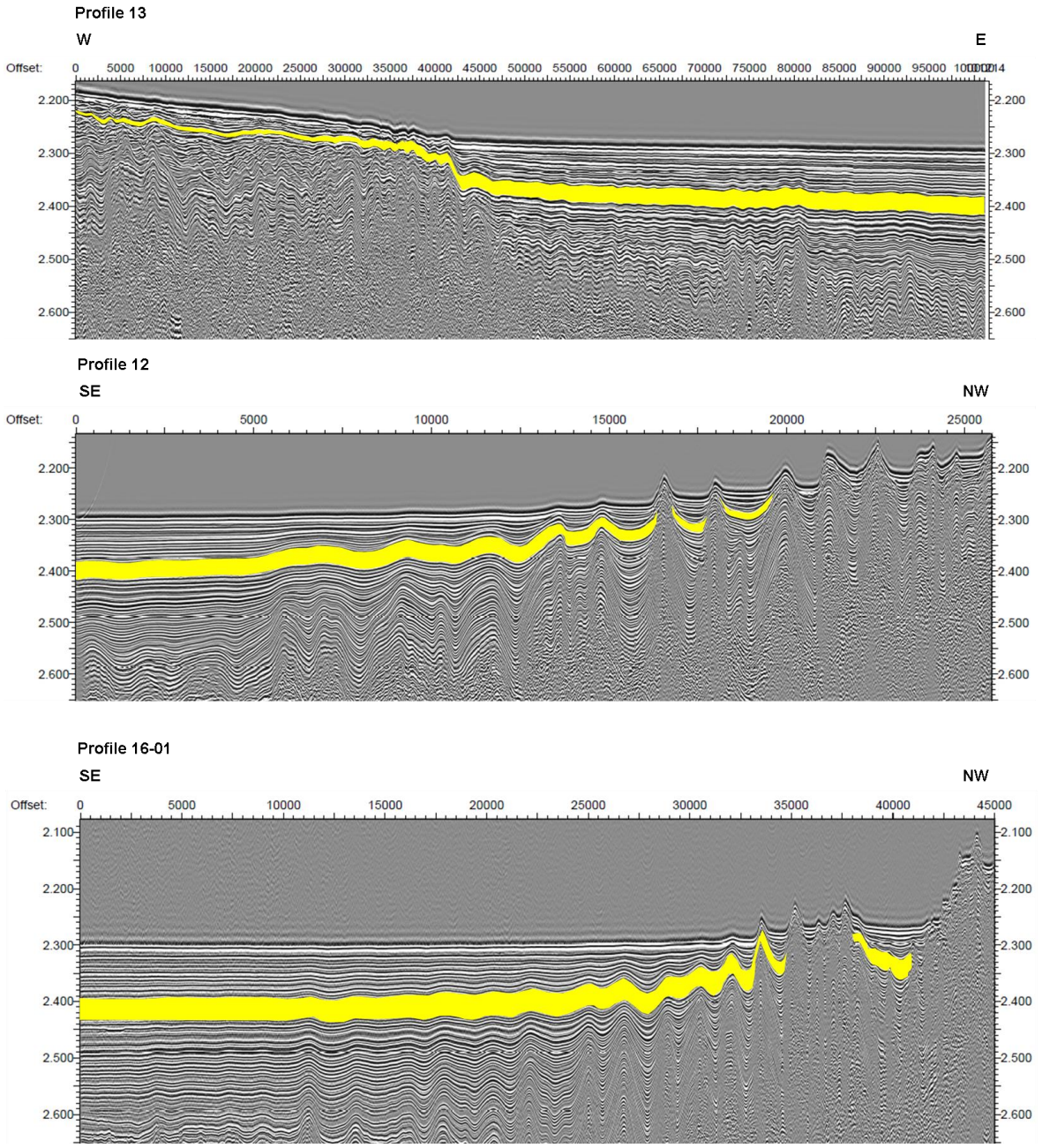

Figure VI.17 - Thick Transparent Layer (TTL; in yellow; Hieke, 2000) identified in CIRCEE-HR seismic profiles 12, 13 and 16-01. The location of the profiles can be seen in Figure VI.13.

In the absence of borehole constrained age interpretations of seismic profiles in the study area, and in order to assign tentative dates to the various episodes of sediment wave formation (Figure V.18), the top of the Messinian (5.3 Myr; International Chronostratigraphic Chart, v2016/12) was interpreted on the relevant seismic profiles. If a constant sedimentation rate is assumed until present (assuming an average seismic velocity about 2700 m/s), a value of ≈ 10cm/1000yr is obtained; this value is consistent with a value of 14cm/1000yr for the Pleistocene, and an average value of about 6cm/1000yr for the Pliocene, obtained at DSDP Site 374 in the Ionian Sea, close to the study area (Cita, Ryan and Kidd, 1978). An age of 2.58Myr was assumed for the Plio-Pleistocene boundary (International Chronostratigraphic Chart, v2016/12). A depth conversion based on the average sedimentation rates of Cita, Ryan and Kidd (1978) was used for the post-Messinian (Figure VI.18).

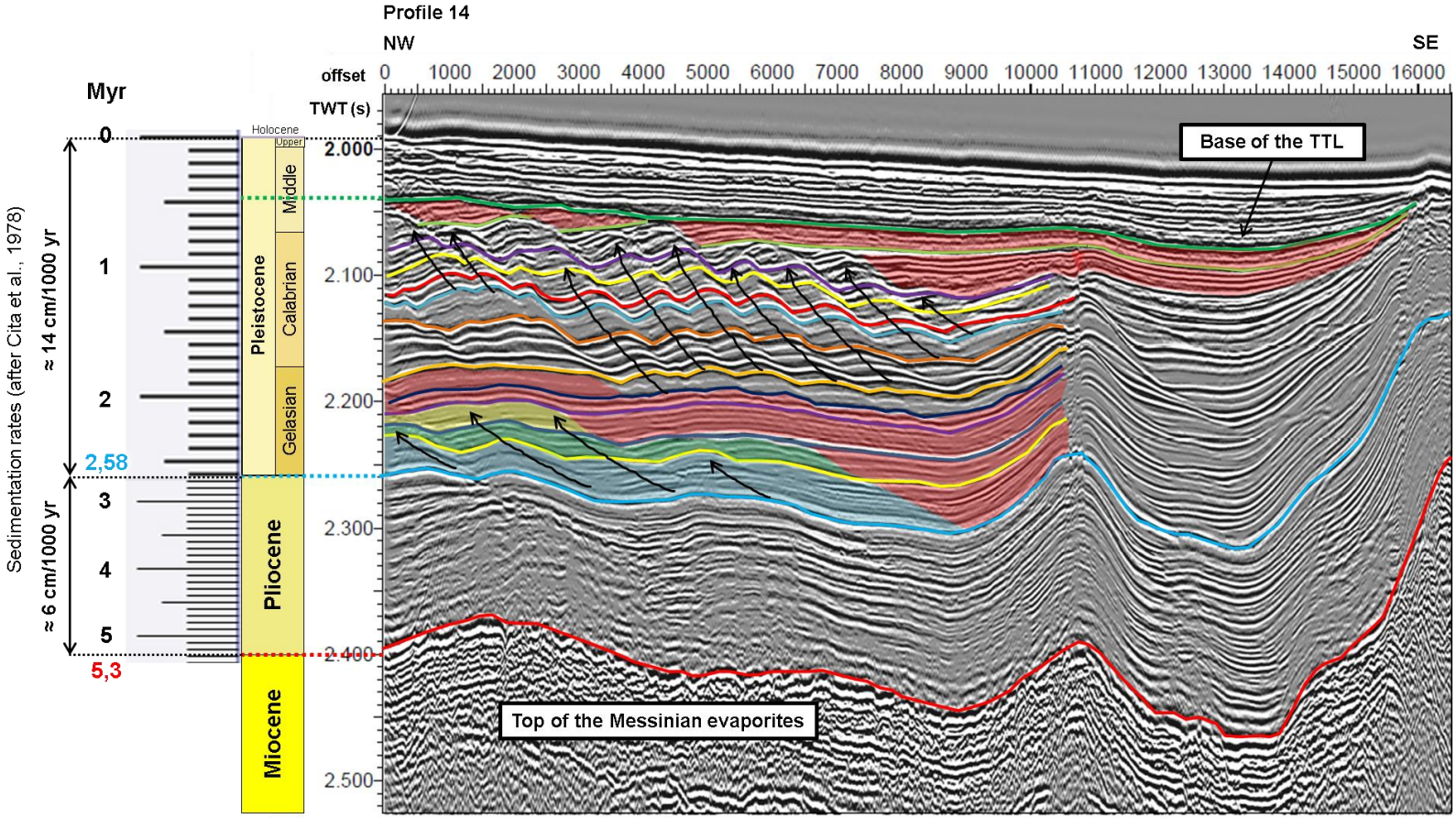

Figure VI.18 - Tentative of dating major seismic horizons in seismic profile 14 (fossil sediment waves from field B) based only on the age of Miocene/Pliocene boundary (5.3 Myr; International Chronostratigraphic Chart, v2016/12) assigned to the reflector that marks the top of Messinian, and sedimentation rates for the Pliocene and Pleistocene, obtained at DSDP Site 374 in the Ionian Sea (Cita, Ryan and Kidd, 1978). This allows to define the reflector that marks the Pliocene/Pleistocene boundary, at about 2.58 Myr (International Chronostratigraphic Chart, v2016/12). Major seismic horizons were identified: top of the Messinian (red); Pliocene/Pleistocene boundary and base of the fossil sediment wave field (blue); an evident change of the sediment wave pattern (dark blue at about 2.2s TWT); base of the TTL and top of the fossil sediment wave field (dark green). Other indicate horizons presented identify several sediment wave formation events. Light red areas mean a gap in the sediment wave formation. Black arrows show the migration direction of the sediment waves. See location of the seismic profile in Figure VI.3).

VI.3 Sediment wave evolution in Fields A, B and C

In this section we analyze the evolution of the sediment wave fields in the study area. It is important to note that wavelength and wave height values presented here are not real but apparent.

Sediment Wave Field A

In this area, the presently-active sediment wave crests seem to be perpendicular/oblique (Figure VI.19) to the present-day turbidity channel that surrounds the deformation front of the Calabrian accretionary wedge (see yellow line in Figure VI.1). Seismic profiles perpendicular to the deformation front show evidence of some upper-slope migration (Figure VI.20). Northward, fossil sediment waves are buried bellow the location of the present-day channel. The wavelength (≈762m) and wave height (≈50m) values of the fossil sediment waves (Profile 11-01; Figure VI.20), assuming v=2000m/s, are larger than the presently-active sediment waves values (≈455m and ≈30m, respectively), showing differences in the hydrodynamics or at the sediment grain size in the region.

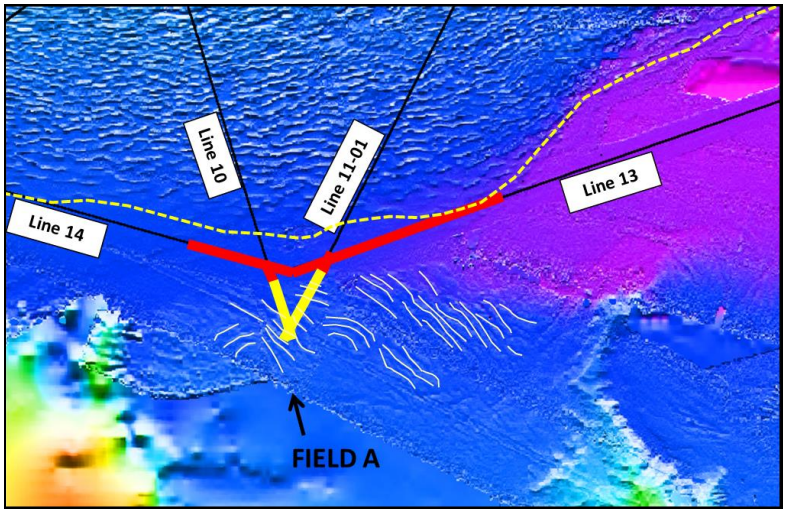

Figure VI.19 - Migrating sediment wave field A. The colored traces (yellow and red) indicate the segments of the seismic profiles where the sediment waves were observed (yellow lines: presently-active sediment waves; red lines: fossil sediment waves). Light yellow dashed line: deformation front of the Calabrian accretionary wedge. The high-resolution bathymetry map shows clearly a presently-active sediment field (courtesy from Marc-Andre Gutscher; MS in prep. Gutscher et al.). Light pink lines: main directions of the crests of presently-active sediment waves.

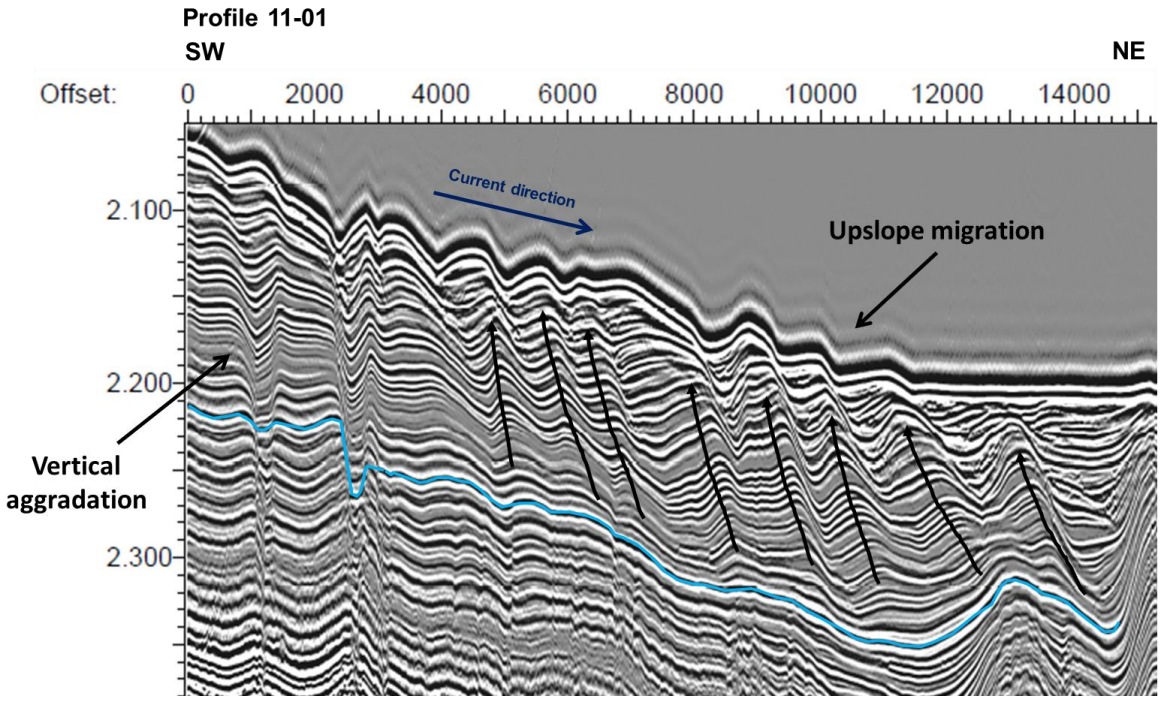

Figure VI.20 - Presently-active and fossil sediment waves in profile 11-01. See location of the profile in Figure VI.3. Blue line: Pliocene/Pleistocene boundary and base of the fossil sediment wave field. Black arrows show the migration direction of the sediment waves.

The asymmetry of the sediment waves allows defining an apparent current direction (Figure VI.20). The sediment waves in this section are essentially migrating in an apparent SW direction but change into essentially aggradational close to the Medina Seamounts.

Sediment Waves Field B

Profile 14 reveals the best image of fossil sediment waves of field B and will be used to explain the several formation episodes. Previously, in Figure VI.18, we propose tentative ages for the main reflectors based on available data. According to those ages, the first evidences of sediment wave formation were in the Early Pleistocene and their formation appears to have occurred approximately at the Pliocene/Pleistocene boundary, a time of major climatic and oceanographic changes in the Northern hemisphere (Head, Pillans and Farquhar, 2008). Between 2.58 and 2 Myr, part of the section shows the formation of longer wavelength (~1450m) upslope migrating sediment waves, essentially in the WNW portion of the line. There seems to be a progression of sediment wave formation to the

WNW during this period (compare blue, green and yellow shaded areas in Figure VI.18. At about 2.2 Myr almost no sediment waves were formed in this area (red shaded areas in Figure VI.18). At about 2.2 Myr major episodes of sediment wave formation episodes were triggered. These sediment waves have shorter wavelengths of ≈905m and larger wave heights of ≈22.5m (assuming v=2500 m/s) than the older ones (≈1450m and ≈12.5m, respectively). These more recent sediment waves clearly show migration upslope, except for the northerwest section where only aggradation occurs. Around 700kyr the formation of sediment waves began to cease in the eastern portion of the seismic section (Figure VI.18). The horizon that represents the base of TTL represents the end of the activity of this fossil sediment field, about 400kyr ago. Just to the E of the sediment wave field, a deep submarine turbidite(?) channel is observed which would lie north of the present turbidite channel axis interpreted by San Pedro et al., 2016; Figure VI.1). As will be discussed in Section VI.4, this points to a palaeochannel turbidite channel spillover as a possible formation mechanism.

Sediment Wave Field C

The sediment waves of field C present an asymmetric geometry, well-laminated and gently dipping internal reflectors and an up-slope migration pattern (Figure VI.21). The wavelengths are about 565 m and the wave heights vary between 21 and 28 m (assuming an average seismic velocities of 1500 and 2000 m/s for the superficial and fossil, respectively).

It was not possible in this work to variably correlate the seismic horizons to the northern profile in order to date the start of the fossil sediment wave formation in this area.

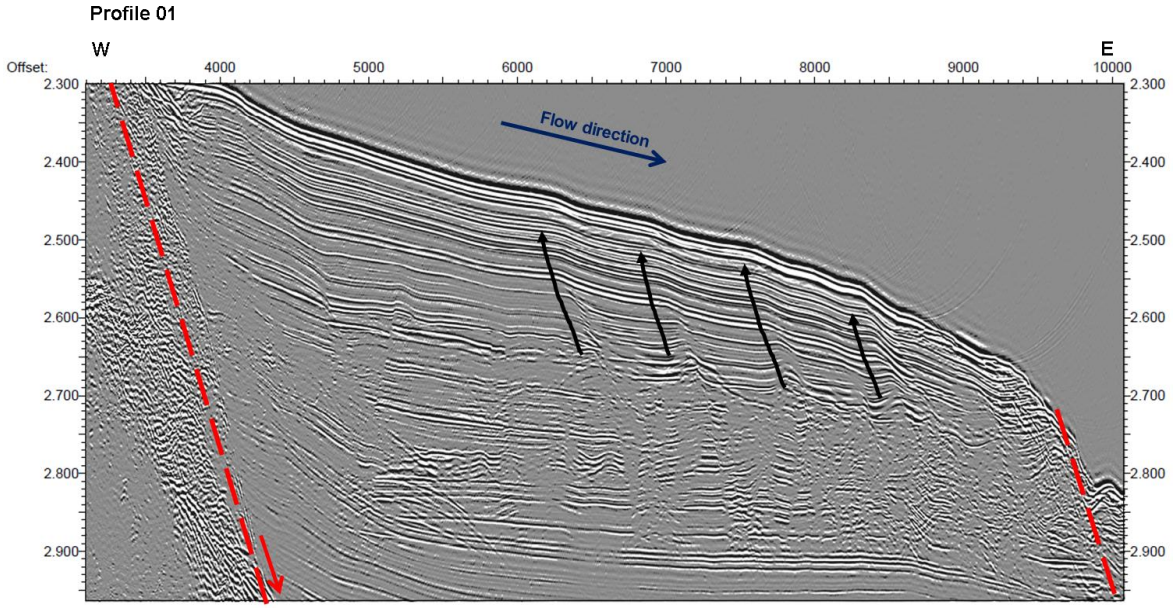

Figure VI.21 - Sediment waves from seismic profile 01. See line location in Figure VI.2. The direction of the current is down-slope (dark blue arrow). Black arrows show the migration direction of the sediment waves (up-slope). Red dashed lines are two major normal faults.

VI.4 Possible formation models

Sediment Wave Field C

As concerns the northern field (field C; profile 01; Figures VI.2 and VI.22A), the observed migrating sediment waves might be explained by gravity flows (turbidity currents), since its location is in the midslope Augusta, next to the Malta escarpment, where several canyons exist and where sediments flow down-slope to the channels in the base of the escarpment. Turbidite channel spillovers may explain their formation. However, internal solitary waves formed in the Messina Straight (Figure VI.22B), may provide an alternative formation mechanism in field C, as these can easily explain the observed patterns. Recently, Droghei *et al*. (2016) reported this formation mechanism to explain the formation of a migrating sediment wave field off Messina Strait (see Section V.1 and Figure V.11).

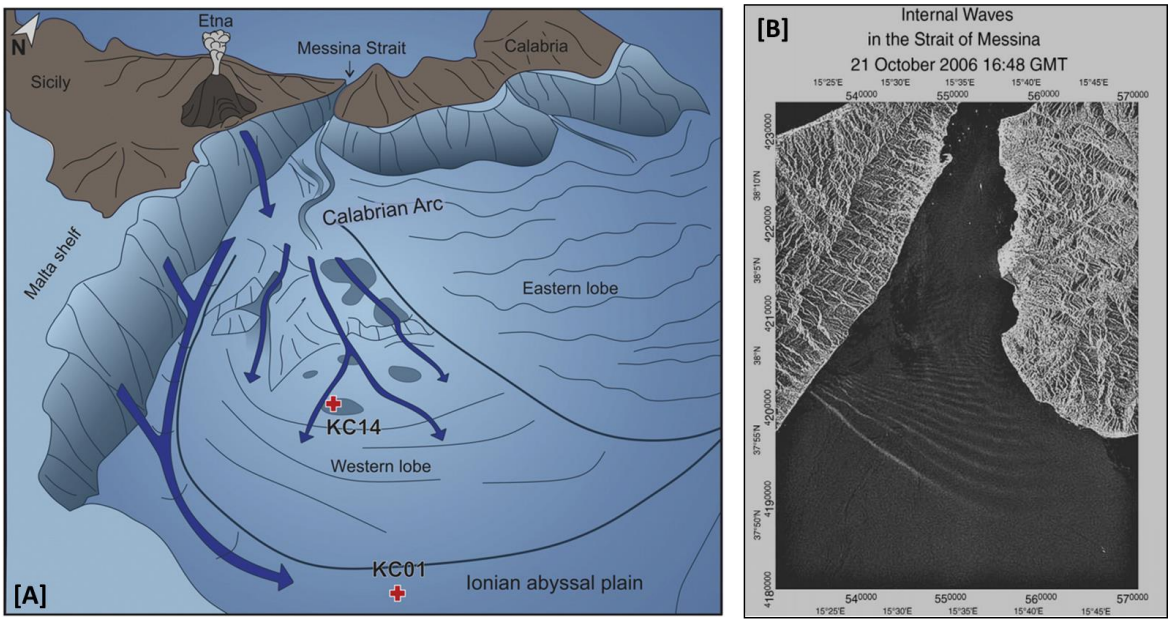

Figure VI.22 - Hypothesis of formation mechanisms of sediment waves. [A] Reconstruction of the main underwater flow on the Calabrian Arc (Köng et al., 2016). [B] SAR image shown a clear internal solitary waves train signature in the Messina Strait, propagating to southward (Casagrande et al., 2009).

Sediment Wave Fields A and B

As concerns the two southern fields, although we cannot rule out the possible role of internal waves, there are no reported observations of their presence in this area. Also in field B, the formation of sediment waves appears to have stopped sometime between 700kyr and 400kyr. For this area, we propose that the fossil sediment waves (Line 14; Figure VI.18) have been formed by turbidite channel spillover (see in particular Figure VI.19), producing sediment waves approximately perpendicular to the main turbidite channel (Figure VI.3); we cannot, nevertheless rule out the possibility of interaction of the main turbidite channel, that approximately follows the deformation front, with bottom currents, but we could not also find any report of their existence in this area.

Chapter VII. Conclusions and Future Work

Main conclusions

In general, the main objectives of this thesis were essentially achieved. The CIRCEE-HR high resolution multichannel seismic lines were reprocessed and a slight improvement of the imaging of the deeper part of the seismic sections was obtained. The lack of a very significant improvement is due to the short streamer length that did not allow a reliable velocity model to be obtained. This is also why we could not get any better results with pre-stack time migration.

3 main fields of sediment waves, both fossil and active were identified on the set of high resolution multichannel seismic reflection profiles available for this study. These were investigated and several generations of sediment waves with different wavelengths and amplitudes were identified.

In the absence of borehole constrained age interpretations of seismic profiles in the study area, and in order to assign tentative dates to the various episodes of sediment wave formation, an overall interpretation of the main seismic reflectors was carried out and correlated between the various seismic profiles. In particular, top of the Messinian was interpreted on the relevant seismic profiles. Using average sedimentation rate values of 14cm/1000yr for the Pleistocene, and of about 6cm/1000yr for the Pliocene, based on DSDP Site 374 data, it was possible to tentatively date the main reflectors and episodes of sediment wave generation.

Two main models of formation were proposed. For the northernmost Sediment Wave Field C, although a possible origin related to turbidite channel spillover cannot be ruled out, it appears that solitary internal waves generated at the Messina Strait may be the more likely responsible mechanism. This is supported by recent studies and by SAR images. As concerns the two southern fields, however, although the possible role of internal waves or the interaction of turbidite channels with bottom currents cannot be ruled out, there are no reported

observations of their presence of neither of them in this area. Therefore, we propose that the fossil sediment waves have been formed by turbidite channel spillover, producing sediment waves approximately perpendicular or oblique to the main turbidite channel. The turbidite channel that now approximately follows the deformation front appears to have been before located further north, this may be an indication that the migration to the south of the accretionary wedge associated with the subduction rollback has stopped the formation of the sediment waves, which are at present formed much further south. If this is correct, a detailed interpretation, constrained by reliable ages, of the various generations of sediment waves in this area may help to constrain the dynamics of the accretionary wedge migration episodes. In field B, the formation of the sediment waves appears to have completely stopped sometime at about 400kyr, although this process started locally at about 700mMyr. We interpret this as linked to the migration to the south of the turbidite channel that approximately follows the edge of the deformation front, caused by the subduction rollback.

Future Work

The main conclusions of this thesis are naturally limited by the time available and a more detailed study of the various sediment wave episodes revealed on these seismic lines, now that a time framework has been obtained for this purpose, may still allow a more refined model that may help to better understand of the interaction between tectonics, associated with the subduction rollback and the migration to the south of the accretionary wedge and deformation front, turbidite episodes and sedimentation, and bottom currents and internal solitary waves. As such, for future work, we suggest to:

1. Refine the age model obtained for the main seismic reflectors based on other well data, if available;

2. Map in detail the presently active sediment wave fields, using for that purpose the new multibeam data recently acquired in this region;

3. Compile any other seismic lines that may exist in this area, reprocess them if necessary and use them to constrain the 3D geometry of the fossil sediment wave fields;

4. Acquire a new 2D high resolution seismic dataset, with a similar source to the one used in CIRCEE-HR to get a good penetration, along detailed grids over the fossil sediment wave fields and with exploratory lines to define the total extension of the sediment wave fields;

5. Compile all the available information on deep contour currents and on internal waves and solitons that may exist in this area, by contacting naval hydrographic offices and by analyzing SAR images in the vicinity of the presently active sediment wave fields;

6. Perform numerical and analog models in cooperation with physical oceanographers to test and better understand the various possible formation models for sediment wave migration.

Bibliography

Cartigny, M., Postma, G., Berg, J., & Mastbergen, D. (2011). A comparative study od sediment waves and cyclic steps based on geometries, internal structures and numerical modeling. *Marine Geology, 280*, 40-56.

Casagrande, G., Varnas, A., Stéphan, Y., & Folégot, T. (2009). Genesis of the coupling of internal wave modes in the Strait of Messina. *Journal of Marine Systems, 78*, S191-S204.

Cita, M., Ryan, W., & Kidd, R. (1978). Sedimentation rates in Neogene deep-sea sediments from the Mediterranean and geodynamic implications of their changes. Em K. Hsü, & L. Montadert, *Init. Rep. DSDP, XCLL* (Vol. part 1, pp. 991-1002).

Cohen, K., Finney, S., Gibbard, P., & Fan, K.-X. (2013; updated). The ICS International Chronostratigraphic Chart. (Episodes 36: 199-204).

Damuth, J. (1979). Migrating sediment waves created by turbidity currents in the northern South China Basin. *Geology, 7*, 520-523.

Dobrin, M., & Savit, C. (1988). *Introduction to Geophysical Prospecting* (4 ed.). McGraw-Hill.

Droghei, R., Falcini, F., Casalbore, D., Martorelli, E., Mosetti, R., Sannino, G., . . . Chiocci, F. (2016). The role of Internal Solitary Waves on deep-water sedimentary processes: the case of up-slope migrating sediment waves off the Messina Strait. *Scientifc Reports, 6*, 36376. doi:10.1038/srep36376

Ercilla, G., Alonso, B., Wynn, R., & Baraza, J. (2002). Turbidity current sediment waves on irregular slopes: observations from the Orinoco sediment-wave field. *Marine Geology, 1-3*, 171-187.

Faccenna, C., Becker, T. W., Lucente, F. P., Jolivet, L., & Rossetti, F. (2001). History of subduction and back-arc extension in the Central Mediterranean. *Geophys. J. Int., 145*, pp. 809-820.

Flood, R. (1988). A lee wave model for deep-sea mudwave activity. *Deep-Sea Research, 35*(6), 973-983.

Flood, R., & Giosan, L. (2002). Migration history of a fine-grained abyssal sediment wave on the Bahama Outer Ridge. *Marine Geology, 192*, 259-273.

Gallais, F., Gutscher, M.-A., Klaeschen, D., & Graindorge, D. (2012). Two-stage growth of the Calabrian accretionary wedge in the Ionian Sea (Central Mediterranean): Constraints from depth-migrated multichannel seismic data. *Marine Geology, 326-328*, pp. 28-45.

Gong, C., Wang, Y., Peng, X., Li, W., Qiu, Y., & Xu, S. (2012). Sediment waves on the South China Sea Slope off southwestern Taiwan: Implications for the intrusion of the Northern Pacific Deep Water into the South China Sea. *Marine and Petroleum Geology, 32*, 95-109.

Gutscher, M.-A. (2013). *CIRCEE-HR mission report.*

Gutscher, M.-A., Dominguez, S., Lepinay, B., Pinheiro, L., Gallais, F., Babonneau, N., . . . Rovere, M. (2015). Tectonic expression of an active slab tear from high-resolution seismic and bathymetric data offshore Sicily (Ionian Sea). *Tectonics, 34*. doi:10.1002/2015TC003898

Hatton, L., Worthington, M. H., & Makin, J. (1986). *Seismic Data Processing: Theory and Practice.* Blackwell Scientific Publications.

Head, M., Pillans, B., & Farquhar, S. (2008). The Early–Middle Pleistocene Transition: characterization and proposed guide for the defining boundary. *Episodes, 31, no.2*, 255-259.

Hieke, W. (2000). Transparent layers in seismic reflection records from the central Ionian Sea (Mediterranean) — evidence for repeated catastrophic turbidite sedimentation during the Quaternary. *Sedimentary Geology, 135*, 89-98.

Hieke, W., & Werner, F. (2000). The Augias megaturbidite in the central Ionian Sea (central Mediterranean) and its relation to the Holocene Santorini event. *Sediment. Geol., 135*, 205-218.

Hieke, W., Melguen, M., & Fabricius, F. (1975). Migration of tectonics from the Mediterranean Ridge into the Messina Abyssal Plain (Ionian Sea). *Rapp. Comm. Int. Mer Mèdit 23, 4a*, 89.

Karl, H., Cacchione, D., & Carlson, P. (1986). Internal-wave currents as a mechanism to account for large sand waves in Navarinsky Canyon Head, Bering Sea. *Sedimentary Petrology, 56*, 706-714.

Kearey, P., & Brooks, M. (1991). *An Introduction to Geophysical Exploration* (2 ed.). Blackwell Science.

Köng, E., Zaragosi, S., Schneider, J.-L., Garlan, T., Bachèlery, P., San Pedro, L., . . . Racine, C. (2016). Untangling the complex origin of turbidite activity on the Calabrian Arc (Ionian Sea) over the last 60 ka. *Marine Geology, 373*, 11-25.

Larner, K., Chambers, R., Yang, M., Lynn, W., & Wai, W. (1983). Coherent noise in marine seismic data. *Geophysics, 48*, 854-886.

McQuillin, R., Bacon, M., & Barclay, W. (1984). *An Introduction to Seismic Interpretation* (2 ed.). Graham & Trotman.

Migeon, S., Savoye, B., & Faugeres, J.-C. (2000). Quaternary development of migrating sediment waves in the Var deep-sea fan: distribution, growth pattern, and implication for levee evolution. *Sedimentary Geology, 133*, 265-293.

Minelli, L., & Faccenna, C. (2010). Evolution of the Calabrian accretionary wedge (central Mediterranean). *Tectonics, 29*. doi:10.1029/2009TC002562

Polonia, A., Bonatti, E., Camerlenghi, A., Lucchi, R., Panieri, G., & Gasperini, L. (2013). Mediterranean megaturbidite triggered by the AD 365 Crete earthquake and tsunami. *Scientific Reports, 3*, 1285. doi:10.1038/srep01285

Polonia, A., Torelli, L., Mussoni, P., Gasperini, L., Artoni, A., & Klaeschen, D. (2011). The Calabrian Arc subduction complex in the Ionian Sea: Regional architecture, active deformation, and seismic hazard. *Tectonics, 30*. doi:10.1029/2010TC002821

Reeder, D., Ma, B., & Yang, Y. (2011). Very large subaqueous sand dunes on the upper continental slope in the South China Sea generated by episodic , shoaling deep-water internal solitary waves. *Marine Geology, 279*, 12-18.

Rosenbaum, G., Lister, G. S., & Duboz, C. (2002). Reconstruction of the tectonic evolution of the western Mediterranean since the Oligocene. *Journal of the Virtual Explorer, 8*, pp. 107-130.

Seismic characteristics and processes of the Plio-Quaternary unidirectionally migrating channels and contourites in the northernslope of the South China Sea. (2013). *Marine and Petroleum Geology, 43*, 370-380.

Sheriff, R. (1991). *Encyclopedic Dictionary of Exploration Geophysics* (3 ed.). Geophysical References Series.

Sheriff, R. (1996). *Understanding the Fresnel Zone.*

Sheriff, R., & Geldart, L. (1995). Exploration Seismology. *Cambridge University Press*, 592.

Telford, W., Geldart, L., & Sheriff, R. (s.d.). *Applied Geophysicis* (2 ed.). Cambridge University Press.

Tontini, F. C., Graziano, F., Cocchi, L., Carmisciano, C., & Stefanelli, P. (2007). Determining the optimal Bouguer density for a gravity data set: implications for the isostatic setting of the Mediterranean Sea. *Geophys. J. Int., 169*, 380-388.

Wynn, R. B., & Stow, D. A. (2002). Classification and characterisation of deep-water sediment waves. *Marine Geology, 192*, 7-22.

Wynn, R., & Stow, D. (2002). Classification and characterisation of deep-water sediment waves. *Marine Geology, 192*, 7-22.

Wynn, R., Weaver, P., Ercilla, G., Stow, D., & Masson, D. (2000). Sedimentary processes in the Selvage sediment-wave field,NE Atlantic: new insights into the formation of sedimentwaves by turbidity currents. *Sedimentology, 47*, 1181-1197.

Wynn, R., Weaver, P., Ercilla, G., Stow, D., & Masson, D. (2000c). Sedimentary processes in the Selvage sediment-wave field, NE Atlantic: new insights into the formation of sediment waves by turbidity currents. *Sedimentology, 47*, 1181-1197.

Xu, J., Wong, F., Kvitek, R., Smith, D., & Paull, C. (2008). Sandwave migration in Monterey Submarine Canyon, Central California. *Marine Geology, 248*, 193-212.

Yilmaz, O. (1987). *Seismic Data Processing.* Society of Exploration Geophysicists, Tulsa.

Yilmaz, O. (2001a). *Seismic Data Analysis: Processing, Inversion, and Interpretation of Seismic Data* (Vol. 1). Society of Exploration Geophysicists.